Creating Structural Material From Martian Regolith Using Spark Plasma Sintering

Understanding the effect of additives and the possibility to lower the energy requirement

G.W.H. Hoekman

Delft University of Technology

TU Delft

This page is intentionally left blank.

Cover image from *Foster + Partners*, retrieved from businessinsider.com. Last accessed: 20-04-2022

Creating Structural Material From Martian Regolith Using Spark Plasma Sintering

Understanding the effect of additives and the possibility to lower the energy requirement

by

G.W.H. Hoekman

to obtain the degree of Master of Science
at the Delft University of Technology,
to be defended publicly on Tuesday May 10, 2022 at 15:30 hour.

Student number:	4355725	
Project duration:	April 19, 2021 – May 10, 2022	
Thesis supervisors:	Prof. dr. ir. S. van der Zwaag,	TU Delft, supervisor
	Dr. Y. Tang,	TU Delft, supervisor
Thesis committee:	Prof. dr. ir. S. van der Zwaag,	TU Delft, supervisor
	Ir. J. Sinke,	TU Delft
	Dr. V. A. Popovich,	TU Delft

TU Delft

Abstract

In order to establish a sustained extra-terrestrial presence, habitats need to be built on the Moon and Mars using novel materials made from local resources. Several material processing methods can be applied to transform the locally abundant regolith into materials suitable for structural purposes. One promising method is sintering. This process can be used to create strong material using little to no Earth-imported additives. However, sintering still requires a large amount of energy to heat the material. A possible method to lower the energy requirement is by introducing small amounts of sintering aids. However, little is known about the effect of aids on the properties of sintered regolith. This research aims to investigate the effect of sintering aids on the densification and mechanical properties of sintered Martian regolith simulant.

In this study, the chosen Martian regolith simulant, Martian Global Simulant - 1 (MGS-1), was first investigated using a variety of powder characterisation techniques to assess the similarity with actual Martian material. Using the Spark Plasma Sintering (SPS) technique, disk shaped samples were sintered at temperatures between 700 °C and 1060 °C and pressures of 30 MPa to 50 MPa. Several powder mixtures were used. Two different additives, aluminium and bismuth oxide, were used in two weight percentages, 2.5wt% and 5wt%, and mixed with baseline material. Samples sintered from this enriched material were compared to those made using baseline MGS-1 material. In order to assess the mechanical properties, the Ball-on-Ring (BoR) compression test was used to determine the biaxial flexure strength of the samples. Since the BoR compression test is a semi-standardised method, an effort was made to validate the testing procedure and obtained results using soda-lime glass samples. Additionally, mortar disks were created and tested to provide a reference for terrestrial material properties. After compression testing, some samples were ground back into a powder and examined using X-ray Diffraction (XRD) to assess any bulk composition changes induced by the additive and/or sintering process.

The results from the powder characterisation techniques show that the chemical composition of MGS-1 is close to that of actual Martian material. In order to achieve strengths comparable to terrestrial mortar, a relative density of at least 70 % needs to be achieved. For the baseline material, the sintering temperature needs to exceed 1000 °C in order to obtain these results. This value is 950 °C for 2.5wt% aluminium additive material, and 900 °C for 5wt% aluminium, 2.5wt% and 5wt% bismuth oxide additive material. For equal sintering temperatures, the biaxial strength of enriched powders exceeds that of baseline material. Hence, the sintering temperature can be lowered for enriched materials to achieve similar strengths. Samples made from bismuth oxide enriched material exhibited superior properties compared to aluminium enriched material. For aluminium enriched material, no clear increase in properties is observed with increasing additive fraction. For bismuth oxide enriched material, there appears to be an increase in properties with increasing additive fraction. A material behaviour transition from brittle to tough appears to be linked to biaxial strengths exceeding 12 MPa. Compared to literature on Martian regolith-based materials, the results for sintered enriched MGS-1 perform well in terms of required additive fraction and mechanical properties. Using additives could potentially be a way to lower the energy requirement for regolith sintering on Mars. This work opens up areas of further research into the optimal additive, additive amount and sintering parameters for on-site application.

Acknowledgements

The completion of this thesis marks the end of my long journey as a student. I have learned a lot through the years I have had the pleasure of walking the halls of the faculty of Aerospace Engineering. Not only due to the many lectures, but also in large part to my extra-curricular activities and the amazing people I have met in the various committees, teaching assistant jobs, my time in the faculty student council and the part-time board of the Enlightness student association.

As a student I have completed many projects, some more challenging than others. The master thesis was arguably my greatest challenge yet. I could not have completed it without my supervisors guiding me along the way. Therefore, first of all, thank you Dr. Yinglu Tang and Prof. dr. ir. Sybrand van der Zwaag for all the support during my thesis. Yinglu, I was one of your first graduate students and you were the one who introduced me into the wonderful world of space materials. Thank you for all the enthusiastic meetings we had, they have always been a great motivator for me. Also thank you for the valuable insight you gave regarding the project and the unwavering willingness to make time for me. Sybrand, your professional knowledge is second to none, which was invaluable to my project. Thank you for supervising me and meeting with me even though by the end of my thesis you were technically retired. Thank you for the amazing critical eye you gave towards my project and the valuable insights. I am sure your advice has made me a better researcher, although there is still more work in that area. Thank you, Ir. Jos Sinke (who was there when I got my bachelor diploma) and Dr. Vera Popovich for taking part in my graduation committee.

A lot of my thesis was experimental work, which I could not have done without the support of some amazing people. First, I would like to thank Hans Brouwer. Hans, thank you for your enthusiasm about my project and teaching me (among much else) the ins and outs of SPS, although much still remains a mystery. Next, I would like to thank all the lab technicians and support staff who helped me perform my experiments. Durga, Marlies and Dave (and the rest of the DASML technicians), your help was immeasurable in obtaining the results used throughout this thesis. Thank you, Shanta, who made sure all was in place for me to graduate, and thank you to all the NovAM PhD students who always gave valuable advice and were always open for a chat or drink in 'de Atmosfeer'.

Working on a master thesis is not something you do alone. The support from peers is one of the most valuable contributions one can wish for during that time. Hence, I cannot thank my fellow NovAM master students enough who helped me along the way. Thank you Sèra, who was my constant office mate throughout my thesis (until she graduated), for all the advice, nice walks and excessive amounts of DE coffee. Thanks to Mark, Nikhil, Casper, Krishna and all the other NovAM students that enriched my time in the department.

Finally, I would like to thank the people closest to me. Starting with my family, and in particular my parents, who have always been there for me throughout my years in Delft. Thank you for the continuous support and the space to let me explore my own path. After all those years I've listened and spent my time finalising my education, instead of yet another side-track (although the OLT might have been my biggest yet). Thanks to all my friends from Groepje 32, the VSV and all the others I have made along the way for making my student time unforgettable. And last but certainly not least, Laura, without whom this thesis never would have been finalised. Thank you for giving the love and support I needed to finish this journey. Also, thank you for listening to my many troubles, giving more valuable advice than you are aware of and being the best proof-reader in the world.

G.W.H. Hoekman
Delft, April 2022

Contents

Abstract iii

Acknowledgements v

List of Tables ix

List of Figures xi

List of Symbols xiii

List of Abbreviations xv

1 Introduction 1
- 1.1 The Need for Extra-Terrestrial Construction . . . 1
- 1.2 The Importance of Using Local Resources . . . 1
- 1.3 Manufacturing Methods Using Regolith (simulant) . . . 2
- 1.4 Research Questions . . . 2
- 1.5 Thesis Structure . . . 2

2 Background and Literature 3
- 2.1 In-situ Resource Utilisation (ISRU) . . . 3
  - 2.1.1 Space Resource Utilisation (SRU) Universal Flowsheet . . . 3
  - 2.1.2 ISRU and Structural Materials . . . 3
  - 2.1.3 Important Aspects for ISRU . . . 4
  - 2.1.4 Design Constrains from ISRU . . . 4
- 2.2 Martian Regolith . . . 5
  - 2.2.1 Martian Regolith Description . . . 5
  - 2.2.2 Properties of Martian Regolith . . . 5
  - 2.2.3 Martian Regolith Simulant . . . 7
  - 2.2.4 Structural Material Made From Regolith . . . 8
- 2.3 The Sintering Process . . . 9
  - 2.3.1 Introduction to Sintering . . . 9
  - 2.3.2 Pressure-less vs Pressure-assisted Sintering . . . 10
  - 2.3.3 Liquid Phase Sintering . . . 11
  - 2.3.4 Sintering Aids . . . 11
  - 2.3.5 Spark Plasma Sintering (SPS) . . . 11
- 2.4 Mechanical Testing From disk-shaped Specimen . . . 13
  - 2.4.1 Uniaxial Compression Tests . . . 13
  - 2.4.2 Bending (Flexure) Tests . . . 13
  - 2.4.3 Multi-axial Flexure Tests . . . 13

3 Materials and Methods 15
- 3.1 MGS-1 Martian Regolith Simulant . . . 15
- 3.2 Additive Materials . . . 16
- 3.3 Material Preparation . . . 16
  - 3.3.1 Sieving . . . 16
  - 3.3.2 Mixing . . . 17
- 3.4 Characterisation Techniques . . . 17
  - 3.4.1 Scanning Electron Microscopy . . . 17
  - 3.4.2 Energy Dispersive X-ray Spectroscopy . . . 17
  - 3.4.3 Particle Shape Analysis . . . 18
  - 3.4.4 Particle Size Distribution Measurements . . . 19
  - 3.4.5 Thermogravimetric Dynamic Mechanical Analysis . . . 19
  - 3.4.6 Specific heat capacity determination . . . 20
  - 3.4.7 X-ray Powder Diffraction . . . 20

3.5 SPS Sintering Methodology . . . 20
3.6 Post Sintering Steps . . . 24
3.7 Mechanical Testing: Ball-on-ring Method . . . 24
3.7.1 Introduction, Theory and Governing Equations . . . 24
3.7.2 Compression Test Set-up . . . 26
3.7.3 Results Processing . . . 27
3.8 Mechanical Behaviour Determination . . . 28

4 Powder Characterisation 29
4.1 Bulk Chemistry of As-received MGS-1 . . . 29
4.2 Particle Size, Shape and Distributions . . . 30
4.3 MGS-1 Thermal Behaviour . . . 34
4.4 MGS-1 XRD Analysis . . . 36

5 The Effect of Sintering Parameters and Material on Sintered Sample Properties 39
5.1 The Effect of Temperature and Pressure . . . 39
5.2 The Effect of Particle Size . . . 41
5.3 The Effect of Dwell Cycle . . . 42

6 The Effect of Additives on Sintered Sample Properties 47
6.1 Introduction to the Effects of Additive Results . . . 47
6.2 Effect of Aluminium Additive . . . 47
6.3 Effect of Bismuth Oxide Additive . . . 49
6.4 Effect of Different Additive Weight Fractions . . . 51
6.4.1 Effect Additive Amount on Densification . . . 51
6.4.2 Effect of Additive Amount on Mechanical Properties . . . 52
6.4.3 Effect of Additive Material and Amount on Material Behaviour . . . 53

7 Discussion 55
7.1 Fitness of MGS-1 compared to actual Martian regolith . . . 55
7.2 Validity of Obtained Results . . . 55
7.3 Effect of SPS Settings and Particle Size on Sample Properties . . . 56
7.4 Effect of Additive Material and Amount on Properties . . . 56
7.5 Performance Compared to Literature . . . 58
7.6 Link of Obtained Results to Martian Application . . . 59

8 Conclusion 61

9 Recommendations 63

Bibliography 64

Appendices 70

A Sintered and Reference Sample Data 71
A.1 Sintering Sample Data . . . 71
A.2 Reference Sample Data . . . 74
A.2.1 Zirconia Reference Data . . . 74
A.2.2 Mortar Reference Data . . . 74
A.2.3 Soda-lime Glass Reference Data . . . 76

B Supplementary Information for the Compression Testing Method 77
B.1 Bench Compliance and Data Processing Information . . . 77
B.2 Validation Experiments . . . 77
B.2.1 Zirconia Disk Compression Results . . . 78
B.2.2 Mortar Disk Compression Results . . . 79
B.2.3 Soda-lime Glass Compression Results . . . 79
B.3 Effect of the Stress Range Correction . . . 81
B.4 Sensitivity Analysis . . . 81

List of Tables

2.1 Average bulk composition of basaltic soils in the Gale Crater, Meridiani Planum and Gusev Crater. Adapted from [18], using original data from [16, 17] 6
2.2 Chemical composition of several Martian regolith simulants 7

3.1 MGS-1 powder physical characteristics 15
3.2 MGS-1 mineralogy (as mixed) [62] 15
3.3 MGS-1 bulk chemistry as measured by XRF [62] 15
3.4 Density and melting temperature of additive materials 16
3.5 Constant SPS machine settings used during sintering 22
3.6 Overview of variable SPS sintering settings 23
3.7 Indenter ball properties used in strength calculations 27

4.1 Bulk chemistry of MGS-1 as reported by Exolith Lab compared to Martian compositions of different locations 29
4.2 Elemental composition of baseline MGS-1 calculated from EDS compared to calculated values from Exolith Lab and Gale Crater data 30
4.3 Weight and percentage of sieving fraction 30
4.4 Summarised results of particle shape descriptors 32
4.5 AMU fluctuations during mass spectrometry 35

A.1 Sintering parameters for all sintered samples 71
A.2 Physical properties for all sintered samples 72
A.3 Mechanical properties for all sintered samples 73
A.4 Physical properties for soda-lime glass reference samples 74
A.5 Mechanical properties for soda-lime reference samples 74
A.6 Physical properties for mortar reference samples 74
A.7 Mechanical properties for mortar reference samples 75
A.8 Physical properties for soda-lime glass reference samples 76
A.9 Mechanical properties for soda-lime glass reference samples 76

B.1 Data for the bench compliance tests used in data processing 77

List of Figures

2.1 Universal flowsheet for SRU processes, adapted from [9]. . . . 3
2.2 Additional binder upmass per shield volume increase, using wt% values commonly found across literature, including lines indicating current launcher limitations. Adapted from [10], launcher data from [11–14] . . . 5
2.3 Martian soil as photographed by the Curiosity rover. a) photograph of the Rocknest trench. b) Close-up image of Rocknest <150 µm sample [7] . . . 6
2.4 Particle size distribution of JSC-Mars-1 and other Martian regolith simulants [31] . . . 8
2.5 Thermal conductivity of JSC-Mars-1 simulant under different pressures. Open diamonds: Seiferlin et al. [31], closed diamonds: Presley and Craddock [35]. The arrows indicate the pressure range on Mars, retrieved from [31]. . . . 9
2.6 Phenomena observed during sintering due to the driving force, adapted from [41] . . . 10
2.7 Densification stages of sintered powders . . . 10
2.8 Densification curve of powder compact, including stages of sintering [41] . . . 10
2.9 Sintering densification mechanisms, adapted from [42] . . . 10
2.10 Spark plasma sintering machine in basic configuration, adapted from [46] . . . 12
2.11 Biaxial compression tests for disk-shaped specimen. Adapted from [53]. . . . 13

3.1 Image of MGS-1 Martian regolith simulant [62] . . . 15
3.2 Steps in the particle shape analysis process . . . 18
3.3 Charts of roundness vs sphericity for particle shape characterisation, adapted from [64–66] 19
3.4 Components and schematic representation of the sample assembly used during sintering 21
3.5 Sintering profile including stage indications . . . 23
3.6 Schematic representation of the data used to determine the sintering onset and saturation 24
3.7 Ball-on-ring test schematic . . . 25
3.8 Schematic overview of ball-on-ring testing fixture . . . 26
3.9 Schematic overview of a) support ring placement and b) sample alignment . . . 26
3.10 Specimen deflection data correction by using the bench deflection measurement . . . 27

4.1 Particle sizes of MGS-1 powder as determined from EDS images . . . 31
4.2 Analysed particle shapes from sieved MGS-1 powders . . . 32
4.3 Box plots of shape descriptors for a) circularity, b) aspect ratio and c) roundness . . . 32
4.4 Particle size distribution of as received MGS-1 . . . 33
4.5 SEM images of additive materials with a) aluminium powder and b) bismuth oxide . . . 33
4.6 MGS-1 heat flow and mass loss upon heating . . . 34
4.7 Apparent chemical reaction in MGS-1 during heating (shaded area) . . . 35
4.8 Mass spectrometry map of the TGDMA experiment performed on baseline MGS-1 powder 35
4.9 Calculated specific heat capacity for baseline MGS-1 simulant powder . . . 36
4.10 XRD patterns for baseline regolith and constituent minerals . . . 36
4.11 XRD patterns for baseline as well as enriched sintered regolith at different temperatures 37

5.1 Microscopy images of sintered baseline samples at different sintering temperatures and pressures. Failure loads for each sample are included. . . . 39
5.2 The effect of sintering temperature on the densification of sintered baseline MGS-1. Lines indicate samples sintered at equal pressures. . . . 40
5.3 Sintering temperature effect on the Young's modulus of sintered MGS-1. Lines indicate samples sintered at equal pressures. . . . 40
5.4 Sintering temperature effect on the biaxial strength of sintered MGS-1. Lines indicate samples sintered at equal pressures. . . . 41
5.5 Effect of sintering temperature on material behaviour of baseline sintered samples . . . 42
5.6 The effect of particle size on the densification of baseline sintered MGS-1 . . . 42
5.7 Particle size effect on the Young's modulus of sintered baseline MGS-1 . . . 43
5.8 Particle size effect on the biaxial strength of sintered baseline MGS-1 . . . 43
5.9 Effect of particle size on material behaviour of baseline sintered samples . . . 43
5.10 The effect of the dwell cycle on the densification of sintered baseline MGS-1 . . . 44
5.11 Dwell cycle effect on the Young's modulus of sintered baseline MGS-1 . . . 44

5.12 Dwell cycle effect on the biaxial strength of sintered baseline MGS-1 45
5.13 Effect of dwell cycle on material behaviour of baseline sintered samples 45

6.1 Effect of 2.5wt% and 5 wt% aluminium additive on the densification of sintered MGS-1 . 48
6.2 Improvement in densification for aluminium enriched samples as compared to sintered baseline MGS-1 48
6.3 Effect of 2.5wt% and 5 wt% aluminium additive on the stiffness of sintered MGS-1 . . . 48
6.4 Improvement in Young's modulus for aluminium enriched samples as compared to sintered baseline MGS-1 48
6.5 Effect of 2.5wt% and 5 wt% aluminium additive on the biaxial strength of sintered MGS-1 49
6.6 Improvement in biaxial strength for aluminium enriched samples as compared to sintered baseline MGS-1 49
6.7 Effect of 2.5wt% and 5 wt% bismuth oxide additive on the densification of sintered MGS-1 50
6.8 Improvement in densification for bismuth oxide enriched samples as compared to sintered baseline MGS-1 50
6.9 Effect of 2.5 and 5 wt% bismuth oxide additive on the Young's modulus of sintered MGS-1 50
6.10 Improvement in Young's modulus for bismuth oxide enriched samples as compared to sintered baseline MGS-1 50
6.11 Effect of 2.5 and 5 wt% bismuth oxide additive on the biaxial strength of sintered MGS-1 51
6.12 Improvement in biaxial strength for bismuth oxide enriched samples as compared to sintered baseline MGS-1 51
6.13 The effect of additive weight percentage on densification 52
6.14 The effect of additive weight percentage on the Young's modulus 52
6.15 The effect of additive weight percentage on the biaxial strength 53
6.16 The effect of additive weight percentage on the material behaviour of sintered MGS-1 . 53
6.17 Biaxial strength vs material behaviour of sintered MGS-1 54

7.1 Sintering curve for the Young's modulus of sintered samples as a function of the sample relative density 57
7.2 Sintering curve for the biaxial strength of sintered samples as a function of the sample relative density 58
7.3 Flexural strength vs required additional material for Martian regolith base materials . . . 58

B.1 Bench compliance indentation images used for data correction 78
B.2 Strength of the zirconia reference samples 78
B.3 Strength of the mortar reference samples 79
B.4 Stiffness of the soda-lime glass reference samples vs sample thickness 79
B.5 Strength of the soda-lime glass reference samples vs sample thickness 79
B.6 Biaxial strength of soda-lime glass specimen vs piston velocity as compared to literature [88] 80
B.7 Effect of the compression test set-up, with a) the long set-up, b) the short and c) the results of tested samples. 80
B.8 Differences caused by the stress range correction implementation on the Young's modulus and the biaxial strength 81
B.9 Sensitivity of the biaxial strength to the formula variables 82

List of Symbols

ν	Poisson's ratio	-
ρ	Density	g cm^{-3}
ρ_g	Geometric density	g cm^{-3}
ρ_r	Relative density	%
ρ_t	Theoretical density	g cm^{-3}
σ	Biaxial strength	MPa
ΔT	Change in material temperature	°C
a	Circular support hole radius	mm
b	Contact radius	mm
b_{eq}	Equivalent contact radius	mm
c_p	Specific heat capacity	J/g°C
F	Force	N
m	Mass	g
n	Number of data points	-
P	Applied load	N
P	Pressure	MPa
P_{dwell}	Dwell pressure	MPa
R	Sample radius	mm
r	Loading ring diameter	mm
$R2$	Coefficient of determination	-
T	Temperature	°C
t	Sample thickness	mm
T_0	Initial material temperature	°C
T_g	Glass transition temperature	°C
T_m	Melting temperature	°C
T_{dwell}	Dwell temperature	°C
V	Volume	cm^3
w	Deflection	mm
z	Hertz contact radius	mm
wt%	Weight percent	%

List of Abbreviations

AMU	Atomic Mass Unit
ASTM	American Society Test and Material
AUC	Area Under the Curve
BoR	Ball-on-Ring
COD	Crystallography Open Database
DC	Direct Current
DMA	Dynamic Mechanical Analysis
DSC	Differential Scanning Calorimetry
EDS	Energy Dispersive X-ray Spectroscopy
FAST	Field-Assisted Sintering Technique
HIP	Hot Isostatic Pressing
HP	Hot Pressing
ISRU	in situ resource utilisation
LOI	Loss on Ignition
MER	Mars Exploration Rover
MGS-1	Martian Global Simulant - 1
MTI	Mars Transfer Insertion
PSD	Particle Size Distribution
RoR	Ring-on-Ring
rpm	rotations per minute
SEM	Scanning Electron Microscopy
SPS	Spark Plasma Sintering
SRU	Space Resource Utilisation
TGA	Thermogravimetric Analysis
TGDMA	Thermogravimetric Dynamic Mechanical Analysis
XRD	X-ray Diffraction
XRF	X-Ray Fluorescence Spectrometry

1 Introduction

Over the past decade the interest in space exploration and extra-terrestrial human settlement has dramatically increased. This is, in part, due to the active missions from space agencies such as NASA and ESA trying to bring back man to the Moon and beyond after the 50-year anniversary of the Apollo moon landings, as well as to commercial companies such as SpaceX. Due to their proximity, the Moon and Mars are generally seen as the first bodies to permanently settle upon. The reasons for going to these places are numerous from a scientific perspective, ranging from efforts to find life on different plants, to understanding the formation of the solar system. In the overall timeline, the Moon is considered a stepping stone on the way to Mars. However, SpaceX already has the intention of landing a crewed mission to Mars as early as 2026 [1]. Before such missions can be undertaken, research is needed in order to prepare for the eventual arrival. Most research is aimed at mitigating the effect of the space environment and ensure safe, habitable conditions for humans. To this effect, habitats will need to be created to protect inhabitants from threats such as radiation (for example solar flares), low pressure (or even vacuum) conditions or even (micro)meteorite impacts.

1.1. The Need for Extra-Terrestrial Construction

Habitats can be divided into several different categories [2]. The first, Type I habitats, are structures manufactured on Earth and fully usable when landed on site. Examples of this type are hard-shell structures. Type II structures are habitats constructed on Earth and assembled/deployed on site. This category contains, for example, inflatable structures. Finally, Type III structures are structures fully manufactured at the destination with minimal resources from Earth. In the early stages, the habitats are most like of the first or second category, with some local resource use. However, importing material from Earth is very costly. This is both due to the large costs involved in launch, as well as the relatively small amount of material that can currently be sent to the Moon and beyond. Therefore, maturing technologies suitable for creating habitats using local resources is an ongoing research topic. In parallel to these, other research efforts focus on generating the energy required to produce materials, as this infrastructure is also lacking on site. Possible energy generation strategies include electric energy obtained from solar panels or thermal energy from nuclear reactors.

1.2. The Importance of Using Local Resources

Not only is the use of local resources sensible from a financial perspective, it can also be used for a variety of other aspects for maintaining a sustained presence. This is because local resources, with the right processing methods, can be made into water, energy or other useful compounds, for example fuel, as well as construction material as mentioned above.

The most abundant local resource on extra-terrestrial bodies is *regolith*. Regolith is defined as the loose upper layer of material on the surface of planetary bodies. It is a loose granular material that mostly consists of different minerals. The composition of regolith changes from celestial body to body. Therefore, separate research for each regolith composition needs to be performed. For these types of research purposes, often an analogue to the actual material is used. This is due to scarcity or even unavailability of the actual material. For example, no sample return mission to Mars has yet been completed [3, 4] and hence no native Martian regolith is available. Such an analogue material is called a *simulant* and generally tries to mimic the physical and/or chemical properties of a certain regolith. For Martian regolith, the mineralogical composition was investigated by landers/rovers like Curiosity's CheMin experiment. This instrument performed the first X-ray diffraction experiment, resulting in the identification of several minerals [5]. Additional chemical information was obtained using the Sample Analysis at Mars (SAM) suite [6]. Physical properties, such as the particle shape, are determined,

for example, using imaging. An example is the MAHLI instrument aboard Curiosity [7]. Collection, processing, storage and consumption of materials sourced from raw local resources falls under the term in situ resource utilisation (ISRU). The concept of ISRU has inspired a large research effort into maturing technologies for sustained extra-terrestrial presence using local resources.

1.3. Manufacturing Methods Using Regolith (simulant)

In order to use regolith for structural purposes, the loose powder needs to be stabilised. This can be achieved using several different processing methods. One of the most explored methods is by using a binder. Different weight fractions of binder can be combined in order to create a stabilised material. Alternatively, the regolith can be melted and cast into a usable shape. However, both of these methods have significant downsides. Current research into the binder-based option requires large amounts of binder materials, which mostly needs to be imported to site. The melting route requires large amounts of energy, which is also scarce.

An alternative method to stabilise regolith is by sintering. Sintering is a consolidation method that heats the material to typically 50 to 80% of the melting temperature [8]. Hence, it requires less energy compared to complete melt casting. Additionally, 100% local material can be sintered, without any imported additive required. However, additives can be used to improve the sintering process and results. Additives that aid in the sintering process, for example by lowering the processing temperature or improving results, are called *sintering aids*. Therefore, sintering regolith with small amounts of additive is potentially an interesting compromise between the two methods.

1.4. Research Questions

Currently, most research is aimed towards the processing of Lunar regolith (simulants) and little towards processing Martian regolith. Specifically in the case of sintering regolith, little is known about the effect of sintering aids on the processing and properties of sintered material. In general, more understanding of the sintering of Martian regolith is required. Therefore, the objective of this thesis is to investigate the effect of sintering aids on sintered sample properties by using a novel mechanical testing method, the ball-on-ring compression test, with the aim of applying the result to determine the feasibility of using sintered materials for structural purposes on Mars. For this thesis, the chosen sintering method is Spark Plasma Sintering (SPS).

Based on this research objective, several research questions can be defined:

RQ1. What is the effect of SPS process parameters on the densification and mechanical properties of sintered Martian regolith simulant?

RQ2. What is the effect of sintering aids on the densification and mechanical properties of sintered Martian regolith simulant?

RQ3. What material property levels need to be reached in order to use sintered Martian regolith for structural purposes?

RQ4. Can sintered Martian regolith simulant, with or without sintering aids, be used to create structural material suitable for Martian infrastructure?

1.5. Thesis Structure

To provide an answer to the research questions posed above, the remainder of this thesis has been given the following structure. First, additional background and literature information is provided in Chapter 2. Next, Chapter 3 discussed the different materials and methods that are used. Chapter 4 presents the result of the MGS-1 powder characterisation, which is the Martian soil simulant used during this thesis. Next, the effect of the sintering parameters and material on physical and mechanical properties of sintered samples is discussed in Chapter 5. Next, in Chapter 6, the effect of additives on the physical and mechanical properties are presented. Chapter 7 evaluates the results of the previous three chapters by discussing six different aspects. These are the fitness of MGS-1, the validity of the obtained results, the effect of SPS settings and particle size, the effect of additive material and amount, the performance compared to literature and the link to Martian applications respectively. Finally, conclusions and recommendations can be found in Chapter 8 and Chapter 9 respectively.

2

Background and Literature

Additional background information and literature data is required in order to answer the research questions stated above. That information is presented in this chapter. First, in Section 2.1, additional information on in situ resource utilisation is given, together with considerations that lead to restraints on the amount of additive used. Next, in Section 2.2, additional information on Martian regolith is presented, both for actual Martian material and simulants. This is followed by an in-depth discussion of sintering in Section 2.3. Finally, a discussion on the mechanical testing from disk-shaped samples is presented in Section 2.4.

2.1. In-situ Resource Utilisation (ISRU)

A variety of areas are currently being researched in order to prepare for prolonged extra-terrestrial presence. Part of these efforts are aimed at extra-terrestrial construction for a variety of different applications, from habitat construction to the creation of infrastructure. In this section, first the general flowsheet for any space resource utilisation process is introduced, followed by a discussion on the link between ISRU and structural materials. Next, important aspects for ISRU in general are discussed. Finally, the current launch capabilities and habitat requirements are presented and used to determine a maximum additive amount to be used throughout the rest of this research.

2.1.1. Space Resource Utilisation (SRU) Universal Flowsheet

In order to use local resources, first, these resources need to be gathered. Any resource gathering for Space Resource Utilisation (SRU) processes resemble terrestrial mining operations. Three main processes can be defined: excavation, beneficiation and extraction. The general material flow through these processes can be described by the flowsheet in Figure 2.1 [9].

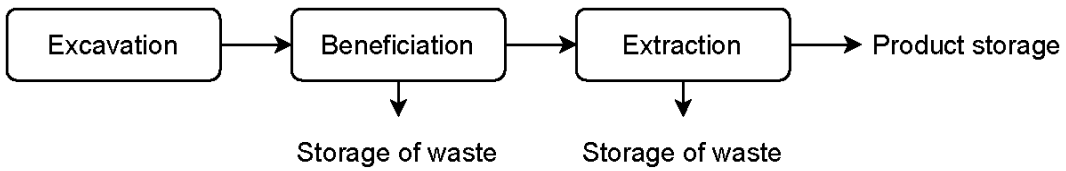

Figure 2.1: *Universal flowsheet for SRU processes, adapted from [9].*

Several processing steps (beneficiation and extraction) are included in this flowsheet. For early applications, however, these processes will be minimally implemented. Therefore, for early application, excavated regolith with minimal processing should be used where possible.

2.1.2. ISRU and Structural Materials

As mentioned above, in the early stages of exploration most available material will only be excavated. Therefore, any application of this regolith needs to use the baseline material. Most likely, this material will be used to protect any potential Type I or II habitats on site. In order to do this, two options are available. The first is by covering the structure with a loose layer of regolith, the second is to stabilise the material and provide protection using constructed materials. Stabilised regolith can also be used to create infrastructure, like roads or exhaust protection walls.

In order to stabilise regolith and create structural materials, several different options exist. The most commonly used ones are binder-based, melting and casting and sintering. However, not all of these

production methods are equally suitable due to mass and energy requirements. Selecting the proper processing method requires the careful evaluation of important ISRU aspects.

2.1.3. Important Aspects for ISRU

As introduced above, ISRU is thought to be one of the most important aspects for extra-terrestrial construction. This philosophy tries to use as much locally sourced material as possible, but several challenges for this approach to extra-terrestrial construction exist.

Available Materials

The first challenge is the available materials. On site, no refined materials are available. The most abundant resource available is *regolith*, a granular material with location dependent mix of minerals (see the definition in the Introduction). Next to regolith, other naturally available materials might be present or relatively readily available. For example, it is expected that water is more readily available on Mars closer to the polar regions.

Initially, regolith is most likely to be used in an unrefined form. Minimal processing, such as grinding or mixing, could be possible. In the longer term, regolith can be a source of derived resources such as metals. However, the main hurdle before this can be realised is the available energy and infrastructure for material processing.

Energy and Infrastructure

On Earth, energy and infrastructure to create construction material is readily available. Power plants, using a variety of energy sources, supply power to a host of different machines capable of creating a large number of different materials. Large networks of infrastructure supply the needed raw materials to the production sites. In space, these resources are unavailable. Few fuel sources are available outside Earth to produce energy, and any machinery needs to be imported from Earth. One well understood method of producing energy in space is by using solar panels. This is currently applied to power most of the existing space objects such as satellites and rovers. The second method is via nuclear energy. Radioisotope Thermoelectric Generators, or RTGs, are relatively lightweight compact power supplies that can be used for decades due to their high reliability. Both methods rely on material imported from Earth, and therefore one limiting factor is the amount that can be sent to site by the current generation of launchers.

Another important aspect for off-site materials production is the amount of energy required. Large solar arrays are needed to produce sufficient energy in order to sustain a habitat or settlement. Even for nuclear power, current state-of-the-art solutions are unable to provide sufficient energy. However, it is expected that the latter will prove most promising for the future.

Automation

Another important aspect of ISRU is automation. If it is possible to use local resources autonomously in order to create materials and products, it then becomes possible to automate the creation of infrastructure and shelters before any human crew arrives. Preparation for the arrival can start decades before arrival, slowly constructing the required facilities.

Automation can be achieved in a single step process, for example by using additive manufacturing solutions, but also using multi-step processes that separate production and assembly stages.

2.1.4. Design Constrains from ISRU

The availability of on-site resources and available energy for processing can limit operations and impose constrains on any ISRU inspired design concept. Similarly, launcher limitations (predominantly volume and cost) can also impose design constrains. One constraint, for example, could be the amount of material able to be imported from Earth. The amount of material required from the Earth is called the required *upmass*. Spedding, Nuttall, and Lim investigated the energy and mass requirements for constructing a thermally processed (sintered) radiation shield for use on a Lunar habitat. They investigated current research using processed Lunar regolith and the required upmass for each material. This yielded relations for the weight percent additive and the required binder upmass. For their investigation, a reference habitat with shield volume of 137.2 m^3 was chosen, but larger shield volumes were also analysed depending on the required shielding [10].

Assuming that these values also serve as a first estimate for the shield volume of a habitat on Mars, their estimate and relations can be plotted against the capabilities of current launch vehicles capable of Mars Transfer Insertion (MTI). This graph is shown in Figure 2.2.

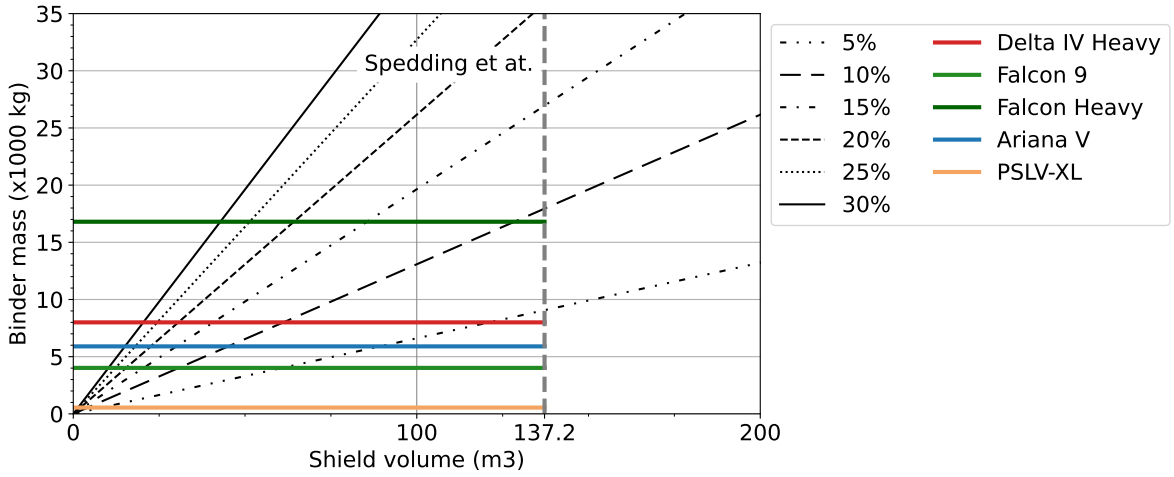

Figure 2.2: *Additional binder upmass per shield volume increase, using wt% values commonly found across literature, including lines indicating current launcher limitations. Adapted from [10], launcher data from [11–14]*

From the graph it becomes clear that the current launch capabilities are by far not suitable to reach the required binder upmass requirements for the proposed shield volume. Only the Starship system, according to SpaceX, would be capable of such performance. For operational launchers, the carrying capacity is much lower. Therefore, for this research, the upper limit for binder mass has been set to 5wt% as this amount of binder upmass seems feasible with current launch capabilities.

2.2. Martian Regolith

This thesis specifically focuses on creating structural materials for use on Mars. Therefore, the most abundant resource available is Martian regolith. In this section, Martian regolith is introduced in more detail. Next, the chemical and physical properties of Martian regolith are discussed.

Unfortunately, as of the time of writing of this thesis, no sample return mission to Mars has been undertaken. Therefore, no actual Martian regolith material is available. However, mineral depositions on Earth that are akin to Martian material can be used to create analogue materials. These materials are known as simulant and generally represent the chemical, physical or a combination of both properties of actual Martian material. This section is concluded by a discussion on available Martian regolith simulants.

2.2.1. Martian Regolith Description

The first planned sample return mission involves the Mars 2020 (”Perseverance”) rover the recently landed on the red planet. This rover will collect and store samples which will be transported back to Earth by a collaborative effort between NASA and ESA [15]. The returned samples will be able to drastically improve our understanding of the Martian regolith. Therefore, current knowledge about the Martian regolith is mostly obtained from remote sensing missions, lander missions and several rovers. Especially the latter category provided insight into the material. An image of the Martian soil, taken by the Curiosity rover, can be seen in Figure 2.3.

2.2.2. Properties of Martian Regolith

Properties of Martian regolith can be split into several different categories. First, the chemical composition is discussed, followed by the physical properties and finally the thermal properties.

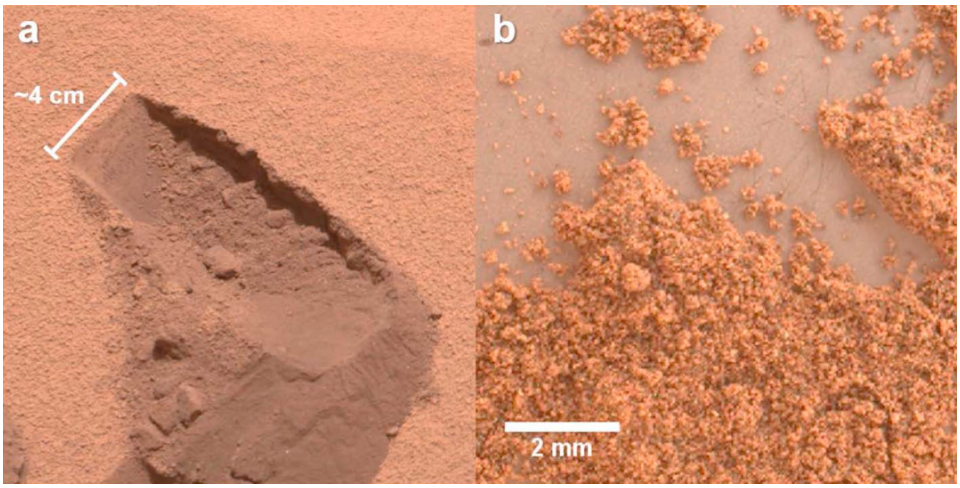

Figure 2.3: *Martian soil as photographed by the Curiosity rover. a) photograph of the Rocknest trench. b) Close-up image of Rocknest* <150 µm *sample [7]*

Chemical Composition of Martian Regolith

The Martian regolith mainly consists of basaltic soils with minerals similar to the Moon's regolith. The average bulk composition of these soils can be seen in Table 2.1. The different measurements were obtained for locations from the Mars Exploration Rover (MER) Curiosity (Gale Crater) [16], the MER Opportunity (Meridiani Planum) [17] and the MER Spirit (Gusev Crater) [17].

Table 2.1: *Average bulk composition of basaltic soils in the Gale Crater, Meridiani Planum and Gusev Crater. Adapted from [18], using original data from [16, 17]*

Oxide	**Gale Crater average [%]**	**Meridiani Planum average [%]**	**Gusev Crater average [%]**
SiO_2	43.16	46.14	46.32
Al_2O_3	9.16	9.39	10.14
CaO	7.08	6.95	6.35
FeO_T	19.33	18.17	16.04
MgO	8.6	7.42	8.61
Na_2O	2.72	2.23	3.01
TiO_2	1.05	1.03	0.87
K_2O	0.5	0.49	0.44
P_2O_5	0.92	0.85	0.82
MnO	0.42	0.37	0.32
Cr_2O_3	0.46	0.4	0.35
Cl	0.77	0.66	0.72
SO_3	5.83	5.91	6.01
Total	100	100	100

Physical Properties of Martian Regolith

Martian regolith is known to predominantly consist of small grains in the range of 20 µm to 45 µm [19]. Nevertheless, a large particle size variation exists. For example, data from the Viking landing sites processed by Shorthill et al. showed a Particle Size Distribution (PSD) between 10 µm and 2000 µm for material at or near the surface [20]. Weitz et al. identified a bimodal particle size distribution at Meridiani Planum with one population mode given by particles <125 µm and the other by particles between 1 mm and 4.5 mm in size [21]. A similar bimodal distribution was observed in the Gale Crater with a mode at 100 µm to 250 µm and the second at 500 µm to 2200 µm [7]. The same study showed that the particle

shapes for all grains are subangular to rounded with a high degree of circularity, which indicates an extensive history of abrasion [7].

Mechanical Properties of Martian Regolith
Bulk densities for Martian regolith have also been determined by the different Viking Landers and MERs. Measured bulk density values vary between 1150 kg m^{-3} for drift material to 1636 kg m^{-3} for crusty material [22]. The low bulk densities of the drift materials infer a large amount of porosity. Estimates for the porosity of Martian regolith are few, but Viking Lander suggests a porosity between 31 % and 58 % for grain densities of 2600 kg m^{-3} and bulk densities between 1100 kg m^{-3} and 570 kg m^{-3} [23].

Thermal Properties of Martian Regolith
The thermal properties of Martian regolith material depend on the bulk density and the porosity of the material. To give an estimate of the thermal properties of regolith, thermophysical properties obtained from orbital data can be used. This data, together with relationships established in the laboratory, were used by Morgan et al. to estimate the thermal conductivity of Martian regolith. Their calculations showed a value between 0.017 W mK^{-1} and 0.048 W mK^{-1}, with a median value of 0.032 W mK^{-1} [24]. This corresponds to 150 µm to 170 µm unconsolidated grains [25].

2.2.3. Martian Regolith Simulant
Similar to actual Martian regolith, the chemical, physical and thermal properties of Martian regolith simulants are also documented. Especially the differences between actual and simulated material are important.

Chemical Properties of Martian Regolith Simulants
Several different Martian regolith simulants have been created over the past decades. The chemical composition of some of the most common Martian regolith simulants is shown in Table 2.2.

Table 2.2: *Chemical composition of several Martian regolith simulants. Values in percent of total, data sources noted in table.*

Simulant	**JMSS-1 [%]**	**JSC-Mars-1 [%]**	**MMS [%]**	**TJ-1 [%]**	**MGS-1 [%]**	**OUEB-1 [%]**
Source	**[26]**	**[27]**	**[28]**	**[29]**	**[3]**	**[30]**
Oxide						
SiO_2	49.28	39.25	49.4	47.7	50.8	50.44
Al_2O_3	13.64	21	17.1	16.2	8.9	7.10
CaO	7.56	5.5	10.45	8.21	3.7	9.52
FeO_T	16	13.5	10.87	10.75	13.3	19.32
MgO	6.35	3	6.08	5.04	16.7	10.71
Na_2O	2.92	2.25	3.28	4.92	3.4	1.33
TiO_2	1.78	3.5	1.09	2	0.3	0.28
K_2O	1.02	0.55	0.48	2.29	0.3	0.71
P_2O_5	0.3	0.8	0.17	0.58	0.4	0.52
MnO	0.14	0.25	0.17	0.15	0.1	0.19
Cr_2O_3	–	–	0.05		0.1	0.179
SO_3						0.448
Total	98.99	89.6	99.14	97.84	98	100.73

Physical Properties of Martian Regolith Simulants
The grain size and shape of Martian regolith simulants are determined by the processing methods of the raw material. The characteristics of multiple simulants have been investigated for these two parameters. All of the current Martian simulant samples exhibit very angular to sub-angular shapes with a low circularity [22, 28, 30], as opposed to the rounded shapes observed for actual Martian material [7]. The particle size distribution for several simulants, including JSC-Mars-1, can be seen in Figure 2.4.

It is observed that the particle size varies between 1 µm and 1000 µm, which falls within the values obtained for Mars.

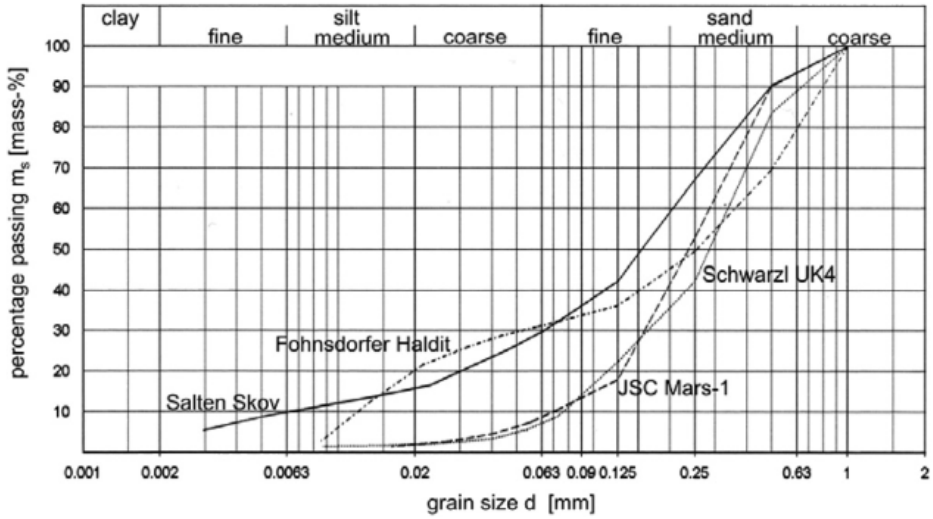

Figure 2.4: *Particle size distribution of JSC-Mars-1 and other Martian regolith simulants [31]*

Mechanical Properties of Martian Regolith Simulants
The mechanical properties of several simulants have been investigated [22, 30, 32, 33]. Delage et al. investigated three different simulants (MSS-D, Mojave simulant and Eifelsand) and provided a value for the Poisson's ratio based on measured seismic velocities. These seismic velocities were measured in a triaxial compression test using different confining pressures. A value of 0.22 was determined. In addition, Delage et al. calculated the Young's modulus using these seismic velocities and the regolith density. A range of 43.5 MPa to 51.2 MPa for the Young's modulus was calculated for densities ranging between 1300 kg m^{-3} and 1533 kg m^{-3} [33].
The bulk density of Martian regolith simulants is reported to range between 835 kg m^{-3} for JSC Mars-1 [32] and 1950 kg m^{-3} for OUHR-1 [30]. Ramkissoon et al. also determined the porosity of their new Martian regolith simulants. They obtained values ranging between 47.7 and 51.7% for bulk densities of 1950 kg m^{-3} and 1620 kg m^{-3} respectively [30].

Thermal properties of Martian Regolith Simulants
Several researchers have tried to investigate the thermal properties of Martian regolith simulant under Martian conditions. In order to assess the use of regolith for 3D printing, Goulas et al. assessed the melting temperature of JSC-MARS-1A. They reported several peaks upon heating, with an overall reported melting temperature of up to 1330 °C [34]. Another investigated property is the thermal conductivity. Because the thermal conductivity depends on the pressure, several measurements at different pressures were performed. The measurements for the thermal conductivity of JSC-Mars-1 simulant in low pressure conditions and absence of water are shown in Figure 2.5. For the pressures on Mars, the thermal conductivity was found to range approximately between 0.055 W mK^{-1} and 0.18 W mK^{-1}.

2.2.4. Structural Material Made From Regolith

Regolith can be used in a variety of methods in order to create a stabilised material suitable for structural application. Past examples of successfully created material include cast lunar regolith [36], sulphur concrete [37] and composites made using a variety of binders, for example polyethylene [38]. The production processes by which these materials are created can be grouped into different categories. The first is binder-based methods. Binder-based manufacturing requires a large amount of upmass in terms of additive material and processing infrastructure. The second category is melt-based processes.

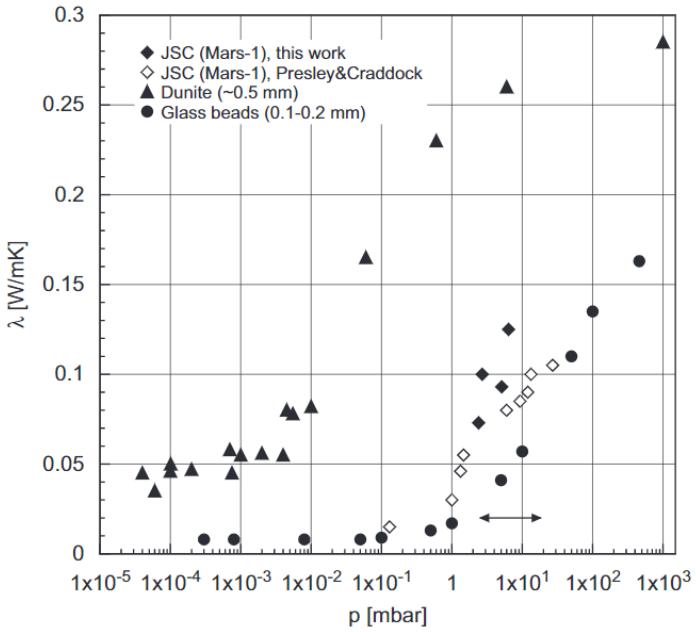

Figure 2.5: *Thermal conductivity of JSC-Mars-1 simulant under different pressures. Open diamonds: Seiferlin et al. [31], closed diamonds: Presley and Craddock [35]. The arrows indicate the pressure range on Mars, retrieved from [31].*

Examples of this type of process are cast bricks or drawn glass fibres. This production method requires less upmass (only infrastructure as opposed to both infrastructure and binder material), but has some significant downsides. For example, the required energy to melt the material is very high and cool down needs to be controlled accurately to avoid cracking. As an alternative to melt-processing, sintering can be used. Sintering requires lower temperatures then melting, making the energy requirements less severe, and can be performed with small to no amounts of additive. Therefore, it could potentially be a suitable method for creating materials on Mars. Some studies on sintered Lunar regolith can be found in literature [39], but only few exist for sintered Martian regolith [40].

2.3. The Sintering Process

Most current research into sintering for extra-terrestrial applications has focused on conventional sintering techniques, but other techniques that could result in improved results are possible. In this section, first, a general introduction to sintering is given. Next, the distinction is made between pressure-assisted and pressure-less sintering and the differences between the two are discussed. Following this, liquid phase sintering and its differences are presented. The effect of sintering aids is discussed after that, including possible sintering energy reduction effects. Finally, the spark plasma sintering technique used throughout this research is introduced.

2.3.1. Introduction to Sintering

As mentioned above, sintering occurs below the melting temperature of a material and fuses individual particles together. This process is often used for a wide range of materials, including metals and ceramics. As mentioned in the Introduction, the material is commonly heated to temperatures between 50-80% of the melting temperature. The driving force for sintering is the reduction of total interfacial energy as it is thermodynamically more favourable to lower the surface energy of individual particles [41]. This total reduction occurs via two methods: densification and grain growth, see Figure 2.6. Two types of sintering are generally defined, solid state sintering and liquid phase sintering. During solid state sintering, no liquid phase is formed during the process. Another distinction can be made between pressure-less and pressure-assisted sintering.

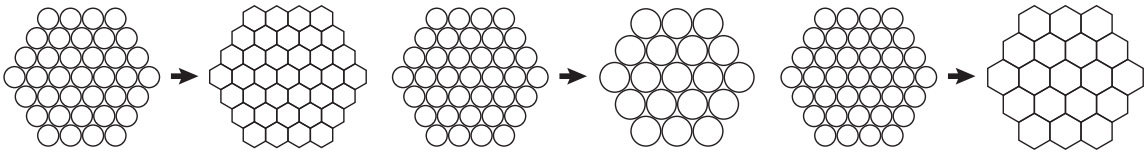

(a) *Densification* **(b)** *Coarsening* **(c)** *Densification and Coarsening*

Figure 2.6: *Phenomena observed during sintering due to the driving force, adapted from [41]*

2.3.2. Pressure-less vs Pressure-assisted Sintering

The general distinction between pressure-assisted and pressure-less sintering can be made as mentioned above. In this subsection, both of these methods are discussed.

Pressure-less Sintering

The most commonly used solid-state sintering process is Hot Pressing (HP). In this method, a powder compact (green body) is created by shaping powder in a mould. Next, the powder compact is heated in an oven until sintering temperatures are reached.

The driving force for sintering is produced by the thermodynamic processes discussed above. Densification occurs in several stages, see Figure 2.7. Initially, powders are compacted together. In the first stage, due to several densification mechanisms, mass transport between particles starts taking place and 'necking' occurs, fusing individual particles together. This is followed by pore reduction. Finally, a consolidated material is obtained in which (some) residual pores can be present. Especially the pore reduction state in which isolated pores are closed requires the most amount of sintering time. An overview of the densification curve including sintering stages can be seen in Figure 2.8 [41].

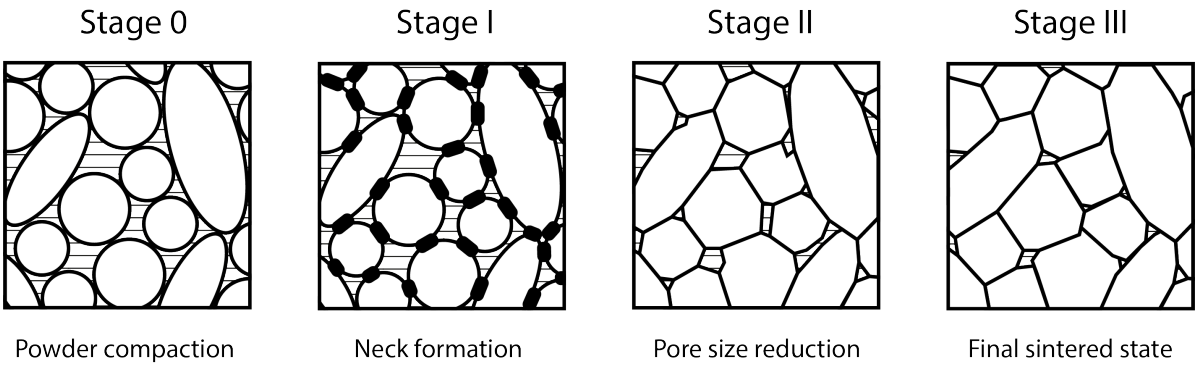

Figure 2.7: *Densification stages of sintered powders*

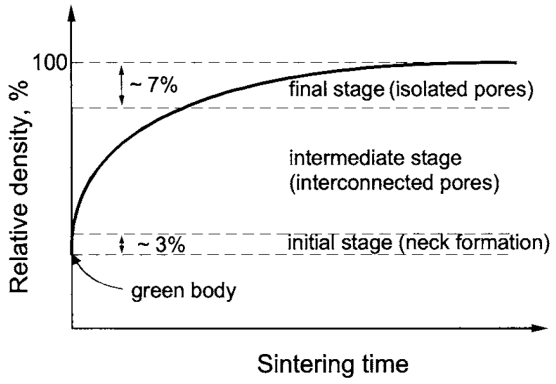

Figure 2.8: *Densification curve of powder compact, including stages of sintering [41]*

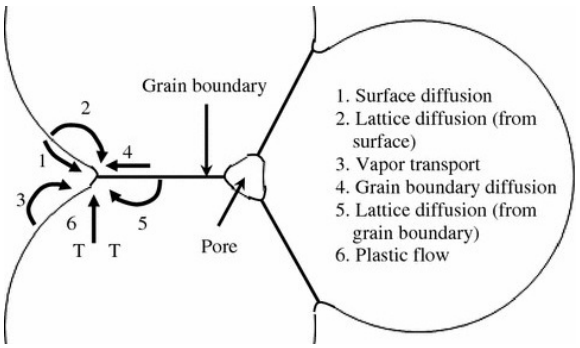

Figure 2.9: *Sintering densification mechanisms, adapted from [42]*

The densification mechanisms in solid-state sintering mentioned above can generally be grouped into six different categories. Shown in Figure 2.9, these are surface diffusion, lattice diffusion (from surface), vapour transport, grain boundary diffusion, lattice diffusion (from grain boundary) and plastic flow [42].

Several of these densification mechanisms can occur at the same time, and the dominant mechanism depends on sintering temperature, grain size and time for a material system [8, 41].

Pressure-assisted Sintering

In pressure-assisted sintering processes, such as Hot Isostatic Pressing (HIP), the Field-Assisted Sintering Technique (FAST) or Spark Plasma Sintering (SPS), pressure is applied during sintering to aid in densification. In the case of HIP, the pressure is applied by a gas, whereas it is mechanical in FAST.

In general, the densification rate always increases with increasing sintering pressure. This is due to the increase in driving force and kinetics. In addition to the densification mechanisms mentioned above, plastic deformation and creep can be major densification mechanisms during pressure-assisted sintering. However, for ceramic samples, diffusion is the dominant mechanism even under high applied external pressures. Diffusion under applied external pressure resembles diffusional creep.

2.3.3. Liquid Phase Sintering

During liquid phase sintering a liquid phase is formed. This liquid phase can be formed in-situ or ex-situ. In in-situ formation, compounds in the powder compact react to form a liquid phase. In ex-situ liquid sintering, a liquid phase is formed without internal reactions. The liquid phase allows fast mass transport through the liquid and hence micro-structural changes can occur fast.

Compared to solid state sintering, liquid phase sintering has several advantages. First of all, easier control of micro structure and a reduction in processing cost can be achieved [41]. Second, densification can be improved if the liquid phase has sufficient wettability with respect to the solid phase. This is due to improved bonding in brazing and soldering [41]. Alternatively, the effect of the liquid phase can be seen as infiltrating and filling pore spaces, thereby improving densification.

Liquid phase sintering can occur in both pressure-less and pressure-assisted sintering. However, in pressure-assisted sintering, the amount of liquid phase present in the sample cannot be too large if the mould geometry is not fully closed. Due to the uniaxial pressure applied during sintering, liquid material can possibly be forced out of the mould assembly, resulting in a melt-out.

2.3.4. Sintering Aids

Materials added to powders in order to enhance the performance of the sintering process and the obtained results are called *sintering aids*. Sintering aids are typically used to enhance the sinterability and control the microstructure [41]. This is achieved by reducing the sintering temperature and aiding in the reduction of pores via densification. Densification can be supported by introducing dislocations and enhancing diffusion [43]. For example, sintering Al_2O_3 with small amounts of MgO improves densification and suppresses grain growth [41]. Sintering aids can also be used to change the sintering conditions. For example, addition of a specific sintering aid can create a liquid phase during sintering, possibly allowing the sintering temperature and/or time to be reduced due to improved mass transport. However, the mechanisms of sintering aids are system dependent and therefore not fully understood [41].

2.3.5. Spark Plasma Sintering (SPS)

Spark Plasma Sintering is a pressure-assisted type of sintering, suitable for both solid-state and liquid phase sintering. Generally speaking, materials made using SPS exhibit superior properties compared to conventional techniques [44]. Therefore, sintering via SPS might produce better results and allow the investigation of the possible properties obtained from sintered Martian regolith.

The SPS system consists of a mechanical loading system that applies uniaxial pressuring on the die and sample during operation, a vacuum/gas atmosphere regulating system, a pulsed DC generator and position, temperature and pressure regulating systems [45]. The basic configuration of an SPS system is shown in Figure 2.10 [46].

Spark Plasma Sintering (SPS), also known as the Field-Assisted Sintering Technique (FAST), uses low voltage (generally lower than 10 V), high pulsed Direct Current (DC) (typically 1 to 10kA) to generate the elevated temperatures necessary for sintering via Joule heating. Densification generally takes minutes as compared to hours for conventional HP technology [47]. This is due to the efficient transfer of

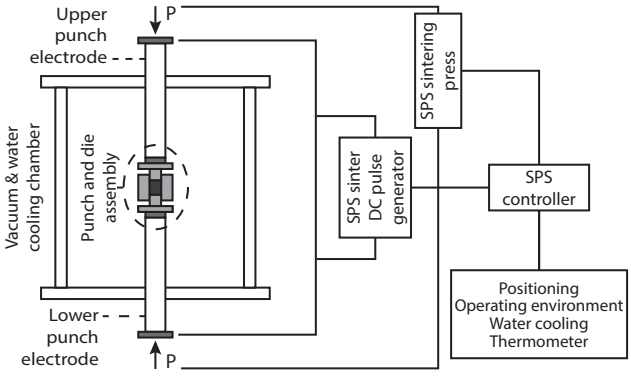

Figure 2.10: *Spark plasma sintering machine in basic configuration, adapted from [46]*

heat to the sample. In conventional methods, like HP and HIP, heat is transferred via radiation from the enclosing furnace and conduction from the furnace base to the sample, as opposed to conduction via the sample mould in SPS. Additionally, due to machine geometry, the SPS system allows for homogeneous heating of the sample assembly whereas conventional processes do not. Moreover, the sintering temperature can be lowered due to the applied pressure. Additional SPS process parameters include the ambient pressure during sintering, the ambient atmosphere during sintering (generally vacuum or inert gas) and DC pulse duration. Shorter operation times and lower sintering temperatures result in better control over grain size as compared to hot pressing [47].

SPS can be used to sinter a wide variety of materials. The heating method depends on the electrical resistance of the tool and sample material. In conductive samples, heat is directly generated via Joule heating within the samples. For non-conducting samples, a conductive tool needs to be used and the heat produced by Joule heating is transferred via conduction to the powder. During sintering, high heating rates up to 1000 °C min^{-1} can be achieved due to the compact geometry of the die and punches and the intimate contact between the sample and the mould. Standard cooling rates are between 150 °C min^{-1} and 400 °C min^{-1} under additional active gas cooling [48]. The geometry of the produced sample depends on the mould geometry. For this thesis, thin disk-shaped specimen are produced.

The sintering mechanisms involved result from the mechanical, thermal and electrical effect. The mechanical effect is due to the applied pressure applied during operation. The applied uniaxial pressure promotes particle rearrangement and increases packing efficiency, resulting in enhanced densification. The amplitude of the applied stress is limited by the high-temperature fracture strength of the loading system and pressing tool.

The first thermal effect comes from the availability of high heating rates. When the activation energy of the densification mechanism is higher than that of the dominant grain coarsening mechanism, rapidly reaching high sintering temperatures can enhance densification while delaying grain growth. Additionally, fast heating rates and short sintering times reduce the interaction between sample and tooling, minimising the risk of contamination of active materials [48]. Thermal gradients or non-uniform temperature distributions can occur within the material due to the non-uniform heating of the porous green body. Microscopic temperature gradients provide an additional driving force for diffusion known as Ludwig-Soret thermal diffusion [48]. Additionally, die size appears to effect thermal gradients. For small (approximately 12 mm) and large sample diameters (approximately 50 mm), the thermal gradients are within approximately 30K. However, for intermediate die sizes, thermal gradients can reach up to 70 K [49]. Local melting can be induced in the presence of large thermal gradients, aiding in the formation of necks between particles [50].

Experiments by Munir, Anselmi-Tamburini, and Ohyanagi showed that the current applied during SPS has a pronounced effect on mass transport. A decrease in the activation of migration of the defects is an example of the effect on sintering mechanisms [51].

2.4. Mechanical Testing From disk-shaped Specimen

In the section above it is explained that SPS results in thin disk-shaped specimen. Since the topic of the current research is focused on creating structural material from regolith, these samples need to be mechanically tested in order to assess their mechanical properties. Several testing methods exist in order to test for common such as compressive and flexural strength. Tensile tests are left out of the discussion as the intended application (construction) mostly entails compressive and flexural loads. In this section, several of these methods are briefly introduced and their applicability to disk-shaped samples discussed.

2.4.1. Uniaxial Compression Tests

Uniaxial compression tests are commonly performed on cylindrical or cube shaped specimen. In terms of cylindrical specimen, the diameter to thickness ratio is commonly 2:1 or larger. For the mould geometries and material available to the SPS process, no cylindrical samples could be created directly. Any cylindrical samples would have to be cut from a bigger disk, resulting in a lot of wasted material. For cubic samples, cubes of different sizes can be used. One commonly used dimension is 2x2x2 inches, which is impossible to make with our available material and mould sizes. Another option is to cut smaller cubes from disk-shaped samples. This, however, results in a lot of access material and inaccurate testing results due to the small cube sizes. Additionally, a large processing time is required in order to get the cube shaped samples ready for compression testing.

2.4.2. Bending (Flexure) Tests

In order to test the bending properties of materials, two different types of tests are commonly used. These are the three-point and four-point bending test respectively. These types of tests are commonly performed on bar shaped specimen. Of the two methods, the four-point bending test is commonly preferred as the three-point equivalent only subjects a small region to the maximum load. Hence, the observed load with the latter method is generally much higher. American Society Test and Material (ASTM) International standard C1161 covers the flexural strength testing of advanced ceramics [52]. In it, the minimum required sample size is set to 25x2x1.5mm. This would require at least a 30mm mould and large amount of cutting to produce the samples. Additionally, the required tolerances are also difficult to meet without extensive machining.

2.4.3. Multi-axial Flexure Tests

A different category of bending tests is multi-axial testing, in which the specimen is loaded in two or more directions simultaneously in order to determine the material response. Generally, these properties are different compared to uniaxial testing and correspond better to real life applications. For example, in the case of a Martian habitat or road, the loading conditions are biaxial as opposed to uniaxial. Therefore, it is interesting to look at some biaxial testing methods. Three methods will be discussed: the ball-on-three balls method, the ring-on-ring method and the ball-on-ring method. Images of the compression test set-up for these methods are shown in Figure 2.11.

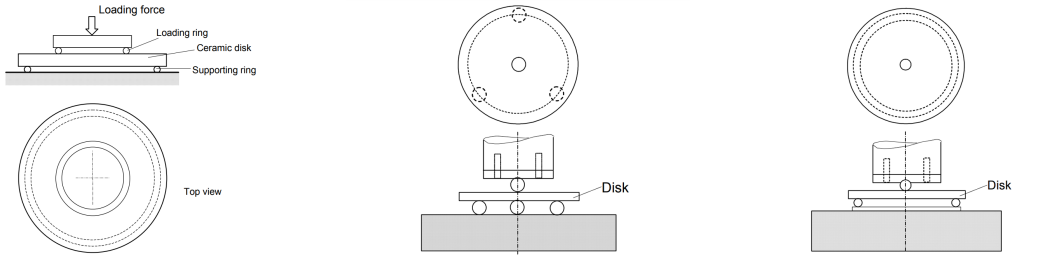

(a) *Schematic of the Ring-on-Ring compression test*

(b) *Schematic of the Ball-on-Three-Balls compression test*

(c) *Schematic of the Ball-on-Ring compression test*

Figure 2.11: *Biaxial compression tests for disk-shaped specimen. Adapted from [53].*

One advantage that all multi-axial flexure tests have over conventional flexural tests is the ability to support disk-shaped samples. This means no extensive cutting operations are necessary for sample preparation.

Ring-on-Ring Compression tests

In the Ring-on-Ring (RoR) test, a disk-shaped specimen is supported by a ring and loaded by a smaller, concentric loading ring [54, 55]. This testing method has been standardised [56] and is commonly used in the testing of ceramics and glass [53]. A schematic overview of the ring-on-ring test is shown in Figure 2.11a.

A well-defined stress state is obtained under ideal loading conditions, e.g., continuous contact between the two rings and the test specimen. To facilitate contact, and to reduce friction, often compliant layers are used between the rings and the sample. If the continuous contact between loading rings and samples is absent, an incorrect stress distribution will result. Therefore, samples should be parallel and flat (plane-parallel) in order to ensure proper loading.

Ball-on-Three-Balls Compression tests

A simplified version of the ring-on-ring test is the ball-on-three-rings test. In this test, the support ring is replaced by three balls and the loading ring by a fourth [57], see Figure 2.11b. This simpler set-up reduces friction but also decreases the effective area experiencing the maximum stress. Due to the sample only being supported on three points, with the loading on a fourth, samples that are less plane-parallel can be tested. For this type of test, Börger, Supancic, and Danzer investigated the possible errors for this testing method and noted that the specimen thickness has the most influence on the calculated strength. Therefore, this value needs to be accurately obtained [58].

Ball-on-Ring Compression

An alternative to the ring-on-ring test which incorporates some of the advantages of the ball-on-three-balls test is the Ball-on-Ring (BoR) test. This test uses a supporting ring and a loading ball instead of a loading ring, see Figure 2.11c. It was first introduced by Shetty et al. as an alternative to the support problems of the RoR method [53, 59]. For the BoR test, samples can also be less plane-parallel. Although the ball-on-ring test is non-standardised, research has been performed in order to validate the testing method [60, 61]. The results showed that the BoR test can be applied accurately to estimate the biaxial strength.

3

Materials and Methods

This chapter covers the different materials and methods used through the experiments of this thesis. First, additional information on the selected Martian regolith simulant is presented in Section 3.1. Next, the reasoning behind the different additive materials is discussed in Section 3.2, Section 3.3 covers material preparation. Section 3.4 covers the different characterisation techniques used and the SPS sintering methodology is covered in Section 3.5. The post-sintering steps, the mechanical testing method and the mechanical behaviour are covered in Section 3.6 through Section 3.8 respectively.

3.1. MGS-1 Martian Regolith Simulant

Martian Global Simulant - 1 (MGS-1) was chosen as the Martian regolith simulant for this thesis based on a previously performed trade-off. MGS-1 is supplied by Exolith Lab and is described as a ”global” basaltic soil simulant based on the mineralogy of Rocknest windblown soil as measured by the MSL Curiosity rover. An image of MGS-1 material can be seen in Figure 3.1.

Figure 3.1: *Image of MGS-1 Martian regolith simulant [62]*

Table 3.1: *MGS-1 powder physical characteristics*

Characteristic	Value	Unit
Uncompressed Bulk Density	1.29	$g\,cm^{-3}$
Mean Particle Size	90	µm
Median Particle Size	60	µm
Particle Size Range	>0.04 - 600	µm

Additional characteristics, mineralogy and bulk chemistry information for this stimulant, obtained from the specs sheet of Exolith Lab, can be found in Table 3.1, Table 3.2 and Table 3.3 respectively [62]. Note that the MGS-1 bulk chemistry information presented here supersedes that supplied by Cannon et al. from Subsection 2.2.3.

Table 3.2: *MGS-1 mineralogy (as mixed) [62]*

Component	Wt%
Anorthosite	27.1
Glass-rich basalt	22.9
Pyroxene	20.3
Olivine	13.7
Mg-sulphate	4.00
Ferrihydrite	3.50
Hydrated silica	3.00
Magnetite	1.90
Anhydrite	1.70
Fe-carbonate	1.40
Hematite	0.50
Total	100

Table 3.3: *MGS-1 bulk chemistry as measured by XRF [62]*

Oxide	Wt%
SiO_2	42.9
Al_2O_3	12.8
CaO	7.4
FeO	11.2
MgO	14.6
Na_2O	1.5
TiO_2	0.6
K_2O	0.6
P_2O_5	0.1
MnO	0.1
LOI	5.3
Total†	97.1

† Excluding volatiles and trace elements

3.2. Additive Materials

In this section the reasoning behind and the properties of the different additive materials are discussed. First the use and properties of aluminium powder is mentioned, followed by the discussion on bismuth oxide. Other additives have been considered, but not investigated. Examples of these include polymers, which were not investigated due to thermal instability at sintering temperatures, and silver hard solder, which could provide favourable brazing and wetting behaviour, but contained cobalt which would have produced toxic fumes upon sintering and was therefore not used.

Aluminium powder

Aluminium was chosen as an additive because of the future possibility to obtain the raw material from the Martian regolith [63]. This would mean the aluminium used as an additive in the sintering process could become a renewable resource and would only need to be imported from Earth in the initial stages of settlement. This makes it very attractive when looking from a sustainability perspective.

Al 99.8 powder was obtained from TLS Technik GmbH & Co. in the form of spherical particles, approximately 45 µm in size. Table 3.4 lists the material properties used for this material. During the experiment, the material was constantly stored and handled inside the controlled atmosphere of the glove box in order to minimise oxidation, see Subsection 3.3.2.

Bismuth oxide powder

Bismuth oxide was mainly chosen as an additive because of its low melting point of 817 °C, good wettability/flowability and chemical composition. As the material is already oxidised, it potentially mitigates an oxidation issue with aluminium as alumina has a melting temperature outside the SPS temperature range.

Bismuth(III) oxide powder, typically 99% pure, was obtained from Alfa Aesar[1] as a sieved powder of a US325 sieve size (44 µm). Material properties are listed in Table 3.4.

Table 3.4: *Density and melting temperature of additive materials*

	Aluminium	Bismuth oxide	
Property	**Value**	**Value**	**Unit**
Density	2.7	8.9	$g\,cm^{-3}$
Melting temperature	668	817	°C

3.3. Material Preparation

In this section the different material preparation steps are discussed. Two main preparation steps can be distinguished: sieving and mixing.

3.3.1. Sieving

MGS-1 is a very heterogeneous mixture of materials in different particle sizes and shapes. It was explained that this particle morphology can greatly influence the properties of the sintered sample. Therefore, it is important to control these parameters such that a better comparison between samples can be made. Sieving can be used to control the particle size.

Two different sieve sizes of 56 and 150 micron from Fisher Scientific[2] were used in order to sieve the MGS-1 powder. A predefined weight of raw powder was placed at the top of the sieving stack, which was then placed in a Haver EML 315 Digital Plus sieving machine[3]. Next, the material was sieved for 10 minutes on magnitude 10. After 10 minutes, the sieve stack was removed from the machine and the sieved powders were extracted. The sieved powders were weighed again in order to calculate the relative fractions. The fraction of material in the intermediate category (56 µm to 150 µm) was used to sinter samples with better control of the particle size.

[1] See Alfa Aesar CAS 1304-76-3 catalogue entry, last accessed 20-04-2022 (link)
[2] See Fisher Scientific product pages for 56 µm sieves (link) and 150 µm sieves (link). Last accessed 20-04-2022
[3] See Haver Boucker 315 Digital Plus booklet (PDF download), last accessed 20-04-2022 (link)

3.3.2. Mixing

In order to investigate the effect of aluminium and bismuth oxide on the sintering characteristics of MGS-1, these additives needed to be mixed in with the MGS-1 powder. Since pure aluminium is reactive and prone to oxidation, mixing of aluminium needed to take place in a controlled, low partial oxygen pressure environment. This environment was available in the MBraun Labstar glove box[4].

To further minimise the chance of oxidation, all mixing steps were performed within the glove box for both aluminium and bismuth oxide enriched powders. Raw powders were inserted into the glove box. The powders were weighed for mixing and combined into glass jars. Zirconia mixing balls were added in order to simulate powder dispersion. Mixing was performed on an Assistant/Cat RM 5F[5] machine for at least two days at 40 rotations per minute (rpm) in order to ensure proper mixing. The rotation speed was kept low in order to minimise any milling effects during powder mixing.

3.4. Characterisation Techniques

This section covers the characterisation techniques used to characterise the MGS-1 Martian regolith simulant powder as well as sintered samples. First, Scanning Electron Microscopy (SEM) and Energy Dispersive X-ray Spectroscopy (EDS) are covered, followed by the explanation of the particle size distribution measurements. Next, a combination method of Thermogravimetric Analysis (TGA) and Dynamic Mechanical Analysis (DMA) testing called Thermogravimetric Dynamic Mechanical Analysis (TGDMA) is explained followed by an explanation of X-ray Diffraction (XRD).

3.4.1. Scanning Electron Microscopy

It is important to know the morphology of both the MGS-1 powder and the sintered samples. Interesting morphology aspects of the powder includes the particle size and particle shape. For sintered samples, fracture surfaces and grain boundaries are areas of interest. Scanning Electron Microscopy is used to investigate these elements. In this thesis, a JEOLJSM7000F scanning electron microscope is used.

Since the particle size and shape have a significant effect on the sintering characteristics (see Subsection 2.3.2), it is important to quantify these parameters for the MGS-1 powder. Powder samples are prepared by gluing a small amount of powder to a sample holder using a conductive graphite adhesive paper. Excessive powder is shaken off the sample holder in order to decrease the chance of main chamber contamination.

Next, the samples are sputtered with a 15 nm gold coating in order to make the samples conductive. After sputtering the samples are stored in a container in order to avoid environmental contamination. In order to observe the sample, the sample is taken out of the container and loaded onto the sample holder of the SEM. Observation of the sample is performed in the main vacuum chamber of the SEM under a vacuum of at least 1×10^{-3} bar. Since MGS-1 is a ceramic powder, high accelerating voltages (up to 15 kV) and probe currents (up to 10 µA) can be used. Similar to powder samples, sintered samples are sputtered in order to make them conductive. Sintered samples are observed under higher magnifications in order to investigate the areas of interest.

3.4.2. Energy Dispersive X-ray Spectroscopy

It is also important to know the chemical composition of the MGS-1 regolith simulant both before and after sintering. This can be investigated using the Oxford Instruments' Ultim Max Energy Dispersive X-ray Spectroscopy (EDS) detector[6] which is integrated into the JEOL scanning electron microscope.

Using the EDS technique, the chemical composition of MGS-1 powder/sintered samples can be determined for an entire area (mapping) or for specific points (point analysis). EDS mapping is used to determine the elemental ratios of MGS-1 powder, which is used to validate manufacturing specifications as well as show any chemical changes that might have occurred during sintering. Point analysis is used to prove the chemical composition of additive materials or to characterise interesting areas in more detail.

[4] See the MBraun Labstar product page, last accessed 20-04-2022 (link)
[5] See the Cat Ing. RM 5F product page, last accessed 20-04-2022 (link)
[6] See the Ultim Max product page, last accessed 20-04-2022 (link)

In order to compare the data generated using EDS to literature data that is often specified in oxide percentages, a conversion needs to be made. In order to do this, a unit volume of mass is assumed and oxide wt% compositions are transformed into molar amounts. Next, these molar amounts are summed per atom type and converted back into a mass percentage. Finally, depending on the observed elements in EDS, the relative compositions are computed.

3.4.3. Particle Shape Analysis

Low magnification images are taken and used to measure particle sizes as well as determine asses particle shapes. Image processing using ImageJ via thresholding is applied to assess particle shape by determining the circularity, aspect ratio and roundness of fitted ellipses around particles. Manual particle tracing has been applied to aid the thresholding. A schematic overview of this process can be seen in Figure 3.2.

(a) *Original SEM image* **(b)** *Manually traced particles* **(c)** *Analysed particles with ellipses*

Figure 3.2: *Steps in the particle shape analysis process*

Circularity is a measure of the deviation between a circle and the particle's shape. A value of 1 indicated a perfect circle, and a value approaching 0 indicates an increasingly elongated shape. The circularity is calculated using the particle's area and perimeter using Equation 3.1. The aspect ratio of a particle is taken as the ratio of the major and minor axis of the fitted ellipse to the particle. The roundness of a particle is generally defined as the ratio of the average radius of circles fitted to particle corners and the maximum inscribed circle of the projected particle outline. In image processing software, the roundness is often calculated using the particle area and the major axis of the fitted ellipse, Equation 3.2.

$$circ. = 4\pi \frac{< Area >}{< Perimeter >^2} \tag{3.1}$$

$$round = 4 \frac{< Area >}{\pi < Major\ axis >^2} \tag{3.2}$$

It is important to note that all these particle metrics are based on projections of 3D particles into a 2D shape. Therefore, by definition, these metrics are subjective. However, visual characterisation based on reference projections can aid in determining the proper category of the particles. Such a visual aid is shown in Figure 3.3.

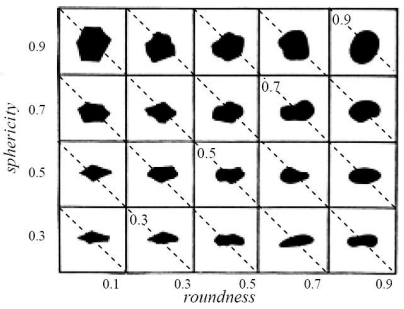

(a) *Sphericity and roundness values for different particles, adapted from [64, 65]*

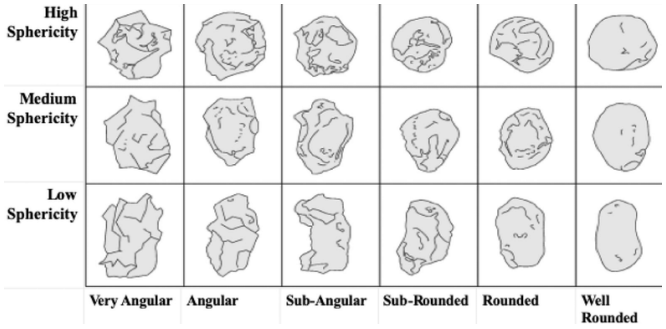

(b) *Sphericity and roundness descriptions for different particles, adapted from [66]*

Figure 3.3: *Charts of roundness vs sphericity for particle shape characterisation, adapted from [64–66]*

3.4.4. Particle Size Distribution Measurements

Particle Size Distribution (PSD) measurements are taken for three main reasons. The first is to investigate the particle size distribution of the received MGS-1 simulant and compare this to the observed particle size distribution on Mars. This comparison can be used (in part) to assess the fitness of MGS-1 simulant. The second is to investigate the effect of mixing on the particle size distribution. The goal of this investigating is to ensure no changes have occurred during mixing. Finally, PSD measurements can be used to check the sieving effectiveness.

All particle size measurements are performed using a Mastersizer 3000 machine from Malvern Panalytical[7]. Measurements are performed using two different sample dispersion methods: dry and wet. Dry powder dispersion uses large amounts of sample (>10 g per test) and can only be measured once. Wet powder dispersion uses small amounts of sample (approx. 1 g per test) suspended in a carrier liquid. The carrier liquid passes the detector in a closed loop, allowing the sample to be re-measured several times. However, it is harder to measure large particle sizes using wet dispersion due to fast sedimentation. Therefore, dry powder measurements were performed on bulk powders and wet measurements were performed on mixed and sieved powders.

For dry measurements the *Aero S* dry powder disperser was used. The appropriate amounts of powder was weighed and placed inside the disperser. The first sample was used to calibrate disperser settings, with measurements being performed for subsequent samples only when the obscurance was in the set range.

For wet measurements the *Hydro sm* wet disperser was used. Appropriate amount of powder were weighted and put in a beaker together with distilled water and ordinary dish soap (to act as a surfactant). Next, the mixture was sonically agitated in order to create a suspension. The *Hydro sm* disperser was filled with distilled water and the pump started. Using a pipette, a small amount of the suspension was added to the distilled water until the obscurance level fell within the set range again and the measurement was started. The disperser is cleaned using distilled water in between measurements of different samples.

3.4.5. Thermogravimetric Dynamic Mechanical Analysis

Thermogravimetric Dynamic Mechanical Analysis was used to determine the material behaviour of MGS-1 with increasing temperature. This experiment provides insight in the melting behaviour of MGS-1, which serves as an upper bound for the sintering temperature. TGDMA test were performed using a Setaram Setsys Evolution machine[8].

Alumina crucibles are used for the TGDMA measurements. First, the initial weight of the alumina crucible is measured. Next, powder is placed in the crucible and compacted using a compaction tool until half the crucible is filled. Again, the mass of the sample is recorded and put in the measurement software. The crucible is placed in the TGDMA machine and the measurement is started. All measurements are performed in an Argon atmosphere at a heating rate of 10 °C min^{-1} up to a temperature of 1400 °C. A 10 min hold at 200 °C is included to remove all moisture before continuing with the rest of

[7] See the Mastersizer 3000 product page, last accessed 20-04-2022 (link)
[8] See information supplied by the Materials Growth & Measurement Laboratory, last accessed 20-04-2022 (link)

the measurements. The heating and cooling cycle are symmetric in time and the heat flow as well as the mass loss is recorded during the entire measurement time.

3.4.6. Specific heat capacity determination

The specific heat capacity (c_p) of a material is the amount of energy required to heat or cool a unit mass of 1 kg of a material system by 1 degree Kelvin. In SI units it is expressed in terms of J/kgK or equivalently as J/kg°C. The energy required to heat a material to a given temperature T is given by:

$$E = m \cdot c_p \cdot (T - T_0) = m \cdot c_p \cdot \Delta T \tag{3.3}$$

where m is the mass of the material, c_p is the specific heat capacity, T is the desired temperature and T_0 the initial temperature of the material.

The c_p can be calculated by comparing heat flow data obtained from a Differential Scanning Calorimetry (DSC) test of the unknown material with heat flow data obtained from a known reference sample with known c_p values. The heat flow experiments are performed using a TA Instruments DSC250 machine[9]. To perform the experiment, a small amount of powder (5 mg to 10 mg) is weighed and placed in an aluminium sample pan. A lid, with a hole in it, is then placed on the pan to allow gasses to escape during the experiment. A synthetic sapphire reference sample is used for all measurements. In order to mitigate the effect of the machine, an empty pan is also measured to obtain a baseline curve.

All experiments are performed using a constant heating rate of 20 °C min^{-1} up to a temperature of 550 °C. An isothermal hold at 200 °C for 10 min is incorporated in each measurement to evaporate most of the moisture.

3.4.7. X-ray Powder Diffraction

Due to the high heterogeneity of the MGS-1 material and the lack of exact compounds in the powder it is very hard to use X-ray Diffraction (XRD) on MGS-1 powder for phase identification. However, XRD can be used to investigate the effect of sintering by looking at the spectra created by unsintered and sintered materials. Differences in peak location, height and width might provide useful information on the effect of sintering on the material composition.

All XRD measurements are performed using a Rigaku MiniFlex 600 XRD machine[10]. Sintered samples are first ground to a powder using a mortar and pestle. Powdered samples are flattened, placed in the XRD machine and exposed to Cu-alpha radiation over an angular range between 10° and 80°. The step size is 0.02° with a movement speed of 0.5 ° min^{-1}.

3.5. SPS Sintering Methodology

To make sure the experiments are performed in a reproducible manner, it is important to know the sintering methodology used to produce all of the sintered samples. This methodology is explained in this section. First, the sample preparations steps for sintering are discussed followed by an explanation of the used sintering cycles with their relevant parameters. All samples are made using a FCT Systeme Gmbh SPS machine.

Spark Plasma Sintering Sample Preparation

In order to prepare a sample for sintering, an assembly needs to be made that can be inserted into the SPS machine. This assembly consists of several parts: a sample mould, two punches and two adaptors. In order to isolate and protect the sinter assembly components from the to be sintered material, graphite paper is used. During sintering, a graphite sleeve was used to isolate the assembly and protect the pressure vessel. Figures 3.4a to 3.4c show the sample mould and punches, sample assembly including adaptors and assembly including graphite sleeve respectively. Finally, Figure 3.4d shows a graphical representation of the sintering assembly.

In order to make the assembly, the graphite paper is lined on the inside of the mould using one of the punches. Next, the punch is partially slid out of the mould and a circular protective piece of graphite paper is used to cover the punch. Next, the to be sintered material is loaded into the mould

[9] See the TA Instruments DSC250 product page, last accessed 20-04-2022 (link)
[10] See the Rigaku MiniFlex product page, last accessed 20-04-2022 (link)

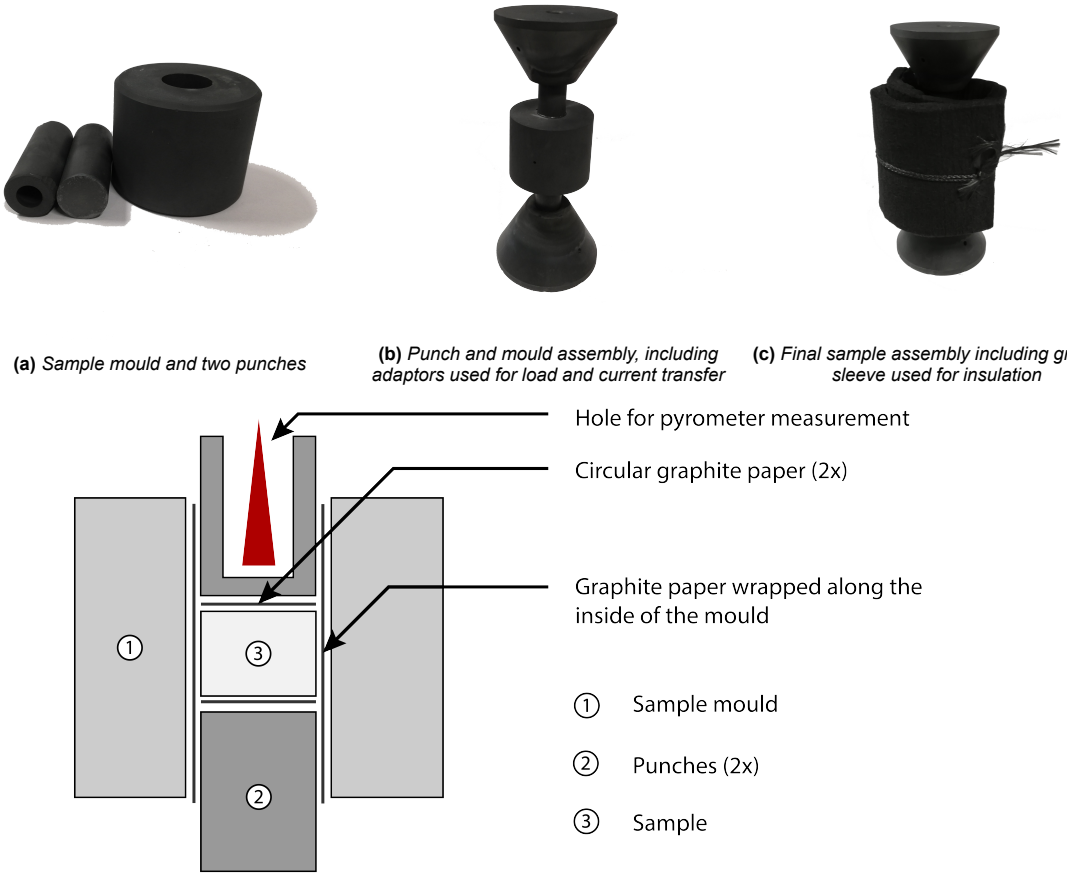

(a) *Sample mould and two punches*

(b) *Punch and mould assembly, including adaptors used for load and current transfer*

(c) *Final sample assembly including graphite sleeve used for insulation*

(d) *Graphical representation of the punch and mould assembly, with graphite paper indicated*

Figure 3.4: *Components and schematic representation of the sample assembly used during sintering*

and covered by a second piece of protective graphite paper. The second punch is inserted and the assembly is pre-compressed to a force of one metric tonne of force using a hydraulic press.

After pre-compression, the mould-and-punch assembly is transferred to the SPS machine. All tests were performed with an insulating graphite sleeve surrounding the assembly. The second adaptor is placed on top of the assembly and the vessel of the SPS machine is closed. Next, the initial force of 5kN is applied after which the sintering process is started.

For mixed powders, the SPS mould assembly was made in the glove box in order to minimise the possibility for oxidation to occur. Only when the SPS machine was ready, the punch-and-mould assembly was taken out of the glove box, transferred to the hydraulic press, compressed, sleeved and moved as quickly as possible into the SPS machine.

SPS Cycle Settings

This subsection will cover the different SPS machine settings used during sintering. First, the general sintering conditions are covered, followed by an explanation of the used temperature profiles, pressure profiles and the dwell cycles.

Sintering Conditions

In the ideal case the sintering conditions resemble the conditions found on Mars. This includes a low-pressure environment, mostly consisting of a relatively CO_2 rich atmosphere. Unfortunately, this was not possible in the SPS machine. Therefore, all sintering experiments were performed in vacuum.

The vacuum conditions were achieved using a series of so-called pump and flush cycles. First the pump was turned on to create the vacuum, after which the chamber was flushed with Argon processing

gas. Flushing also introduced an inert environment, minimising the chance of oxidation.

SPS Machine Settings
A multitude of settings can be adjusted during the SPS process, from the temperature and pressure to the pulse duration in between pulses. For the experiments in this thesis, most of these settings were kept constant and only parameters of interest were changed. These parameters include sintering temperature, pressure and ramp down. A discussion for each parameter is presented below. During sintering the dwell cycle was kept constant at a 10 min temperature and pressure hold.

Temperature Settings For the experiments in this thesis the sintering temperatures were varied between 700 °C and 1060 °C. This range was chosen since it encompasses both the melting temperatures of aluminium and bismuth oxide, which is necessary to ensure a liquid phase during sintering.

Heating to the desired dwell temperature occurred using a constant heating rate of 50 °C min^{-1} for all samples. This heating rate determines the time required to reach dwell cycle conditions.

Pressure Settings The effect of consolidation on sintering can be investigated by varying the applied pressure. For these experiments, two different pressures were used: approximately 30 MPa and 50 MPa, corresponding to an applied force of 10 kN and 16 kN respectively. The maximum pressure was determined by the graphite die diameter used for the experiments. Reaching this pressure was performed during the heating stage, hence ramp up speed was variable and dependent on the time required to reach the dwell temperature.

Ramp down Ramp down refers to the segment in the SPS cycle where the temperature and or pressure are decreased. Decreasing these parameters can occur simultaneously or sequentially. In this thesis, two different sequential ramp down segments have been investigated. In the first configuration, first the pressure decreased in 5 min while the temperature stayed constant. Next, the temperature also decreased in 5 min. In the second configuration, the pressure was maintained after the hold and the temperature was decreased. After the temperature decrease, the pressure was released.

Overview of Used Sintering Settings

Throughout all the sintering steps, several of the SPS machine settings were kept constant. These settings can be found in Table 3.5. Variable settings are summarised in the overview table (Table 3.6) below. The reader is referred to Table A.1 for the exact specific sintering settings of each sintered sample. Recall that all experiments are performed under vacuum.

Table 3.5: *Constant SPS machine settings used during sintering*

Setting	Value	Unit
Pulse time	15	ms
Pause time	5	ms
Heating rate	50	°C min^{-1}

Table 3.6: *Overview of variable SPS sintering settings*

Materials	Types used	Sintering force	Sintering Temp.	Dwell cycle
As received (baseline) MGS-1	as received sieved 56-150 µm sieved <56 µm sieved ext.	10 kN (30 MPa) 16 kN (50 MPa)	700 °C 800 °C 900 °C 950 °C 1000 °C 1050 °C 1060 °C	*Standard:* 10 min pressure hold and 15 min temperature hold *Reversed:* 15 min pressure hold and 10 min temperature hold
MGS-1 + Al	2.5wt% additive 5 wt% additive			
MGS-1 + Bi_2O_3				

Overview of A Typical Sintering Cycle

In Figure 3.5 below an overview of a typical sintering cycle is shown. In this case, a dwell temperature and pressure of 1050 °C and 50 MPa respectively were used, with a 15 min temperature hold and 10 min pressure hold. The pump-and-flush, ramp up, dwell and ramp down stages of the SPS run are also indicated.

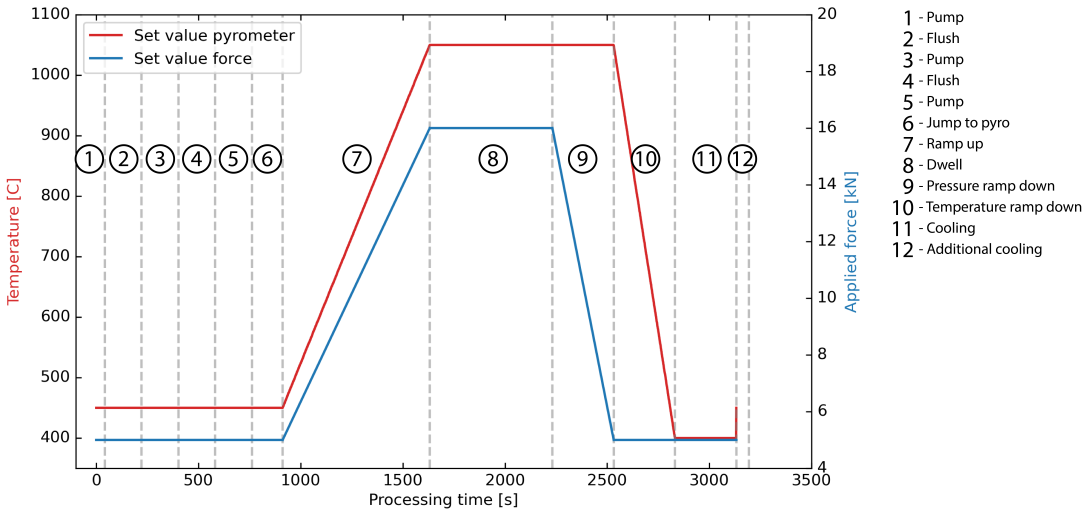

Figure 3.5: *Sintering profile including stage indications*

Sintering Onset and Saturation

A lot of data is collected during sintering. Using this data, valuable insight into the sintering characteristics of MGS-1 Martian regolith simulant can be obtained for both the baseline material as well as the enriched mixtures. Parameters that are of special interest are the moment sintering starts, the sintering onset, and when most of the sintering has occurred, hereafter referred to as sintering saturation.

The sintering onset and saturation are determined using the relative piston travel, temperature and pressure data collected during sintering. A schematic representation of the used data for these observations is presented in Figure 3.6. The onset time is defined as the intersection between the horizontal and the slope of the relative piston travel (green line in Figure 3.6). The onset time can also be used to determine the sintering onset temperature and pressure. The saturation time is determined from the relative piston travel curve. When the curve plateaus in the temperature and pressure hold, sintering saturation occurs. The onset of this plateau is taken as the saturation time.

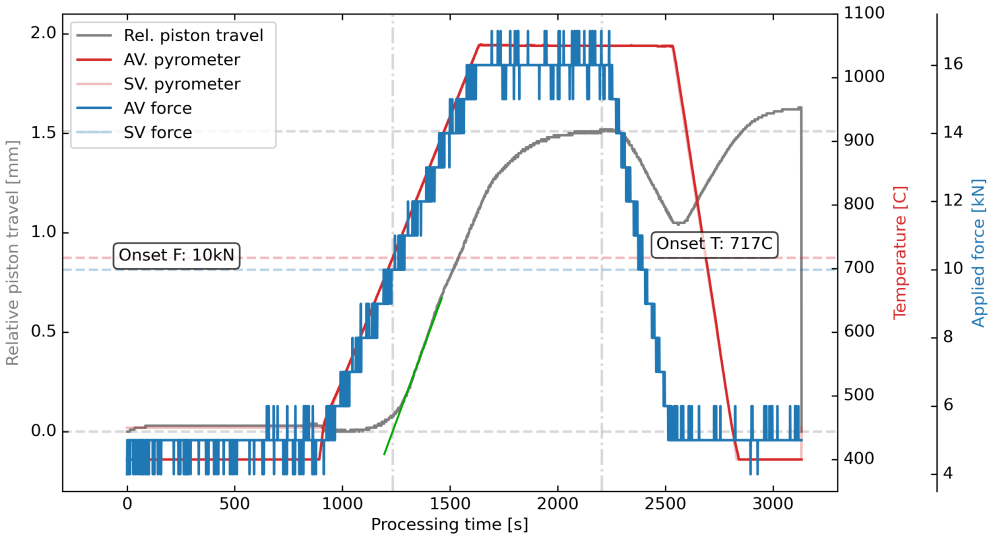

Figure 3.6: *Schematic representation of the data used to determine the sintering onset and saturation. Set values (SV) and actual values (AV) are indicated.*

3.6. Post Sintering Steps

This section covers the sample preparation for mechanical testing and the determination of the geometric density of the sintered samples.

Sample Preparation for Mechanical Testing

Prior to mechanical testing, all samples were processed to obtain the desired shape and surface finish. Samples were prepared by grinding using progressively finer abrasive disks until a preferred final finish of 4000 SiC grit was obtained. Initial grinding was aimed at removing the fuse graphite paper from the sample, hence grinding times varied. For final finish grinding, each sample was grounded for at least one minute. All samples were dry ground because poorly sintered samples proved prone to damage when wet ground. Grinding also removed the fused graphite protective foil from samples sintered at high temperatures.

Geometric Density Determination

After sample preparation, the geometric density of the sample could be determined by measuring the diameter, thickness and weight of each sample. This method for density determination was chosen over others, such as the Archimedes method, due to susceptibility to damage due to fluids as mentioned above. This also ensured that the density determination did not affect the mechanical properties of the density tested samples.

The sample diameter and thickness were measured five times in order to provide a reliable average and get an estimate for the error introduced in the manual grinding step. All measurements were taken with a calliper and a micrometre. Generally, the calliper resulted in a higher sample volume and hence a lower density and relative density. This results in a conservative estimate for the properties.

3.7. Mechanical Testing: Ball-on-ring Method

Material properties of sintered samples are evaluated using mechanical testing, specifically using the ball-on-ring method. First, the method is introduced and the governing equations are presented. Next, the compression set-up for this thesis is discussed. The section is concluded by a discussion on the compression results processing steps.

3.7.1. Introduction, Theory and Governing Equations

The ball-on-ring method has been frequently applied to study the strength of brittle, thin, disk-shaped materials. This makes the ball-on-ring method especially suitable for samples produced via SPS. Con-

trary to conventional 3-point or 4-point bending tests that result in uniaxial properties, the BoR test characterises the biaxial strength of the material. Since this type of loading is more common in application, biaxial properties are preferred over uniaxial ones. Another advantage of this testing method over 3-point or 4-point bending tests is in its sensitivity to flaw orientation. The conventional methods are sensitive to both edge and surface flaws since both are in line with the main stress axis. In the BoR test, the highest stress occurs in the centre of the sample, avoiding edge effects. Therefore, the BoR test is only sensitive to surface flaws as only those follow the main stress axis. Additionally, the radially symmetric biaxial load in the BoR test signifies that defect orientation does not play a major role. A schematic of the ball-on-ring test is shown in Figure 3.7.

Closed form solutions exist for the maximum tensile stress of a specimen tested using the BoR method. One solution was developed by Kirstein and Woolley [67]. This solution was adapted for the BoR test by Shetty et al. in 1980 [59]. An alternative solution was proposed by Hu [68]. Both solutions are a function of the test setup geometry, the sample geometry and the maximum sustained load. For a uniform concentric load, the maximum stresses at the centre as presented by Kirstein and Woolley [67] are given by:

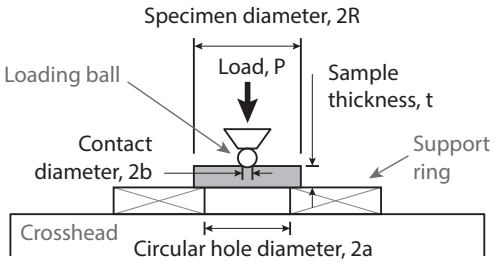

Figure 3.7: *Ball-on-ring test schematic*

$$\sigma_{\max} = \frac{3P(1+\nu)}{4\pi t^2}\left[1 + 2\ln\frac{a}{b} + \frac{1-\nu}{1+\nu}\left(1 - \frac{b^2}{2a^2}\right)\frac{a^2}{R^2}\right] \tag{3.4}$$

where a, b, R, P and t are defined as in Figure 3.7 and ν is the specimen Poisson's ratio.

However, the radius of contact area, b, is hard to determine. Shetty et al. and With and Wagemans offered a simple approximation given by $b = t/3$ [59, 69]. Additionally, this solution also fails to account of the effects of small loading areas. Westergaard wanted to address this issue by applying the "special theory of slabs" as opposed to the "ordinary theory". The special theory is much more complicated than the ordinary theory. An equivalent contact radius b_{eq} can be found that expresses the result of the special theory in terms of the ordinary theory. The expression proposed by Westergaard is given by [70]:

$$b_{eq} = \begin{cases} \sqrt{1.6b^2 + t^2} - 0.675t, & \text{for } b < 1.724t \\ b, & \text{for } b > 1.724t \end{cases} \tag{3.5}$$

An accurate value for the radius of uniform loading, b, is still required in this expression. Using Hertz contact theory, Equation 3.6, this value can be calculated.

$$z = \left[\frac{3P \cdot r}{4}\left(\frac{1-\nu_1^2}{E_1} + \frac{1-\nu_2^2}{E_2}\right)\right]^{1/3} \tag{3.6}$$

where r is the radius of the loading ball, ν is the Poisson's ratio, E the Young's modulus and subscripts 1 and 2 denote the specimen and loading ball respectively.

By substituting the expression for z in Equation 3.5, a new expression for b_{eq} is found:

$$b_{eq} = \begin{cases} \sqrt{1.6z^2 + t^2} - 0.675t, & \text{for } z < 1.724t \\ z, & \text{for } z > 1.724t \end{cases} \tag{3.7}$$

Finally, substituting Equation 3.7 in Equation 3.4 results in the expression for the biaxial strength that will be used throughout this thesis:

$$\sigma_{\max} = \frac{3P(1+\nu)}{4\pi t^2}\left[1 + 2\ln\frac{a}{b_{eq}} + \frac{1-\nu}{1+\nu}\left(1 - \frac{b_{eq}^2}{2a^2}\right)\frac{a^2}{R^2}\right] \tag{3.8}$$

In Equation 3.6, the specimen Young's modulus needs to be known. As a first approximation, another expression from Kirstein and Woolley can be used [71]. They developed expression Equation 3.9 for the deflection w of a similar shaped thin elastic disc specimen under central loading.

$$w = \left\{-0.0642 + 0.5687\left(1-\nu^2\right) + \left[-0.3793 + \left(1-\nu^2\right)\right] \cdot \frac{a}{R^2}\right\}\left(\frac{Pa^2}{Et^3}\right) \tag{3.9}$$

This expression can be rewritten in terms of the slope of the deflection curve, P/w, to result in an estimate for the Young's modulus:

$$E = \left\{-0.0642 + 0.5687(1-\nu^2) + [-0.3793 + (1-\nu^2)] \cdot \frac{a}{R^2}\right\} \cdot \left(\frac{P}{w}\frac{a^2}{t^3}\right) \tag{3.10}$$

3.7.2. Compression Test Set-up

Ball-on-ring compression tests were performed on a Zwick-Roell 10 kN compression bench. A static indentation fixture was used to apply the load. Since the ball-on-ring method is semi-standardised, multiple support ring-to-sample ratios can be found in literature. Values range between 0.542 [69] and 0.818 [61]. For this research, a value of 0.8 was chosen based on Shetty et al. [72]. This resulted in a support hole radius of 16 mm. To support the samples during testing, a stainless-steel ring was machined. A schematic overview of the ball-on-ring fixture is seen in Figure 3.8. The compression tests were performed at piston speeds of 0.5 mm min^{-1} to 1 mm min^{-1}, with most test being performed at a piston speed of 0.5 mm min^{-1}. Typical time to failure after first contact ranged between 14.82 s and 96.92 s for sintered samples.

The support ring was glued to the compression bench cross bar using double sided tape. Alignment of the indenter with the centre of the support ring was ensured by using a 3D printed guide. Similarly, sample alignment was ensured by the use of other 3D printed guides. An overview of the support ring placement and sample alignment is shown in Figure 3.9.

The material of the indenter ball is assumed to be stainless steel. All relevant indenter parameters for the equations above are listed in Table 3.7.

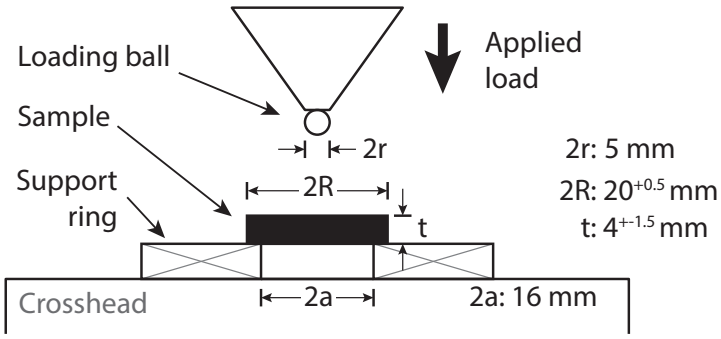

Figure 3.8: *Schematic overview of ball-on-ring testing fixture*

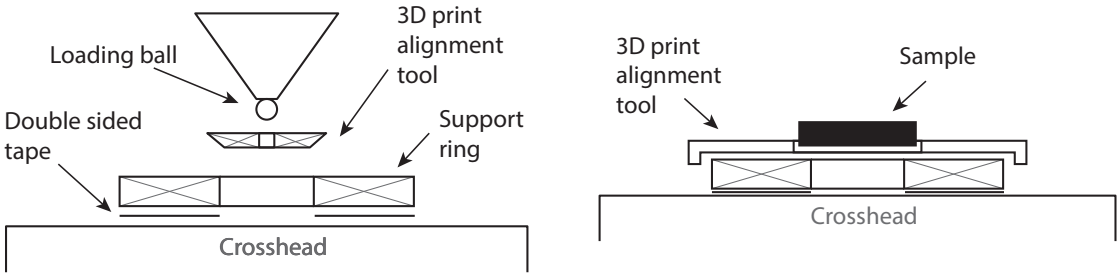

(a) *Schematic of support ring alignment*

(b) *Schematic of sample alignment*

Figure 3.9: *Schematic overview of a) support ring placement and b) sample alignment*

Table 3.7: *Indenter ball properties used in strength calculations*

Property	Value	Unit
Radius	2.5	mm
Young's modulus	198000	MPa
Poisson's ratio	0.275	-

3.7.3. Results Processing

After the compression tests have been performed, the data needs to be processed in order to get to the final results. First, the data needs to be corrected in order to take into account the deflection of the compression bench via a bench compliance measurement. Next, the final results are obtained by using Equations (3.6) to (3.10). A value of 0.2 has been assumed for the Poisson's ratio of sintered MGS-1 samples. In order to do this properly, samples need to be evaluated in a certain stress range in order to improve specimen comparison.

Bench Compliance and Data Correction

Prior to each compression test run, a bench compliance test was performed in order to estimate the bench deflection upon loading. Instead of a sample, a metal disc was used during these experiments. The sample data can be corrected by subtracting the bench deflection data. This procedure is explained below.

First, the bench compliance test is performed up to the maximum capacity of the used load cell. After each bench compliance test, a spherical indentation was left in the metal plate. The diameter of this indentation was measured using optical microscopy on a Keyence WideArea 3D Measurement System Controller, VR5000. Second, using Equation 3.11, this diameter was transformed to a hole depth. In the third step, this hole depth was subtracted from the maximum deflection of the compression bench and a new bench deflection curve was estimated via a linear approximation.

$$d = 2\sqrt{h(D-h)} \tag{3.11}$$

where d is the indentation diameter, h the indentation height and D the diameter of the indenter.

To correct the specimen deflection data, the bench deflection for each load was calculated and subsequently subtracted from the specimen deflection data to obtain a more accurate result. This procedure is illustrated in Figure 3.10. Note that the correction does not affect the maximum force sustained by each sample, but only the slope of the force-deflection curve.

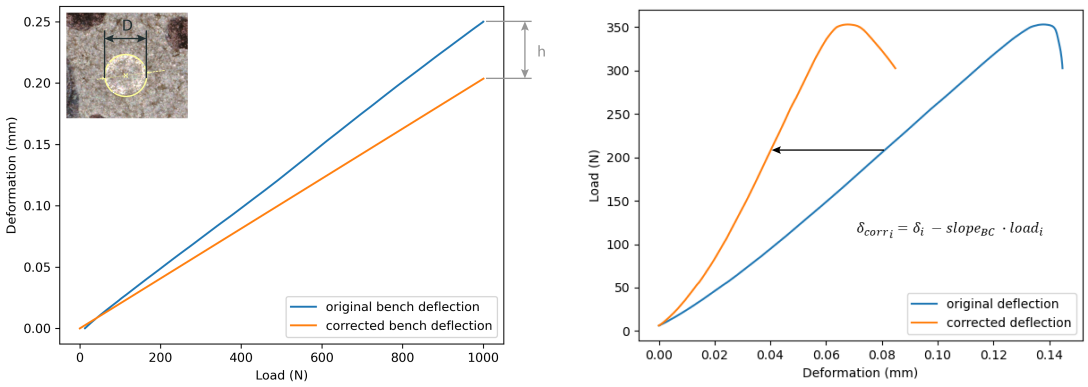

(a) *Determination of the bench deflection curve*

(b) *Correcting the specimen deflection data*

Figure 3.10: *Specimen deflection data correction by using the bench deflection measurement*

Stress Range Correction

The Young's modulus of a sample is approximated using the linear region in the deflection curve. To improve the comparison between samples, it is important to evaluate the Young's modulus within an equal stress range. This correction process starts with an initial approximation of the Young's modulus

obtained via visual inspection of the linear region. Next, the biaxial strength of all samples is calculated. Samples with a biaxial strength above a certain threshold are subsequently selected. The weakest sample in the selection is used to determine the stress range. The upper and lower limits are set at 20 and 80 percent of the minimal biaxial strength.

Next, for all samples in the selection, these upper and lower limits of the biaxial stress are used to calculate the corresponding forces in each sample using Equation 3.12 obtained from rewriting Equation 3.8. These forces are subsequently used in the deflection curves of each sample to define the linear region used to calculate the Young's modulus. Finally, the new Young's modulus is used to update the biaxial strength of all selected samples.

$$F = \sigma \cdot \frac{4\pi t^2}{3P(1+\nu)} \left[1 + 2\ln\frac{a}{b_{eq}} + \frac{1-\nu}{1+\nu}\left(1 - \frac{b_{eq}^2}{2a^2}\right)\frac{a^2}{R^2} \right]^{-1} \tag{3.12}$$

3.8. Mechanical Behaviour Determination

Another interesting aspect of the mechanical response of sintered samples is the mechanical behaviour. In this thesis, two different aspects are investigated. The first is an evaluation of the deformation behaviour and the second is and investigation of the fracture pattern.

Deformation Behaviour

The deformation behaviour of samples is evaluated using the deflection curve of the biaxial test. The sample behaviour after the maximum sustained load is used to categorise the sample as exhibiting either brittle or tough behaviour. To do this, the Area Under the Curve (AUC) after the maximum load is divided by the AUC before the maximum load. Using visual inspection of the deflection curves, a threshold value is chosen. If the area fraction of a sample is below the threshold, the sample is said to behave brittle. Otherwise, the sample behaves tough. The threshold value has been set to 0.252 for all behaviour determinations.

Fracture Pattern Analysis

Using optical microscopy, the radial fracture pattern of broken samples is observed. The number of fractures is recorded and patterns are evaluated to determine crack initiation and propagation. It is important to note that the fracture of ceramics is loading rate dependent. For low loading rates, a single crack is potentially enough to effectively release the applied stress. At higher loading rates, additional cracks can potentially nucleate and propagate during testing as the stress release of the initial crack has not yet become effective. In this thesis, the amount of fracture is used as an indicator for material homogeneity. For this analysis, few fractures (less than three) indicate a low amount of crack initiation points, possibly pointing to a less homogeneous material. Multiple fractures indicate more crack initiation points attributed to a more homogeneous stress distribution, indicating a more homogeneous material.

4

Powder Characterisation

Since material properties can have a large effect on sintered sample characteristics, it is important to have a good understanding of the base powder used during the analysis. To get this understanding, several characterisation methods from the previous chapter can be employed to determine the chemical and physical properties of the used materials. In this chapter, the results of in-house powder characterisation are shown. In Section 4.1 the bulk chemistry of as received MGS-1 regolith and mixed simulant with 5wt% additive is determined using EDS. Next, in Section 4.2, the physical properties of the as received regolith and that of the additive powders are assessed by looking at the particle shape, size and distribution. Finally, the thermal behaviour of MGS-1 is investigated in Subsection 3.4.2.

4.1. Bulk Chemistry of As-received MGS-1

In this section the bulk chemistry of as-received (baseline) regolith and mixed regolith is discussed. First, the comparison between MGS-1 and actual Martian regolith is presented, followed by the composition as measured via EDS.

Table 4.1 compares the bulk chemical composition of MGS-1 as reported by Exolith Lab, as measured using X-Ray Fluorescence Spectrometry (XRF), to the composition of Martian regolith for different locations on Mars. Note, the MGS-1 data has been normalised to 100% and volatiles as stated in the MGS-1 fact sheet have been included.

Table 4.1: *Bulk chemistry of MGS-1 as reported by Exolith Lab compared to Martian compositions of different locations*

Oxide	**MGS-1 (Exolith Lab) [%]**	**Rocknest [18] [%]**	**Difference Rocknest [%]**	**Gale Crater Average [16] [%]**	**Difference Gale Crater [%]**
SiO_2	43.6	43.02	1.357	43.16	1.034
Al_2O_3	13.0	9.38	32.758	9.16	34.742
CaO	7.5	7.27	3.455	7.08	6.057
FeO_T	11.4	19.2	50.887	19.33	51.734
MgO	14.8	8.7	52.396	8.6	53.250
Na_2O	1.5	2.7	55.373	2.72	56.315
TiO_2	0.6	1.19	69.894	1.05	53.026
K_2O	0.6	0.49	21.607	0.5	19.805
P_2O_5	0.1	0.95	166.074	0.92	160.201
MnO	0.1	0.42	122.054	0.42	122.054
Cr_2O_3				0.46	
Cl	0.005	0.69	176.734	0.77	197.377
SO_3	1.29	5.48	117.653	5.83	127.483
LOI	5.4				
Total	100			100	

From the table it becomes clear that the composition of MGS-1 is close to the material observed on Mars for the major constituent elements. However, some discrepancies exist, for example in the amount of titanium containing compounds. Additionally, the amount of sulphur containing compounds in MGS-1 is far lower than that found on Mars.

To validate the information provided by the manufacturer, in-house chemical analysis was performed using EDS during SEM. The six most abundant elements are considered and the elemental composition of MGS-1 is calculated from the oxide values reported above, using the method detailed in Subsection 3.4.2. The results are shown in Table 4.2.

Table 4.2: *Elemental composition of baseline MGS-1 calculated from EDS compared to calculated values from Exolith Lab and Gale Crater data*

Element	Measured Composition [%]	Calculated from Exolith Lab [%]	Calculated from Gale Crater [%]
O	52.5	44.995	47.020
Si	19.2	21.592	21.908
Fe	10.9	13.367	14.682
Al	7.3	8.059	5.265
Ca	5.1	7.304	5.495
Mg	5.1	4.683	5.631

Comparing the values, it is logical that oxygen is the most present element due to the many oxides present in MGS-1 minerals. The other observed values are in the same order of magnitude as the calculated values, mostly differing a couple of percent. Hence, they are in line with expectations and comparable. However, deficiencies in the amount of iron and to a lesser extent aluminium are present.

4.2. Particle Size, Shape and Distributions

In this section, the physical properties of MGS-1 are compared to observations for actual Martian material. Three different areas will be investigated. These are the particle shape, size and particle size distribution respectively. Finally, the particle size and shape of the additive materials is also presented.

Particle Size of As Received MGS-1

There are several ways to investigate the particle size of a powder. In this thesis, three different methods were used. In the first method, the particle size was investigated by a dry sieving test that determines the relative weight percentages of several sieve sizes. The second method investigates images of the sieved powders using SEM and finally the particle size can be assessed by looking at the results from the particle size distributions. The latter results regarding particle size are covered in the subsection on the PSD.

In the first method, two different sieve sizes of 56 µm and 150 µm respectively are used. Three different batches were sieved, the results of which can be found in Table 4.3. The amount of sieved material totalled almost 400 g, which is expected to result in a good representation of the overall powder.

Table 4.3: *Weight and percentage of sieving fraction*

	Sieve size	Fraction <56 µm	Fraction 56 - 150 µm	Fraction >150 µm	Total
Batch 1	mass [g]	20.14	39.10	39.31	98.55
	[%]	20.44	39.87	39.89	100
Batch 2	mass [g]	17.05	40.48	41.56	99.09
	[%]	17.21	40.85	41.94	100
Batch 3	mass [g]	37.30	76.28	86.92	200.5
	[%]	18.16	38.05	43.35	100
Average	[%]	18.75	39.52	41.73	100
STD	[%]	0.013225	0.014220	0.011509	

From the weights of the sieved powders, it is clear that the majority of the particles are of the intermediate and largest particle sizes. However, no information about the size of particles within these

sieving fractions can be obtained from this analysis. In order to get a first understanding of the individual size of particles, SEM imaging was used. Particle images using the SEM for the different sieve sizes can be seen in Figure 4.1.

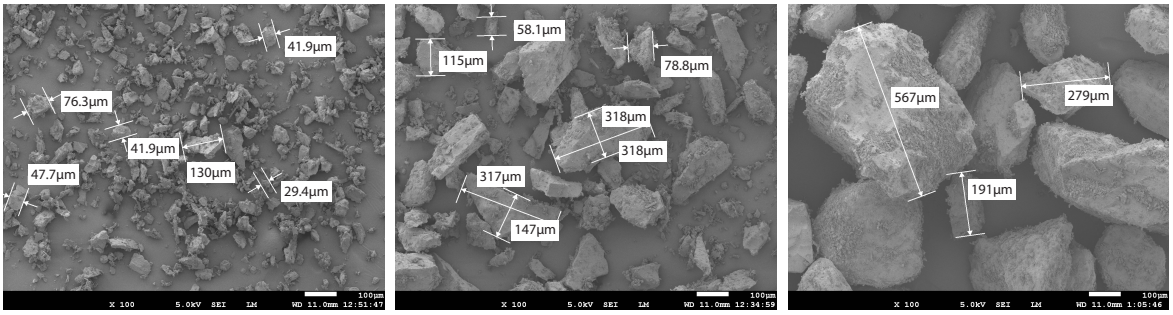

(a) *Particle sizes in the smallest sieving fraction*

(b) *Particle sizes in the medium sieving fraction*

(c) *Particle sizes in the largest sieving fraction*

Figure 4.1: *Particle sizes of MGS-1 powder as determined from EDS images*

It can be observed that the sieving process in general was successful in separating the different particle sizes, but some particles were incorrectly separated. For example, small particles in Figure 4.1b indicate that not all particles smaller than 56 µm have been sieved out.

Additionally, particles with dimensions larger than the sieving size can be observed (for example the particle in the lower left-hand side of Figure 4.1b). The presence of these particles can be explained by looking at their particle shape and other dimensions.

Particle Shape of As Received MGS-1

From the SEM images, it can be seen that the particle shape of MGS-1 regolith simulant is irregular. Particle shapes range from approximately round to highly elongated and from approximately spherical to plate-like. Larger particles are generally less regularly shaped than smaller particles. The presence of high aspect ratio particle explains the particles with one length dimensions that falls outside of the sieve sizes, as the other two fall within the sieve sizes.

Due to the irregular shape, it is harder for the particles to be closely packed together. This results in porosity in the MGS-1 powder. Additionally, smaller particles tend to agglomerate in larger groups, as can be seen in Figure 4.1b and Figure 4.1c. In between these agglomerates, voids are present. The combination of the difficulty in packing with the porosity in agglomerated particles makes it plausible that a liquid phase during sintering can infiltrate between these particles and fill up voids.

To get a better understanding of the particle size, particle size analysis is performed. First, SEM images are compared with the charts shown in Figure 3.3 using visual inspection. Next, image processing is performed to evaluate shape descriptors.

Comparing the particle shapes of the original SEM images with the charts shown in Figure 3.3, it is concluded that the smallest sieving fraction mostly contains angular to sub-angular particles. Sphericity is generally medium, but a large spread in particles is apparent. In the medium sieving fraction, the angularity is similar but more particles with high aspect ratios and lower sphericity are present. The largest particle size shows sub-angular to rounded particles. Sphericity is medium on average, but elongated particles are present.

The results for the image processing process for the three different sieving fractions are shown in Figure 4.2. Individual particles are coloured, numbered and fitted ellipses are shown. The particle circularity, aspect ratio and roundness are evaluated from the fitted ellipses. The results are summarised in Table 4.4.

The values obtained from image processing correspond to those presented in the sphericity and roundness charts, Figure 3.3a. The average obtained roundness value of 0.6266 falls between sections in the chart, but comparing particle shapes indicates that the value is appropriate for the observed particles.

To better understand the locality, spread and skewness obtained via image processing, box plots are drawn for each of the three shape descriptors. Whiskers are drawn to indicate the variability outside

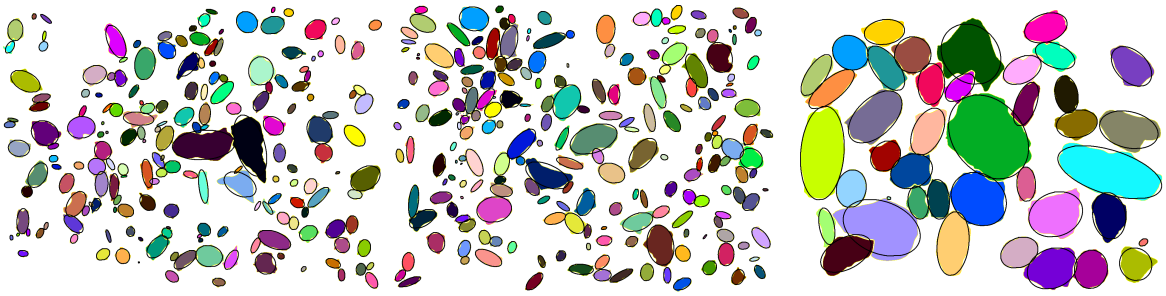

(a) *Particle shapes of the smallest sieving fraction* **(b)** *Particle shapes of the medium sieving fraction* **(c)** *Particle shapes of the largest sieving fraction*

Figure 4.2: *Analysed particle shapes from sieved MGS-1 powders*

Table 4.4: *Summarised results of particle shape descriptors*

Sieving fraction	n	Circ.	STD Circ.	AR	STD AR	Round	STD Round
<56 µm	186	0.7267	0.1084	1.7381	0.6012	0.6300	0.1698
56-150 µm	212	0.7043	0.0971	1.8266	0.6135	0.5998	0.1653
>150 µm	40	0.7261	0.0752	1.6318	0.4121	0.6501	0.1527
Average	–	0.7190	–	1.7321	–	0.6266	–
STD	–	0.0104	–	0.0797	–	0.0207	–

Note: n = number of analysed particles, Circ = circularity, AR = aspect ratio, Round = roundness, STD = standard deviation

the box. The results are shown in Figure 4.3.

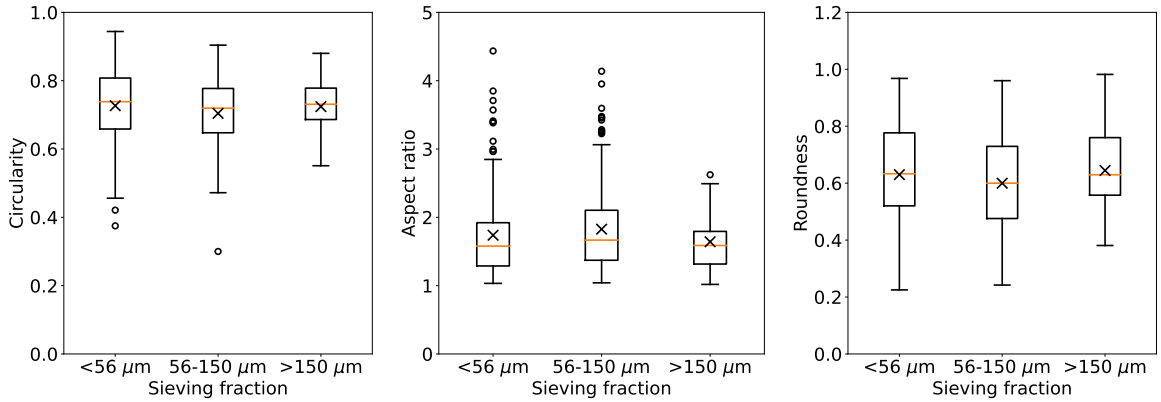

(a) *Circularity box plot of sieved material* **(b)** *Aspect ratio box plot of sieved material* **(c)** *Roundness box plot of sieved materials*

Figure 4.3: *Box plots of shape descriptors for a) circularity, b) aspect ratio and c) roundness. Mean values are indicated by "x".*

Whiskers are drawn at 1.5 times the interquartile range. Only few outliers exist within this range for the circularity. All data from the roundness determination fall within this range. However, large outliers are present in the aspect ratio, indicating the presence of highly elongated particles.

PSD of As Received MGS-1

The particle shape distribution affects particle packing and by extension sintering properties. The particle shape distribution for Martian regolith is known (Table 2.2.2), hence ensuring a similar particle size distribution is important for any simulant. To assess the particle size distribution of MGS-1, six different measurements were performed. The average particle size distribution has also been computed,

Figure 4.4.

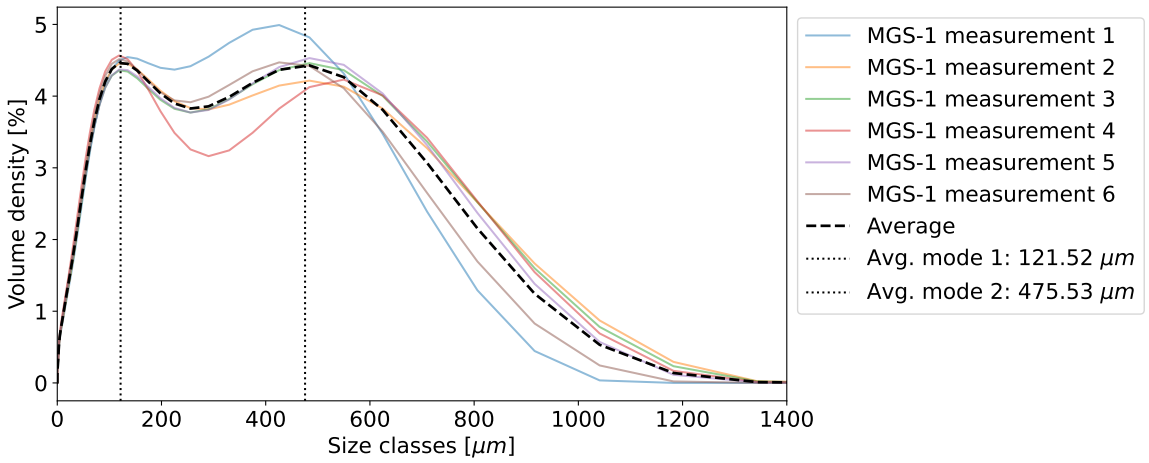

Figure 4.4: *Particle size distribution of as received MGS-1*

The obtained distribution is bimodal, with the modes at approximately 120 µm and 475 µm respectively. Additionally, the measurements show that particles larger than the specified 600 µm by the manufacturer are observed. This is explained, in part, by similar observations from particle sieving, where particles with one dimension larger than the used sieve size passed through the sieves.

Particle Size and Shape of Additive materials

It is important to investigate the particle size and shape of the additive materials, as these properties affect the particle packing and additive distribution within the mixed powder. This is especially important as the dispersion of a potential liquid phase can have a large effect on sample properties, and hence the effectiveness of the additive. To this extent, Scanning Electron Microscopy is used. SEM images of the used aluminium and bismuth oxide powder are shown in Figure 4.5. The aluminium particles are mostly spherical, as per manufacturing specifications. The bismuth oxide powder is irregular and contains a large number of very small particles.

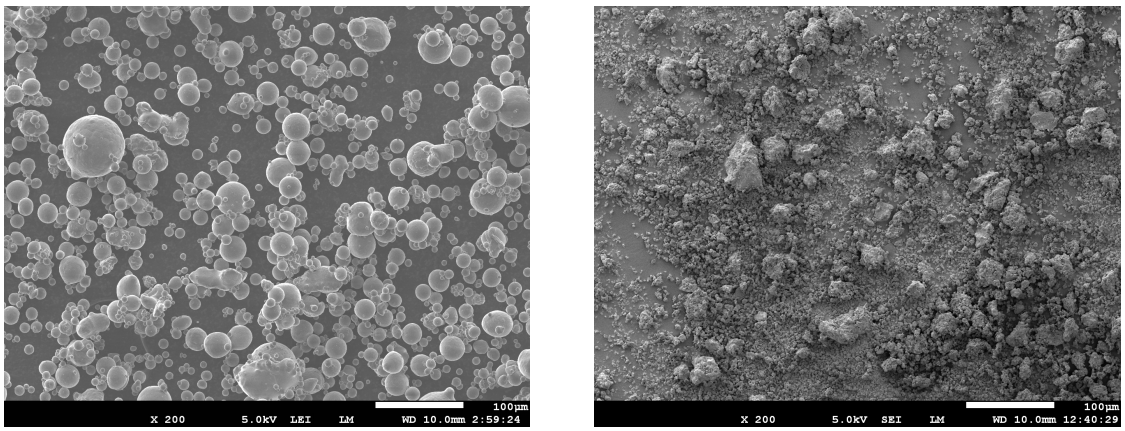

(a) *SEM image of aluminium powder*

(b) *SEM image of bismuth oxide powder*

Figure 4.5: *SEM images of additive materials with a) aluminium powder and b) bismuth oxide*

The effect of additives on the particle size distribution of the mixture is limited due to the small additive weight percentage. However, the size of the additive powders is substantially smaller than most of the MGS-1 material.

4.3. MGS-1 Thermal Behaviour

The thermal behaviour of MGS-1 was investigated by TGDMA and DSC. The former was used to determine the onset of melting and the mass-loss upon heating, the latter was used to determine the specific heat capacity of the material. After an initial TGDMA trail experiment it appeared that several chemical reactions occurred upon heating. This is discussed in a subsection on thermal stability.

Melting and Mass Loss

The TGDMA analysis was run symmetrically with a maximum temperature of 1400 °C. In Figure 4.6, only the first half of the test up to the maximum temperature is shown for clarity. The onset of melting and the mass loss as a percentage of the initial mass are shown.

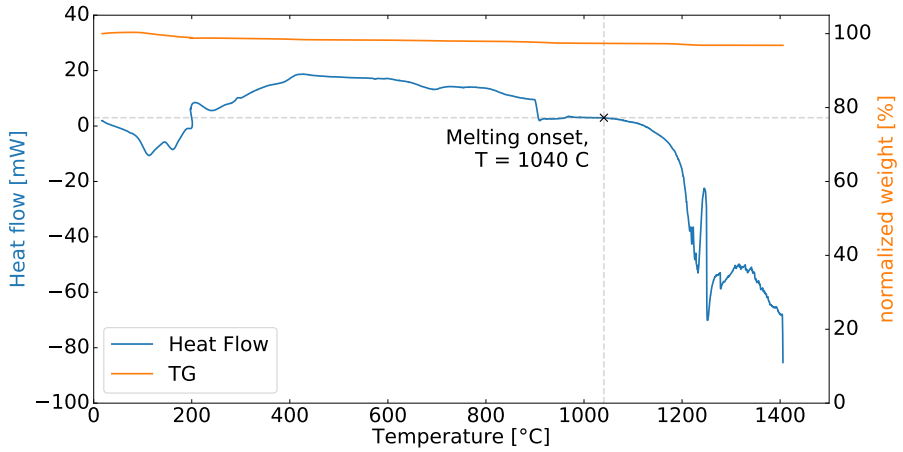

Figure 4.6: *MGS-1 heat flow and mass loss upon heating*

The graph shows a jump in heat flow around T = 950 °C. This can be explained by the change in heating rate. After T = 950 °C, the heating rate was lowered from 50 °C min^{-1} to 25 °C min^{-1} in order to improve the resolution around the suspected chemical reaction (see the subsection below). The onset of melting is defined as the point where the heat flow starts deviating from the average value of the relative constant heat flow between 950 °C and 1000 °C. Using this definition, a melting onset of approximately 1040 °C is found. Therefore, the upper bound of the sintering operations should be close to this value. The mass loss during this heating period of the TGDMA test was 2.8523 mg (or 3.1508 wt%).

Thermal Stability

Figure 4.6 shows an exothermic peak in the endothermic melting peak. This is indicative of a phase change and or a concurrent chemical reaction. A more detailed view of this suspected reaction peak is shown in Figure 4.7.

Interestingly, this possible reaction appears to coincide with a small amount of mass loss. Therefore, to get a better understanding of the process, mass spectrometry was used to try and identify any possible species that might have formed during this reaction. The result is shown in Figure 4.8.

From the graph it is clear that several different Atomic Mass Unit (AMU) values appear and disappear throughout the experiment, indicating activity within the material. Notable AMU values that fluctuate during the experiment, together with a possible explanation for these fluctuations, are summarised in Table 4.5. Other notable fluctuations occur at 12 AMU, which appears and disappears at the beginning of the experiment and 48 AMU, which shows similar behaviour.

Specific Heat Capacity

In total, three different samples were used for the specific heat capacity determination. The c_p value was determined in the temperature range for which the constant 20 °C min^{-1} heat flow was achieved. This corresponds to temperatures of 225 °C to 540 °C. The results from this computation can be seen in Figure 4.9.

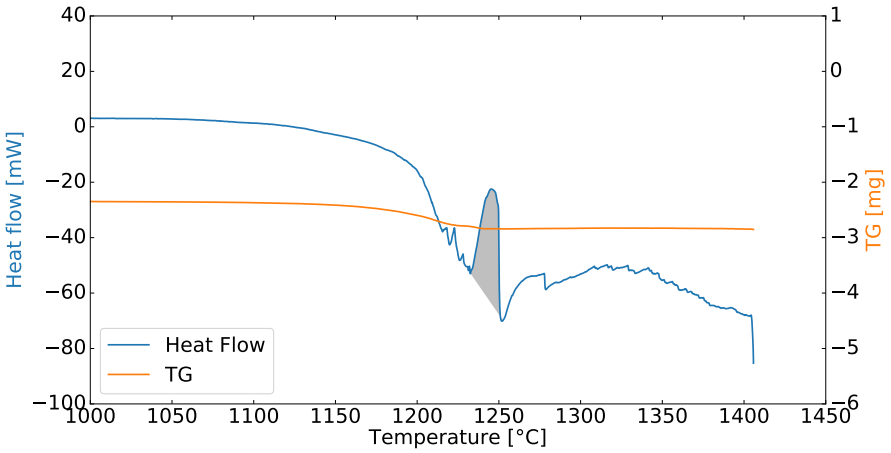

Figure 4.7: *Apparent chemical reaction in MGS-1 during heating (shaded area)*

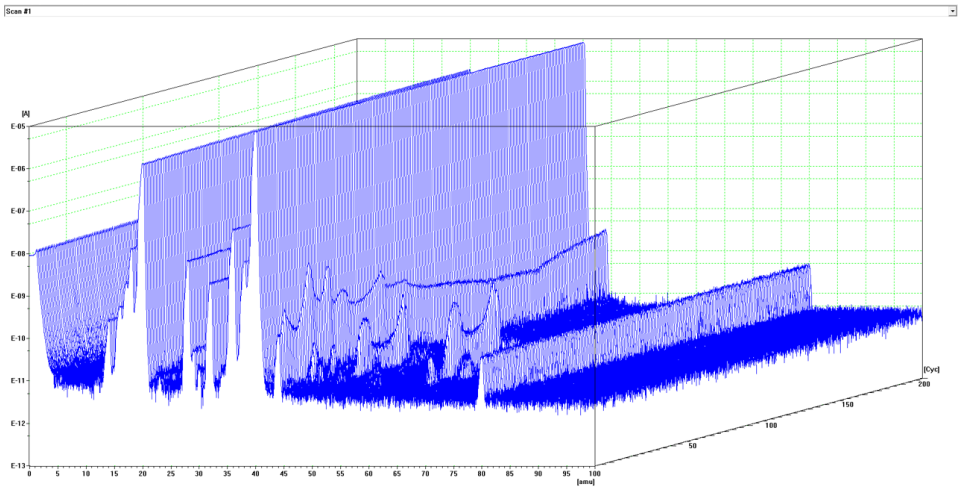

Figure 4.8: *Mass spectrometry map of the TGDMA experiment performed on baseline MGS-1 powder*

Table 4.5: *AMU fluctuations during mass spectrometry*

AMU	Behaviour	Possible species	Explanation
14	Increases at the end of experiment	N	Argon supply decreases and air becomes dominant again
18	Appears and disappears during the early experiment	H_2O	Evaporation of retained moisture
28	Increases at the end of experiment	N_2	Argon supply decreases and air becomes dominant again
32	Increases at the end of experiment	O_2	Argon supply decreases and air becomes dominant again
44	Appears and disappears during the early experiment	CO_2	Possible reaction product
64	Appears and disappears during the early experiment	SO_2	Possible reaction product

The mass loss in this temperature range obtained by TGDMA (see above) was 0.46943 g, or 0.5186 wt%. Values for the specific heat capacity varied in this temperature range between 0.8 J/g°C and

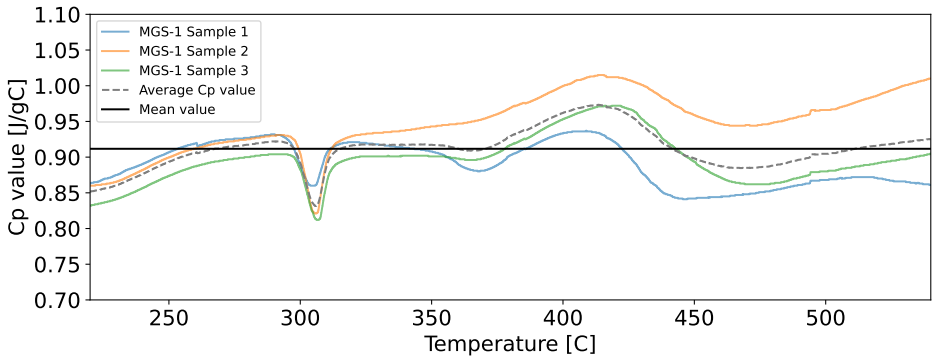

Figure 4.9: *Calculated specific heat capacity for baseline MGS-1 simulant powder*

1.05 J/g°C. The average over this temperature range is 0.912 J/g°C, which serves as a first estimate. This value correlates well with c_p values of constituent minerals in a similar temperature range [73].

4.4. MGS-1 XRD Analysis

The first pattern determined is that of the ground baseline MGS-1. This pattern, together with reference patterns from constituent minerals, is shown in Figure 4.10. A large number of reflections is observed, which is expected for a highly heterogeneous material with many crystalline components.

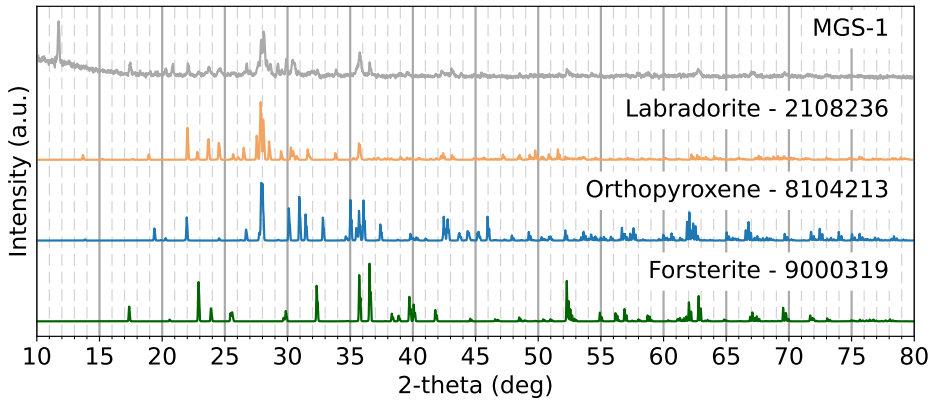

Figure 4.10: *XRD patterns for baseline regolith and constituent minerals*

The three major constituents of MGS-1 by weight are plagioclase, pyroxene and olivine, accounting for 27.1wt%, 20.3wt% and 13.7 wt% respectively. These mineral groups are represented by labradorite, orthopyroxene and forsterite respectively in Figure 4.10. The patterns for these minerals were obtained from the Crystallography Open Database (COD). COD ID numbers are indicated in the figure.

In total, six powders made from samples sintered at different temperatures, additives and particle sizes have been investigated. An overview of the obtained patterns is found in Figure 4.11.

Comparing the XRD patterns of baseline sintered MGS-1 at different temperatures, no significant changes in the pattern are observed until a sintering temperature of 1060 °C. At this temperature, the peak at 37°, associated with olivine (forsterite) disappears and a new reflection at 33° is observed. Additionally, with increasing sintering temperature, the intensity of the reflections between 20° and 25° change, with a pronounced reflection at 22° appearing.

For the aluminium enriched sample sintered at 1050 °C, most of the reflections observed in the pattern correspond to those observed for the baseline MGS-1 material, indicating that minimal chemical changes have occurred. However, the reflection at 26° and 36° appears to increase in intensity and a small reflection at 67° appears. Interestingly, for the aluminium enriched sample sintered at 1060 °C, the reflection at 37° remains and no reflection at 33° is observed.

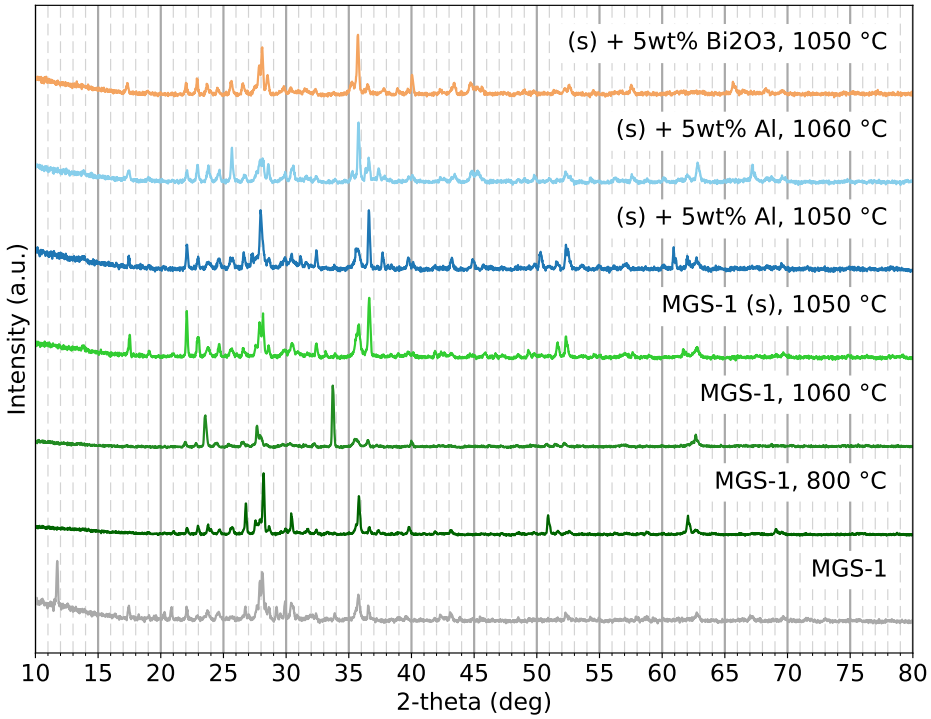

Figure 4.11: *XRD patterns for baseline as well as enriched sintered regolith at different temperatures. Samples made from sieved MGS-1 powder are indicated with "(s)".*

The pattern for Bi_2O_3 enriched material is similar. The peak at 36° appears to shift to 37° and the reflection at 28° appears to increase in intensity. Additionally, small reflections appear at 50° and 61°. The overall pattern still resembles that of baseline material well, indicating minimal chemical processes at the investigated sintering temperature for this additive.

5

The Effect of Sintering Parameters and Material on Sintered Sample Properties

Many processing parameters can be changed during the SPS process that all affect the properties of the sintered sample. From literature it is known that these properties are mostly affected by three variables. These are the applied pressure during sintering, the sintering temperature and the particle size of the used material. In this chapter, the effect of each of these parameters on the properties of sintered, baseline MGS-1 is covered. First, the effect of temperature and pressure is discussed followed by the particle size. Finally, the effect of the dwell cycle type is discussed.

5.1. The Effect of Temperature and Pressure

The effect of temperature pressure on the properties of sintered samples is evaluated by looking at three parameters: the densification, the mechanical properties and the material behaviour of sintered samples. For this analysis, samples of sintered, baseline MGS-1 are used. Two different sintering pressures are investigated, 30 MPa and 50 MPa. This corresponds to an applied sintering force of 10 kN and 30 kN respectively. Images of selected samples sintered at different sintering temperatures and pressures, after grinding, polishing and compression testing, can be seen in Figure 5.1. Note, sintering conditions and properties of all samples are listed in Appendix A. Sample descriptors correspond to those listed in Table A.3. The failure load F for each sample is also indicated.

(a) *Sample P1,* T = 800 °C, P = 30 kN, F = 8.07 N

(b) *Sample P2,* T = 900 °C, P = 30 kN, F = 11.67 N

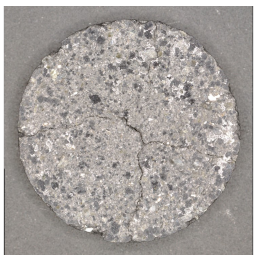

(c) *Sample P5,* T = 1060 °C, P = 30 kN, F = 88.48 N

(d) *Sample P3,* T = 800 °C, P = 50 kN, F = 15.07 N

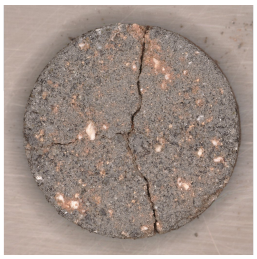

(e) *Sample P4,* T = 900 °C, P = 50 kN, F = 15.75 N

(f) *Sample P6,* T = 1060 °C, P = 50 kN, F = 244.75 N

Figure 5.1: *Microscopy images of sintered baseline samples at different sintering temperatures and pressures. Failure loads for each sample are included.*

The first thing noticed when looking at the images above is the apparent change in colour. The baseline MGS-1 regolith simulant (Figure 3.1) is reddish-brown, but appears to turn grey when sintered at high temperatures. Next, from the rough appearance of samples sintered at lower temperatures it can be deduced that the degree of sintering is low.

Temperature and Pressure Effect on Densification

The effect of the sintering pressure and temperature on the relative density of the sintered samples as a function of sintering temperature and pressure is shown in Figure 5.2. Unless otherwise specified, the samples are sintered at an applied pressure of 50 MPa.

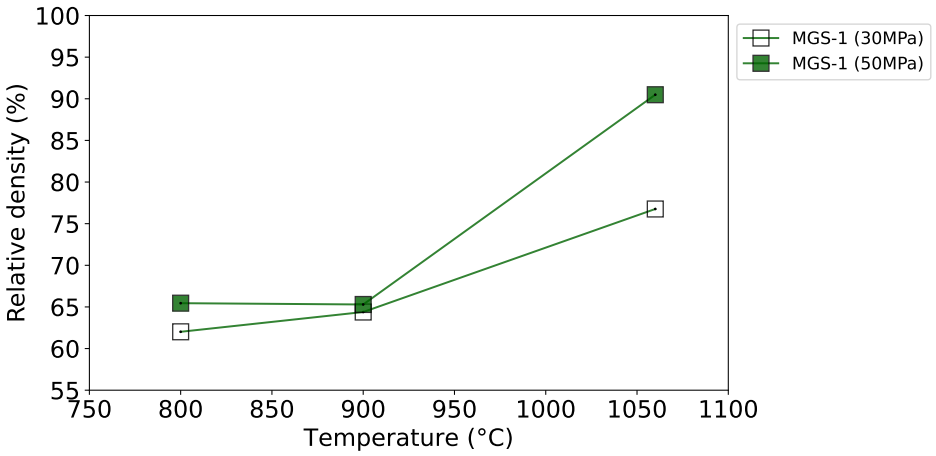

Figure 5.2: *The effect of sintering temperature on the densification of sintered baseline MGS-1. Lines indicate samples sintered at equal pressures.*

Samples sintered at identical pressures are connected with a line. Looking at Figure 5.2, the relative density hardly improves at temperatures between 800 °C and 900 °C. This is true for both the sintering temperature and sintering pressure. At higher temperatures, an increase in the relative density is observed, correlating with the improvement in consolidation observed in Figure 5.1 above. Comparing the effect of sintering temperature with sintering pressure, it can be seen that sintering temperature has a bigger impact on the relative density then the sintering pressure.

Temperature and Pressure Effect on Mechanical Properties

The effect on the mechanical properties is split in two different properties, the Young's modulus and the biaxial strength respectively. Recall that the Young's modulus is derived from the deflection curve of the ball-on-ring compression test. The biaxial strength is calculated using this Young's modulus and the results of the test. Note, no stress range correction has been applied for the results in this subsection.

Figure 5.3 illustrates the effect of the sintering temperature and pressure on the calculated Young's modulus and Figure 5.4 the effect on the biaxial strength.

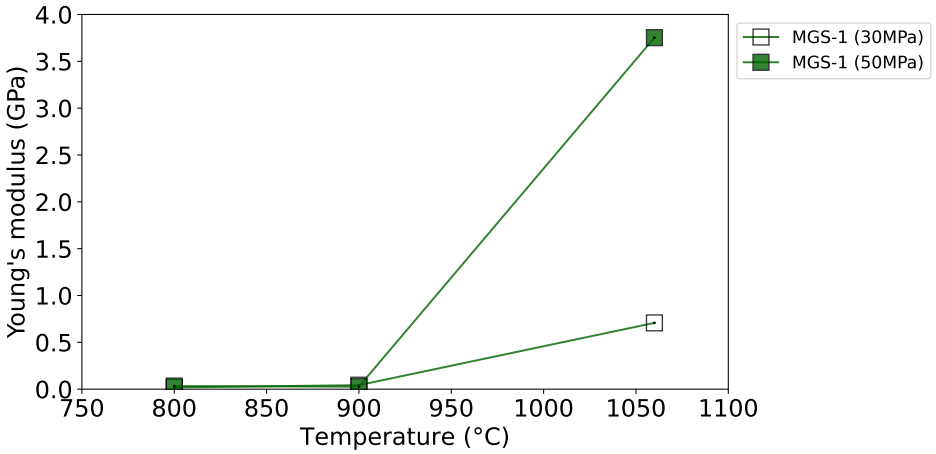

Figure 5.3: *Sintering temperature effect on the Young's modulus of sintered MGS-1. Lines indicate samples sintered at equal pressures.*

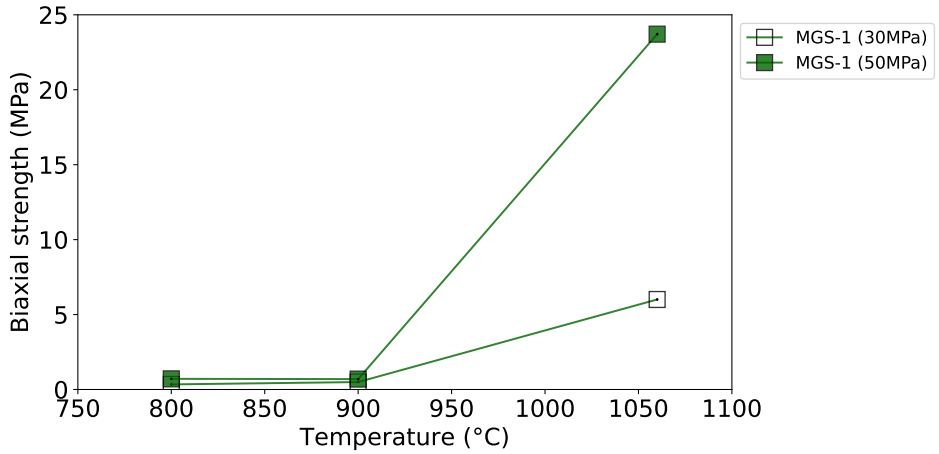

Figure 5.4: *Sintering temperature effect on the biaxial strength of sintered MGS-1. Lines indicate samples sintered at equal pressures.*

Similar to the behaviour of the relative density, little improvement is observed in both the Young's modulus and biaxial strength at sintering temperatures below 900 °C. To investigate the effect of temperature, samples sintered at the same pressure but different temperatures can be compared. Looking at the temperature effect, the Young's modulus increased by well over an order of magnitude for samples sintered at 30 MPa of pressure and by more than two orders of magnitude for samples sintered at 50 MPa of pressure. This difference is a factor of 12 and 34 for the biaxial strength and respective pressures. Similarly, to investigate the effect of sintering pressure, samples sintered at different pressures but equal temperatures can be compared. For samples sintered at 1060 °C, the Young's modulus improves by almost an order of magnitude, whereas the biaxial strength improves by a factor of 5.

It appears that, with increasing sintering temperature above 900 °C, the stiffness of the samples increases by a larger amount compared to the strength. However, with the current number of samples, not enough data is available to determine underlying and intermediate behaviour.

Temperature and Pressure Effect on Material Behaviour

The effect on material behaviour is determined using the method described in Section 3.8. Recall that the material behaviour is determined using ratio of the AUC of the force deflection plots. If the ratio is smaller than the threshold the sample is brittle, otherwise the sample is tough. Brittle samples are coloured olive green, tough samples cyan. This colour system has been applied to the biaxial strength plot, resulting in Figure 5.5. Only the sample sintered at high temperature and high pressure (50 MPa) showed brittle behaviour. All other samples showed tough behaviour.

5.2. The Effect of Particle Size

Four different particle sizes were used to sinter samples. They are baseline regolith, with a reported particle size between 0.04 µm to 600 µm, sieved powders with sizes <56 and 56 µm to 150 µm and externally sieved powder with a particle size smaller than 315 µm. Again, the effect on the densification, mechanical properties and mechanical behaviour is evaluated.

Particle Size Effect on the Densification

The relative density of sintered samples from the four different particle sizes is shown in Figure 5.6. The sample was sintered at 50 MPa pressure if no other pressure is indicated.

It is clear that the as received particle size shows the largest spread in relative density. Samples sintered with different particle sizes mostly fall within these boundaries. Controlling the particle size range improves the spread in relative densities, indicating an increase in property control. Contrary to expectations, smaller particle sizes do not correspond to increasing properties, in this case an increase in relative density.

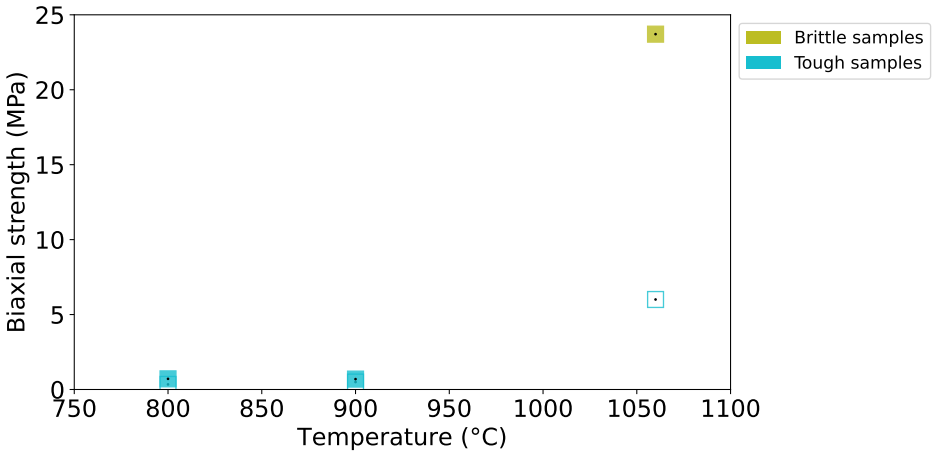

Figure 5.5: *Effect of sintering temperature on material behaviour of baseline sintered samples. Open squares indicate samples sintered at an applied pressure of* 30 MPa *and filled squares at* 50 MPa*.*

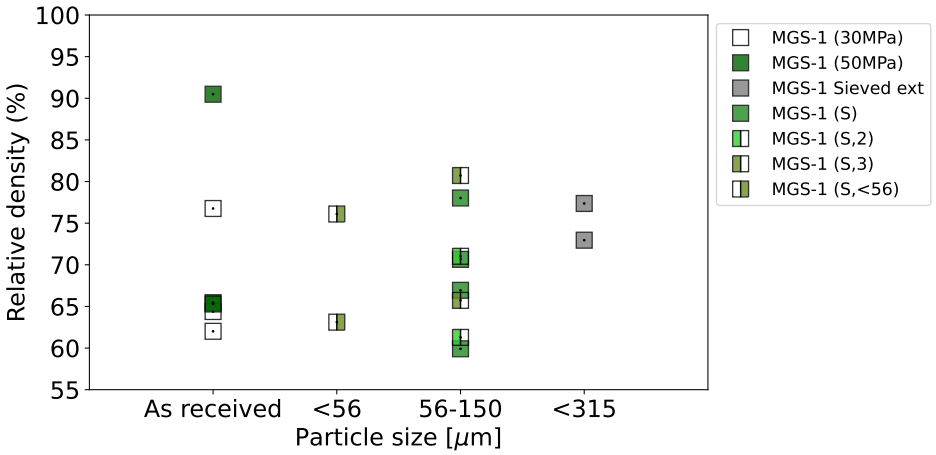

Figure 5.6: *The effect of particle size on the densification of baseline sintered MGS-1. Sieved materials are indicated with "(S)", followed by either the sieving batch or additional information.*

Particle Size Effect on Mechanical Properties

Similar trends are observed in the mechanical properties, Figure 5.7 and Figure 5.8. Again, controlling the particle size results in a smaller spread in properties. Decreasing the particle size does not seem to result in a reproducible improvement in properties.

Particle Size Effect on Material Behaviour

Different particle sizes seem to have little effect on the material behaviour of sintered samples, Figure 5.9. The biaxial strength appears to play a role in the material behaviour.

5.3. The Effect of Dwell Cycle

The temperature and pressure hold, or dwell cycle, has an effect on sintered sample performance. Two different dwell cycles were investigated. The default dwell cycle consisted of a ten-minute pressure and 15-minute temperature hold; the alternative reversed the respective holding times. The default sintering cycle is shown in Figure 3.5. Only samples made from sieved material are discussed in this section.

Dwell Cycle Effect on the Densification

A longer pressure hold (right hand side of Figure 5.10) appears to increase the average relative density of sintered samples. However, the spread in properties of the reverse method is within that of the

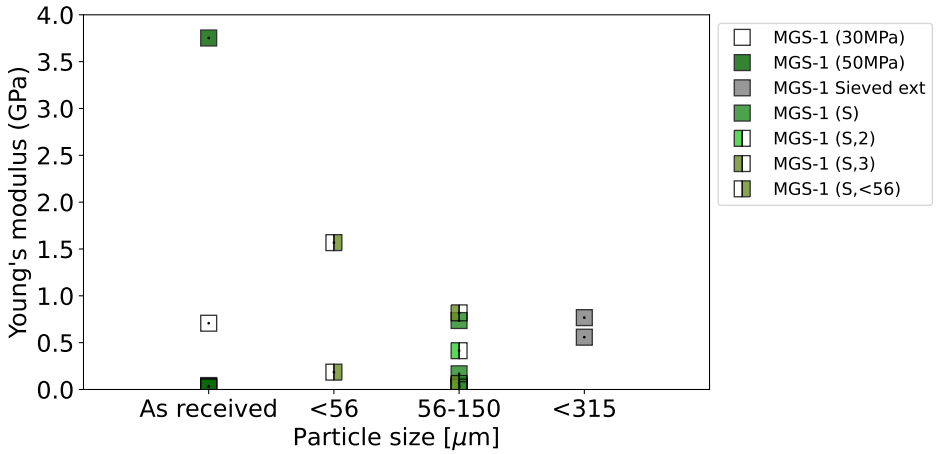

Figure 5.7: *Particle size effect on the Young's modulus of sintered baseline MGS-1*

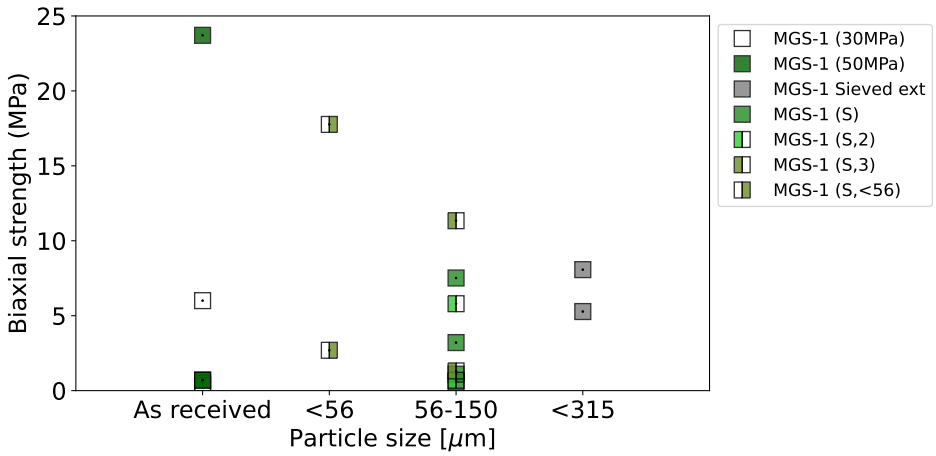

Figure 5.8: *Particle size effect on the biaxial strength of sintered baseline MGS-1*

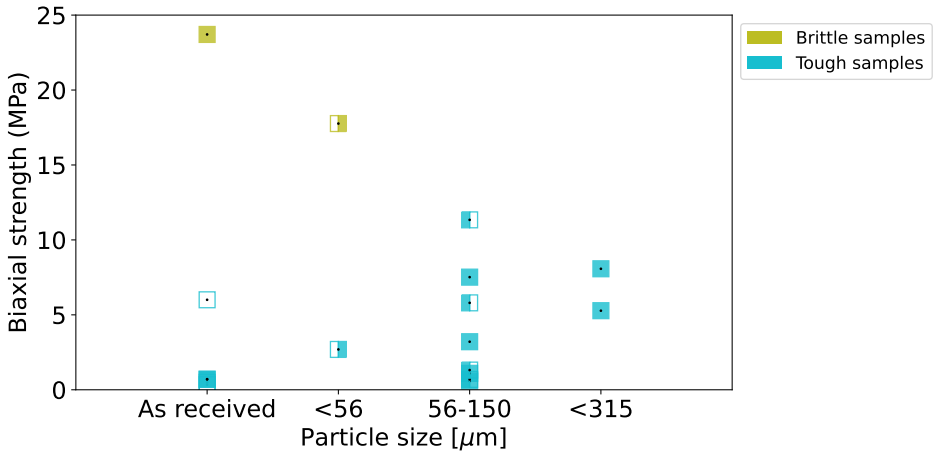

Figure 5.9: *Effect of particle size on material behaviour of baseline sintered samples. Different markers indicate different materials as in the previous figure.*

default. Hence, this specific dwell cycle does not notably affect densification.

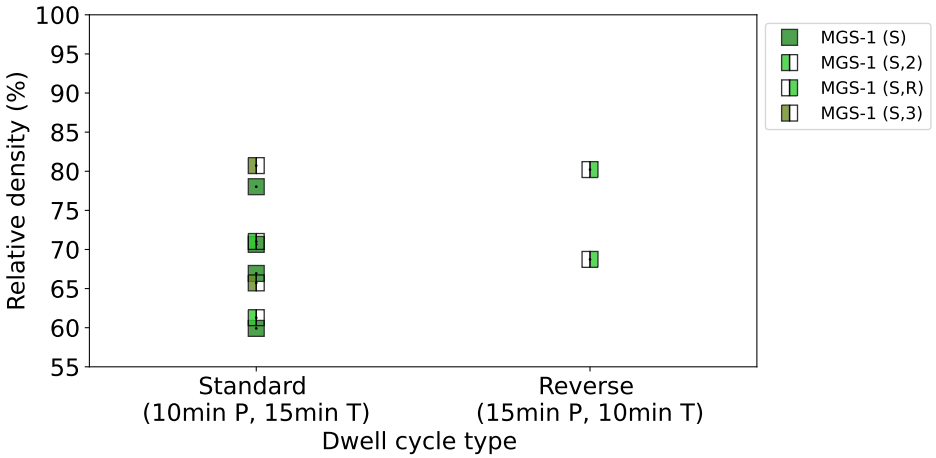

Figure 5.10: *The effect of the dwell cycle on the densification of sintered baseline MGS-1*

Dwell Cycle Effect on Mechanical Properties

The Young's modulus, Figure 5.11, and biaxial strength, Figure 5.12, show very similar behaviour for the two different dwell cycles. No significant difference in properties between the two cycles is observed.

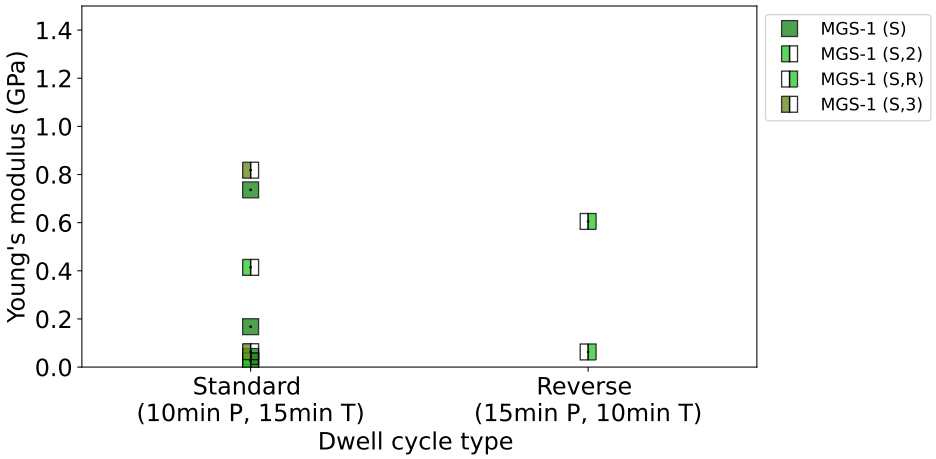

Figure 5.11: *Dwell cycle effect on the Young's modulus of sintered baseline MGS-1*

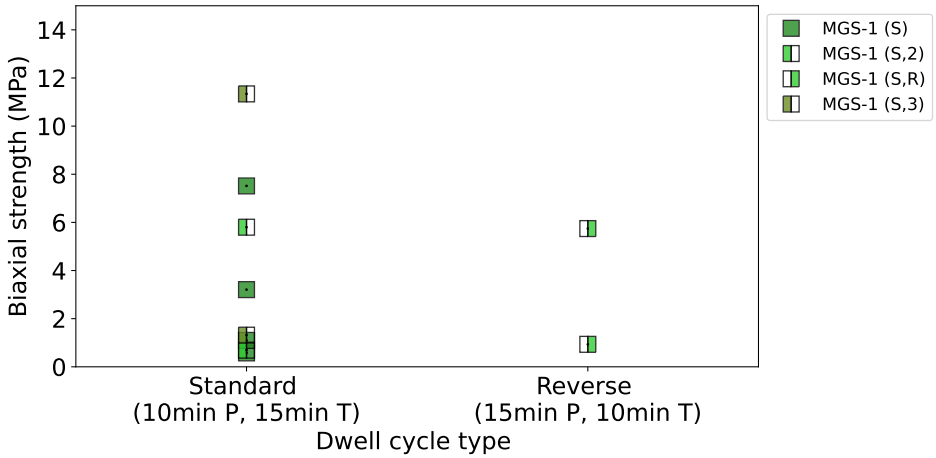

Figure 5.12: *Dwell cycle effect on the biaxial strength of sintered baseline MGS-1*

Dwell Cycle Effect on Material Behaviour

The alternative dwell cycle does not result in a change in material behaviour, Figure 5.13. None of the samples evaluated for the dwell cycle effect show brittle behaviour. Additionally, none of the samples exhibited biaxial strengths high enough (>13 MPa) for previously observed brittle behaviour. This fortifies the notion that biaxial strength and material behaviour are linked.

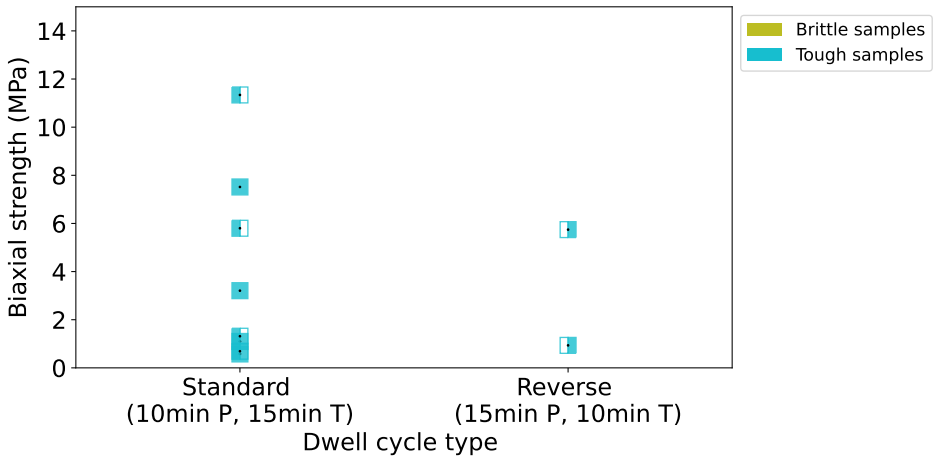

Figure 5.13: *Effect of dwell cycle on material behaviour of baseline sintered samples. Markers correspond to different sieve batches.*

6

The Effect of Additives on Sintered Sample Properties

Using sintering aids to improve results is common practice [8, 43]. To improve the properties of sintered Martian regolith simulant, two different sintering aids, aluminium and bismuth oxide, are investigated. Both additives are aimed at providing a liquid phase during sintering, with the aim of improving densification and sample properties.

In this chapter, the effects of both of these additives on the properties of sintered samples are discussed. Specific properties of interest are the densification of the samples and the mechanical properties (Young's modulus and biaxial strength). First, in Section 6.1, an introduction to the presented results is given. The effects of adding aluminium and bismuth oxide are discussed in Section 6.2 and Section 6.3 respectively. Two different weight fractions, 2.5 and 5 wt% were investigated per additive. Following the discussion on individual additives, the effect of additive amount is presented in more detail in Section 6.4.

6.1. Introduction to the Effects of Additive Results

Many samples were created and tested to evaluate the sintered sample properties. The validity and reproducibility of the results were two of the key drivers for creating the total number of samples. Samples with aberrant physical and mechanical behaviour were recreated and the properties re-assessed and compared to expectations. In this chapter, these deviating samples have been omitted from the analysis. Additionally, only results from sieved samples of the medium size fraction (56-150 micron) are presented. An overview of sintering conditions and properties of all samples can be found in Appendix A.

All shown samples were sintered at temperatures above the melting temperature of bismuth oxide and that of aluminium (817 °C and 668 °C, see Table 3.4) to ensure a liquid phase during sintering. The maximum temperature for these experiments was set to 1050 °C, based on the observed melting onset of MGS-1. All samples were sintered at 50 MPa of applied pressure using the default dwell cycle.

For the assessment of the mechanical properties of the samples, a stress range was applied following the method of Subsection 3.7.3. As a threshold value, only samples with a biaxial strength larger than 10 MPa were used. This value was based on the average biaxial strength of mortar reference samples, see Appendix B, Subsection B.2.2. The effect of this stress range correction is discussed in Appendix B, Section B.3.

In the following sections the improvement of the aforementioned properties is presented. The improvement is calculated per sample based on the average performance of the baseline samples (without additives) for each sintering temperature. However, note that the values shown for the improvement in Young's modulus and biaxial strength are calculated using material properties *before* applying the stress range correction. As shown in Appendix B, the Young's modulus is strongly affected by this correction, whereas the biaxial strength is hardly affected. The improvement plots for the relative density are unaffected by the application of the stress range correction. For the legends of the figures in this chapter, "(S, *X*)" indicates sieved material from batch *X* and mixed materials are indicated by a sieving batch plus additive material and amount.

6.2. Effect of Aluminium Additive

In this section the effect of adding aluminium on the properties of sintered MGS-1 is presented. First, the effect on the densification is discussed, followed by the effect on the mechanical properties.

Effect of Aluminium Addition on Densification

The calculated relative density of aluminium enriched samples sintered at different temperatures is shown in Figure 6.1. Different markers indicate different powder mixtures and different colours indicate different sieving batches.

Comparing the trends in relative density (lines in the plot), it can be observed that the relative densities of aluminium enriched samples is higher than those observed for baseline MGS-1. This is true for both amounts of additive. However, the 2.5 wt% additive samples sintered at low temperatures exhibit properties close to those of baseline samples. Additionally, it appears the improvement of aluminium enriched samples, regardless of additive amount, is lower at higher sintering temperatures.

The improvement in relative density with sintering temperature is plotted in Figure 6.2. From the figure it becomes clear that the improvement in densification does not go over 20% and indeed decreases with increasing temperature.

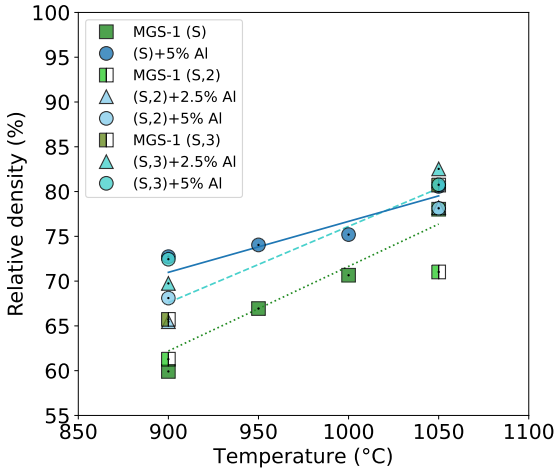

Figure 6.1: *The effect of 2.5wt% (dashed line) and 5 wt% (solid line) Al additive on the densification of sintered MGS-1. Baseline samples are shown for reference (dotted line).*

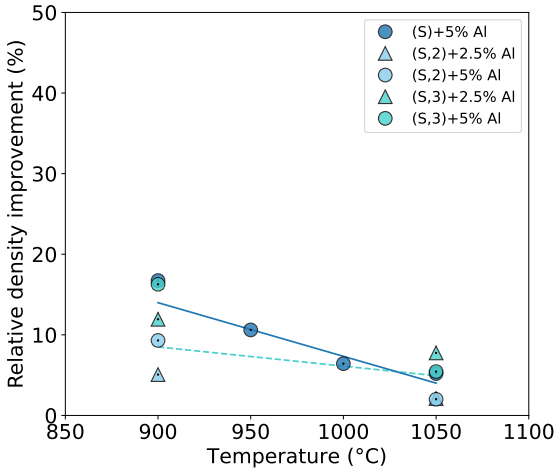

Figure 6.2: *Improvement in densification for aluminium enriched samples as compared to the MGS-1 baseline. Solid and dashed line represent 5wt% and 2.5wt% enriched samples respectively, no stress range correction applied.*

Effect of Aluminium Addition on Mechanical Properties

The effect on the mechanical properties is split in two parts: the effect on the stiffness and the strength. This stiffness is calculated from the force-deflection curve as discussed in Subsection 3.7.1.

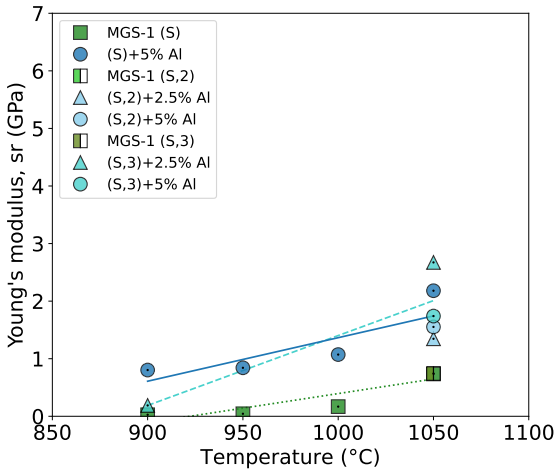

Figure 6.3: *The effect of 2.5wt% (dashed line) and 5 wt% (solid line) Al additive on the stiffness of sintered MGS-1. Baseline samples are shown for reference (dotted line).*

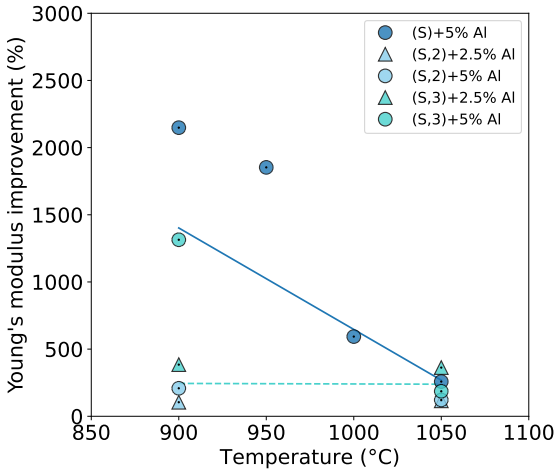

Figure 6.4: *Improvement in stiffness for aluminium enriched samples as compared to the MGS-1 baseline. Solid and dashed line represent 5wt% and 2.5wt% enriched samples respectively, no stress range correction applied.*

Figure 6.3 shows that the Young's modulus of sintered baseline MGS-1 only notably increases for sintering temperatures above 1000 °C. A similar trend is observed for aluminium enriched samples. Interestingly, there appears to be little difference between 2.5 and 5wt% enriched powders.

The stiffness of enriched samples is considerably higher at a sintering temperature of 1050 °C, but most of the improvement is observed at lower sintering temperatures (Figure 6.4). In this temperature range, the difference in densification is also larger. However, at a sintering temperature of 1050 °C, the densification of aluminium enriched samples is only slightly improved compared to plain material.

A similar increasing trend for the biaxial strength is observed in aluminium enriched samples, Figure 6.5. Again, the baseline level for aluminium enriched samples is higher than that of baseline samples. However, comparing the generally observed trends by looking at the lines to guide the eye, it can be seen that the increase in biaxial strength seems to start earlier than the onset of stiffness improvement. The onset of improved biaxial strength seems to start at sintering temperatures above 950 °C.

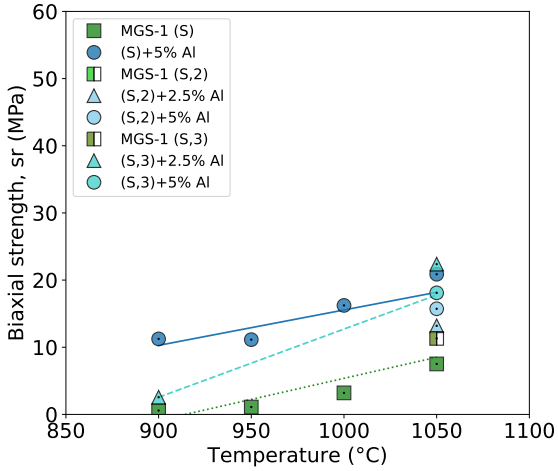

Figure 6.5: *The effect of 2.5wt% (dashed line) and 5 wt% (solid line) Al additive on the biaxial strength of sintered MGS-1. Baseline samples are shown for reference using a dotted line.*

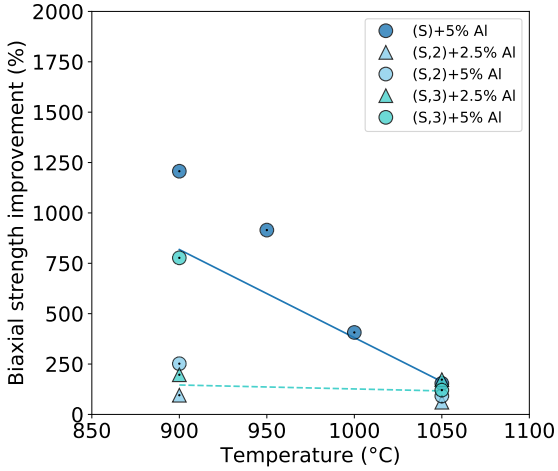

Figure 6.6: *Improvement in biaxial strength for aluminium enriched samples as compared to sintered baseline MGS-1. The solid and dashed line represent 5wt% and 2.5wt% enriched samples respectively. Note, stress range correction has not been applied.*

The improvement in the biaxial strength of aluminium enriched samples is shown in Figure 6.6. A similar shape to the Young's modulus improvement is observed, with most of the benefit obtained at lower sintering temperatures. At higher sintering temperatures, the properties become similar to pure MGS-1 sintered samples. Again, no notable difference at high sintering temperatures is observed between 2.5 or 5 wt% enriched samples.

6.3. Effect of Bismuth Oxide Additive

The effect of adding 2.5 or 5 wt% additive to MGS-1 on the properties of sintered samples is discussed below. Properties are discussed in the order of the previous section.

Effect of Bismuth Oxide on Densification

Figure 6.7 shows the relative density of sintered samples enriched with bismuth oxide compared to those of pure MGS-1. Again, two different weight fractions of additive were investigated. Again, it can be observed that the enriched samples outperform the baseline values. One sample sintered at 1050 °C even obtained a relative density close to 100% and is considered fully dense.

Contrary to the aluminium enriched samples, a clear difference can be observed for the different additive weight fractions. Generally, the 5wt% doped bismuth oxide samples outperform those with 2.5wt% dopant. Additionally, it can be observed that the spread in relative densities obtained for bismuth oxide enriched samples is larger than their aluminium enriched counterparts.

The improvement in densification for bismuth oxide enriched samples is shown in Figure 6.8. Improvements in the order of 10 to 40% are observed. For both the 2.5 wt% and 5 wt% additive samples,

the improvement appears to decrease with increasing temperatures.

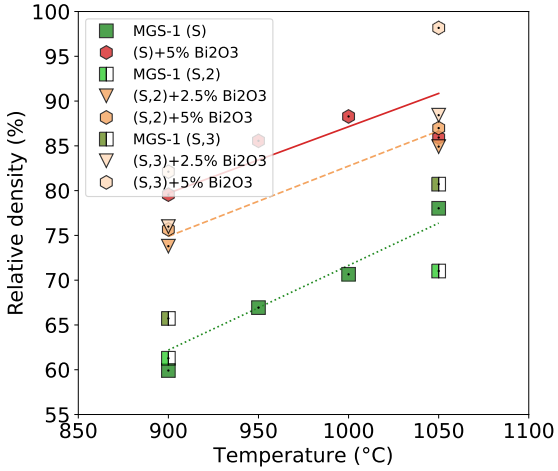

Figure 6.7: *The effect of 2.5wt% (dashed line) and 5 wt% (solid line) bismuth oxide additive on the densification of sintered MGS-1. Baseline samples are shown for reference using a dotted line.*

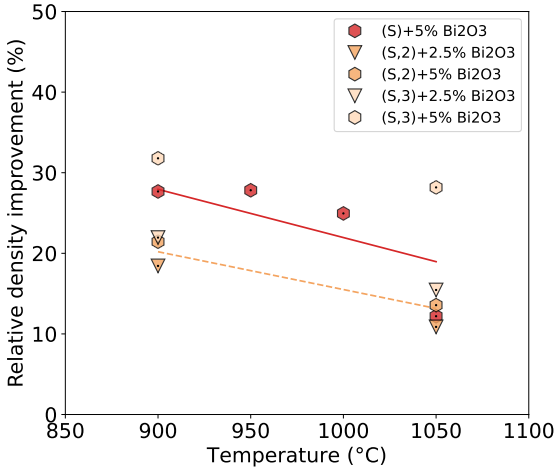

Figure 6.8: *Improvement in densification for bismuth oxide enriched samples as compared to sintered baseline MGS-1. The solid and dashed line represent 5wt% and 2.5wt% enriched samples respectively. Note, stress range correction has not been applied.*

Effect of Bismuth Oxide on Mechanical Properties

The stiffness of bismuth oxide doped samples also significantly improves as compared to the base MGS-1 material. The calculated values for the Young's moduli for this additive are shown in Figure 6.9. A large spread in stiffness values is observed, similar to the spread in relative density. Larger amounts of additive again perform better.

Compared to aluminium enriched samples, which only showed an increasing trend in stiffness for sintering temperatures over 1000 °C, the bismuth oxide enriched system appears to exhibit this increasing trend at sintering temperatures starting at 900 °C.

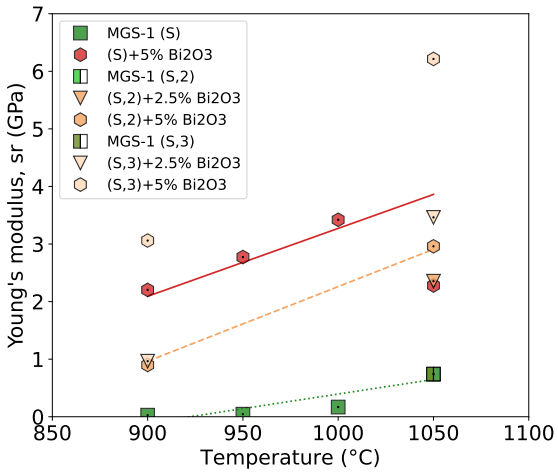

Figure 6.9: *The effect of 2.5wt% (dashed line) and 5 wt% (solid line) bismuth oxide additive on the Young's modulus of sintered MGS-1. Baseline samples are shown for reference using a dotted line.*

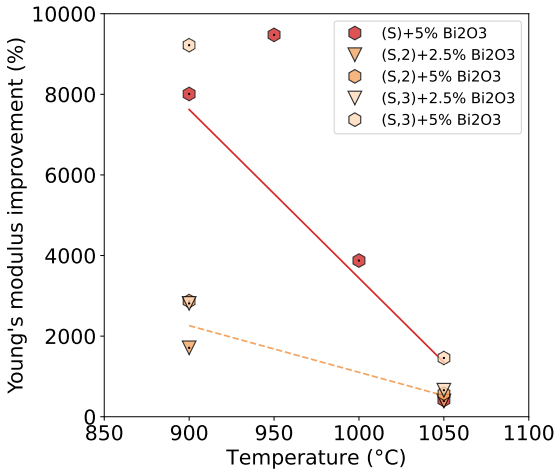

Figure 6.10: *Improvement in Young's modulus for bismuth oxide enriched samples as compared to sintered baseline MGS-1. The solid and dashed line represent 5wt% and 2.5wt% enriched samples respectively. Note, stress range correction has not been applied.*

The stiffness improvement for bismuth oxide enriched samples is shown in Figure 6.10. A large improvement of almost two orders of magnitude can be observed at lower sintering temperatures. At higher sintering temperatures, the improvement decreases but still more than doubles compared to the performance of sintered baseline material. In terms of stiffness, it is clear that larger dopant amounts

result in larger improvements.

In line with the expectations from the increase in Young's modulus, the biaxial strength of bismuth oxide enriched samples far outperforms those of baseline material, see Figure 6.11. The same large spread in calculated strength again observed, but the improvement is less compared to that of the Young's modulus (Figure 6.12). Again, the improvement starts at sintering temperatures above 900 °C.

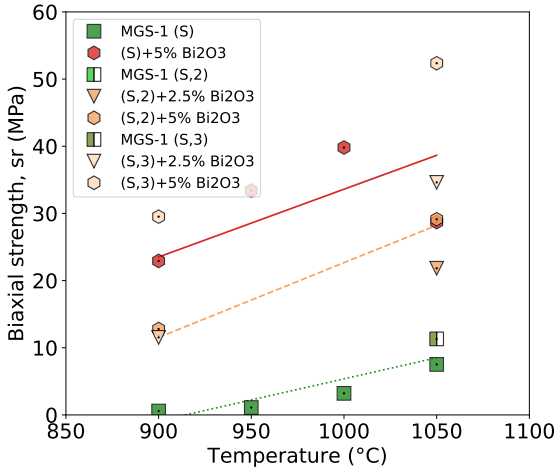

Figure 6.11: *The effect of 2.5wt% (dashed line) and 5 wt% (solid line) bismuth oxide additive on the biaxial strength of sintered MGS-1. Baseline samples are shown for reference using a dotted line.*

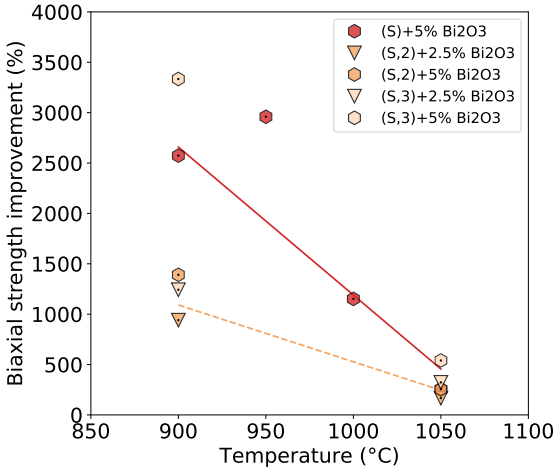

Figure 6.12: *Improvement in biaxial strength for bismuth oxide enriched samples as compared to sintered baseline MGS-1. The solid and dashed line represent 5wt% and 2.5wt% enriched samples respectively. Note, stress range correction has not been applied.*

In terms of the biaxial strength improvement, a very similar trend is observed in which the most benefit is gained at lower sintering temperatures compared to higher ones. However, similar to the Young's modulus, the biaxial strength at high sintering temperatures is still several times higher. The trends for different weight percentages still persist.

6.4. Effect of Different Additive Weight Fractions

The above results show that adding sintering aids to MGS-1 notably improves the properties of sintered samples. However, in the results presented above, it is unclear what the effect of the different weight fractions is. Therefore, in this section, the properties are plotted as a function of weight percentage additive. For the figures in this section, the same biaxial strength requirement and stress range correction has been applied as in the sections above. For clarity in the figures, the results of different additives are horizontally separated.

6.4.1. Effect Additive Amount on Densification

Figure 6.13 illustrates the relative density of sintered samples as a function of the weight percent additive. Unsurprisingly, the relative density of samples with two-and-a-half weight percent additive fall between that of baseline material and 5wt% additive.

Looking at Figure 6.13, the relative density of aluminium enriched samples hardly changes between 2.5 and 5wt% additive, as indicated by the vertical spread in the data, which is in line with previous observations. The blue lines indicate that adding more aluminium does not necessary result in increasing densification. Bismuth oxide enriched samples appear to show an increase in relative density with increasing weight percent additive. Considering the trend, lower weight fractions of bismuth oxide might still result in a considerable increase in densification.

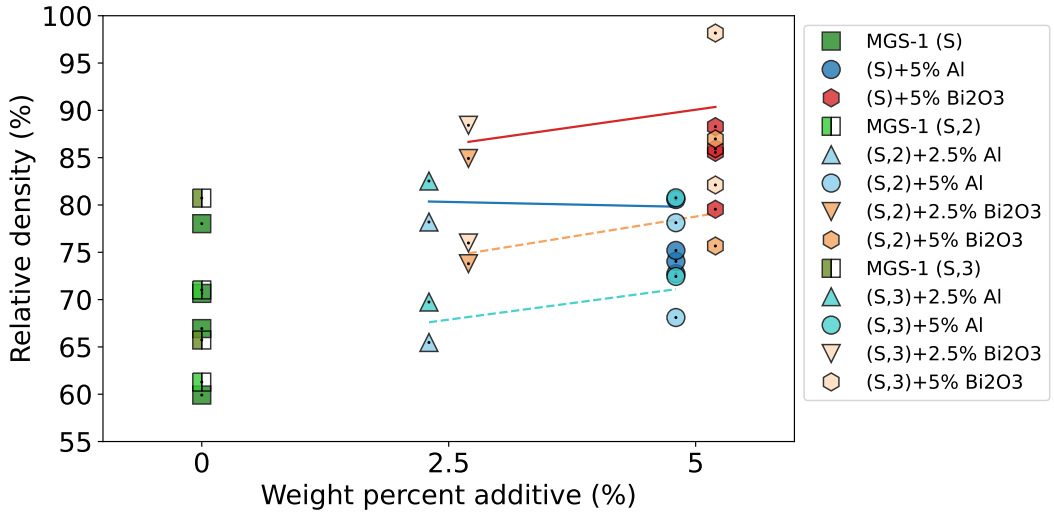

Figure 6.13: *The effect of additive weight percentage on densification. The general trend for samples sintered at high (1050 °C) and lower temperature (900 °C) are shown using solid and dashed lines respectively.*

6.4.2. Effect of Additive Amount on Mechanical Properties

In Figure 6.14 and Figure 6.15 show the effect of additive percentage on the Young's modulus and biaxial strength respectively. Note, in these plots the baseline material samples are shown.

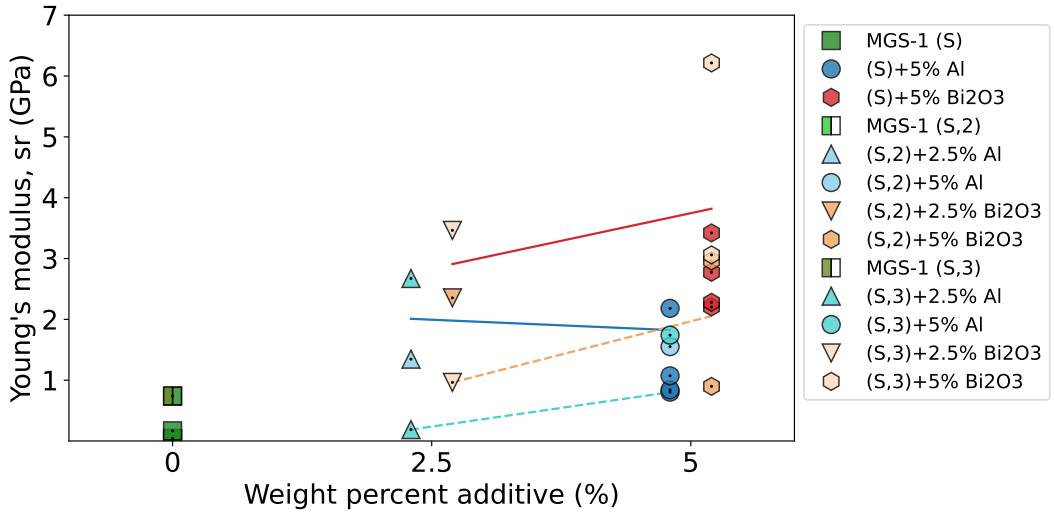

Figure 6.14: *The effect of additive weight percentage on the Young's modulus. The general trend for samples sintered at high (1050 °C) and lower temperature (900 °C) are shown using solid and dashed lines respectively.*

The properties of both additives for both weight percentages are again higher than those of baseline material. Due to the low number of samples, it is impossible to explain whether the samples enriched with 2.5 wt% aluminium have a higher stiffness than their 5wt% counterparts. Bismuth oxide shows a general increasing trend in stiffness for increasing weight percentage. It is also important to note the large spread in properties for a single weight percentage, indicating low reproducibility of results.

The biaxial strength shows similar behaviour as the Young's modulus. Again, the properties of aluminium enriched samples appear relatively independent of additive weight percentage and the properties of bismuth enriched samples appear to increase with increasing additive weight percentage. The same large spread in properties is also present.

The relative increase in properties of samples with 2.5wt% additive can be calculated. For aluminium enriched powders, this increase at a sintering temperature of 1050 °C compared to baseline material is a factor of 1.9 for the biaxial strength. For bismuth oxide enriched powders, this improve-

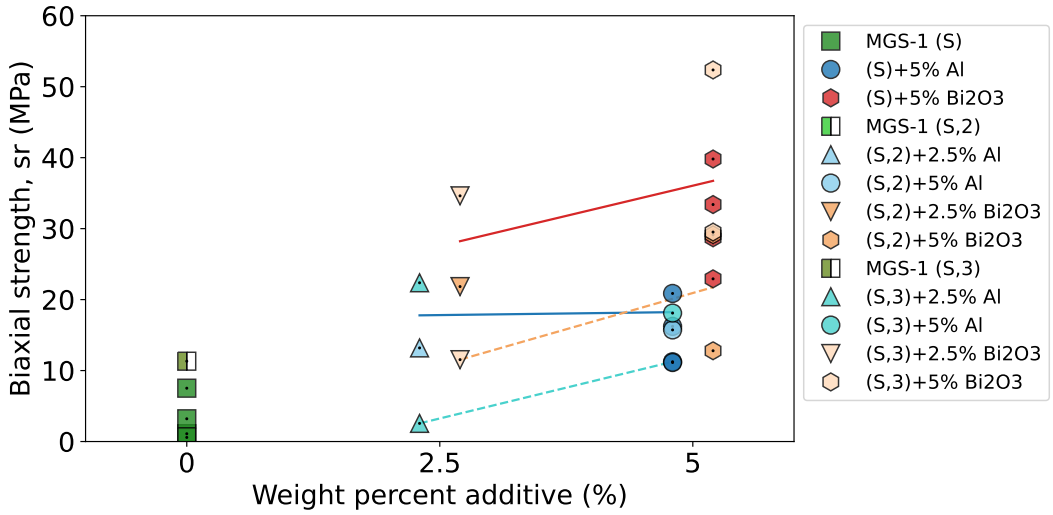

Figure 6.15: *The effect of additive weight percentage on the biaxial strength. The general trend for samples sintered at high (1050 °C) and lower temperature (900 °C) are shown using solid and dashed lines respectively.*

ment is a factor of 3. Comparing this to the increase in performance of the 5wt% case, it is seen that the improvement of the aluminium enriched samples is comparable, whereas the bismuth oxide enriched samples show a clear increase in properties with increasing weight percentage.

6.4.3. Effect of Additive Material and Amount on Material Behaviour

For the samples considered above, the material behaviour is plotted in Figure 6.16. Recall that the material behaviour is based on the ratio of the area under the curves before and after the maximum load in the force-deflection plots, see Section 3.8. All samples with 5wt% additive displayed brittle behaviour, irrespective of what type of additive was used. Some samples enriched with 2.5wt% additive displayed tough behaviour. This behaviour was observed for both an aluminium and bismuth oxide enriched sample. All of these samples were sintered at 900 °C. Sintered baseline material exhibited tough behaviour. It appears that the material behaviour is a function of both additive weight percentage and sintering temperature.

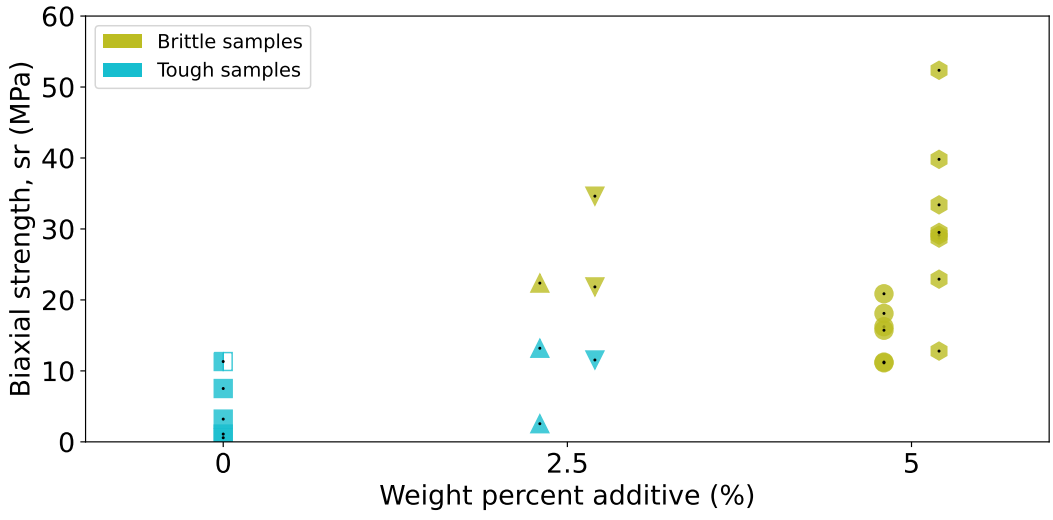

Figure 6.16: *The effect of additive weight percentage on the material behaviour of sintered MGS-1. Markers indicate samples made from baseline material (square), 2.5wt% aluminium (circle), 5wt% aluminium (triangle), 2.5wt% Bi_2O_3 (inverse triangle) and 5wt% Bi_2O_3 (hexagon),*

Alternatively, the material behaviour can be plotted against the biaxial strength of the samples. This graph is shown in Figure 6.17. Note, for this graph all samples are used, not just the ones made from sieved material with a strength mostly exceeding 10 MPa as used above. Boxes in the graph indicate the biaxial stress range of each material behaviour type for each sample group.

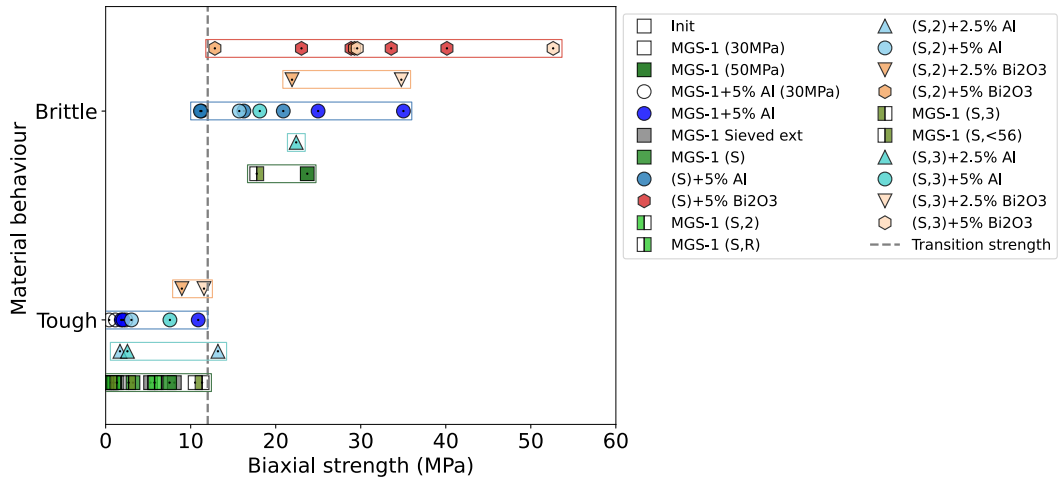

Figure 6.17: *Biaxial strength vs material behaviour of sintered MGS-1. Boxes indicate the range in biaxial strength of each type for each sample group. Some materials weaker than* 10 MPa *are also included.*

Similar to the previous graph, 5wt% additive samples overwhelmingly exhibit brittle behaviour, only one aluminium enriched sample of unsieved material exhibited tough behaviour. Additionally, it can be observed that the range of brittle behaviour of the 2.5wt% samples mostly fall within the 5wt% counterpart. A transition from tough to brittle behaviour appears to occur at around a 12 MPa biaxial strength value, this is indicated in the figure as a grey dotted line.

7

Discussion

In this chapter the discussion of the current thesis research is presented. First, in Section 7.1, the fitness of the used MGS-1 simulant is compared to the actual Martian regolith material and possible effects of any discrepancies are discussed. Next, the validity of the obtained results is briefly discussed in Section 7.2. In Section 7.3, the effect of SPS settings and particle size on sample properties is discussed, followed by an analysis of the effect of additives on sample properties. In Section 7.5 a comparison between literature data and the results obtained in this thesis is given. Finally, a link to the application on Mars is presented.

7.1. Fitness of MGS-1 compared to actual Martian regolith

When comparing the chemical composition of actual Martian regolith to that of MGS-1, good agreement is observed. Small discrepancies exist in sulphur, phosphorus and titanium containing compounds (Table 4.1).

Comparing physical properties (particle size, shape and distribution), the fitness of MGS-1 decreases. The particle size falls well within the observed range on Mars [7]. From our experiments, particles larger than specified were also observed. Karl et al. made similar observations [74]. The occurrence of bigger particles can possibly be attributed to particle agglomeration, but also to particles with one size dimension larger than 600 µm as observed with SEM imaging.

The particle size distribution shows more discrepancies. The bimodal distribution observed on Mars was faintly observed in the MGS-1 simulant, but the two modal populations appeared at slightly different particle sizes and the distinction between the modes was notably less than observed on Mars. Especially the second population occurs just below the mode observed by Weitz et al. [7]. Bimodal distributions in particle size have an effect on particle packing, with the underlying idea that smaller particles fit in interstitial spaces created by bigger particles.

More differences are observed when looking at the particle shapes. Observed particles shapes by Weitz et al. show sub-angular to rounded grains with high levels of circularity [7]. Observed particles in this research showed considerably lower circularities. Mostly angular to sub-angular particles were observed. This difference is most likely due to the manufacturing methods used to create MGS-1.

The discrepancies above all indicate that the packing density of MGS-1 is lower compared to actual Martian material. This has an effect on the densification observed during sintering, as higher packing factors improve particle contact and hence densification. Densification with actual Martian regolith is expected to increase due to the anticipated improved particle packing. In conclusion, the overall fitness of MGS-1 is considered to be good. However, some improvements are possible. Special attention needs to be paid to the physical properties (particle size and shape) of the MGS-1 simulant in order to ensure a better match with actual Martian material.

7.2. Validity of Obtained Results

The ball-on-ring compression method used during this thesis is a non-standardised compression test method. Therefore, it is important to validate the obtained results using well-known reference samples. In this thesis, two different reference materials were tested: zirconia disks and soda-lime glass disks. The properties were tested and compared to literature. For an in-depth review of the validation steps and outcomes, the reader is referred to Appendix B.

The validation experiments showed that the calculated biaxial strength of reference samples corresponds to values found in literature. Furthermore, experiments performed using the soda-lime glass specimens showed that the Young's modulus approximation calculated from the force-deflection curve

deviates notably from the actual value. The difference increases with increasing thickness. However, since the sample Young's modulus has little effect on the biaxial strength, those results are not affected. Still, the calculated values for the Young's modulus of sintered samples should be regarded as a conservative ball-park estimate. It is expected that the results obtained in this thesis for the biaxial strength of sintered MGS-1 samples are representative of the actual properties.

7.3. Effect of SPS Settings and Particle Size on Sample Properties

From the graphs of the sintering onset and saturation of all samples (not reported), it became clear that the chosen dwell time of 10 min was enough to reach sintering saturation. Based on literature, the effect of sintering temperature and sintering pressure was assumed to affect the sintered sample properties the most. The results of the variation of these two parameters seems to indicate that the effect of temperature is larger than the effect of pressure. This result was also observed for sintered lunar regolith simulant using SPS by Zhang et al. [75]. The larger effect of temperature can be attributed to the improved densification mechanisms with increased temperature. From the analysis of the number of radial fractures, no apparent difference due to SPS settings or sample properties was observed.

Four different particle sizes were investigated. The first was baseline (as received) material, the other three sieved material. Sieved material with smaller particle sizes is expected to result in better densified samples due to the higher surface energy and more locations where sparks can occur. However, contrary to this expectation, no obvious improvement in sample strength was obtained for smaller particle sizes. A similar observation was made by Eser and Kurama [76]. No apparent reason for this observation was found, but there might be relation to sample preparation. One possibility is the formation of agglomerates during mixing. After mixing, these are not broken up. It is known that agglomerates can prevent full densification [42]. Alternatively, in the pre-pressing stage before entering the SPS machine, particle fracture possibly occurred, decreasing the actual particle size, increasing compaction and surface energy and resulting in very similar powders. These hypotheses still remain to be tested. However, particle fissure is not expected at the relatively low pressure of 30 MPa during pre-pressing, as it is generally attributed to much higher pressures [48].

7.4. Effect of Additive Material and Amount on Properties

In terms of physical properties, the use of additives increased the density of the sintered samples. This effect was present for both additive amounts and both additive materials. Similar effects were observed in literature, even for very small amounts of additives [77–79]. Especially the use of bismuth containing compounds was previously suspected to improve densification [80]. One possible reason for this increase is the densification effect caused by the liquid phase during sintering. Theoretically, the liquid phase could have infiltrated pores in the material and thereby increased compaction.

For both additive materials, the resulting sample mechanical properties also increased, far exceeding those obtained for baseline material. Again, this can possibly be attributed to an effect caused by the liquid phase in the material. A decrease in the porosity of the sample leads to less points where stress concentrates and hence higher loads can be sustained. Additionally, the liquid phase might interact with the particles in a mechanical and/or chemical way. Mechanical interlocking between the solidified liquid phase and particles could explain improved properties. Should a chemical connection be made between the ceramic regolith and the additive, this could possibly also improve cohesion and as a result the properties. However, the observed XRD spectra during this research (see Section 4.4) do not indicate a substantial change in chemical composition. Hence, the increase in properties is mostly attributed to mechanical effects.

The properties of bismuth enriched samples exceed those of aluminium enriched samples. It appeared that increasing the weight fraction of bismuth oxide result in an increasing trend for the mechanical properties, whereas increasing the aluminium weight fraction did not seem to result in an increasing trend. One possible explanation for this can be deduced from the thermal behaviour of MGS-1 upon heating (see Figure 4.3). The thermal decomposition of Mg-sulphate (epsomite) results in the release of S_{02}/SO_3 and oxygen [3]. This sulphur dioxide was also observed during gas spectroscopy measurements performed during this research. The created oxygen possibly provides an oxidising environment within the sample mould. Since pure aluminium is highly reactive, it could be hypothesised that the metal oxidises to alumina during sintering. The melting point of alumina far exceeds the sintering

temperatures used, effectively removing the liquid phase. The decomposition of epsomite occurs at temperatures between 825 °C and 1000 °C [40], which indicates that liquid aluminium should be present for some time before possible oxidation can occur. Therefore, some benefits from liquid aluminium are obtained (resulting in the observed improvement), but no continuous improvement is present. In the case of bismuth oxide additives, the liquid phase is not hindered during sintering, resulting in improved properties.

In order to investigate if the improvements observed for the different additives can be attributed to the increase in densification, or depend on the additive, sintering curves can be used. The sintering curves for the stiffness biaxial strength as a function of relative density can be observed in Figure 7.1 and Figure 7.2 respectively. Note, in these plots the stress range correction has been applied and both sieved and unsieved samples are plotted. Trend lines in the figures are calculated for relative densities above 70 %. In the plots an estimate for the uncertainty is also presented. This uncertainty is based on the effect of measured standard deviations in sample physical properties.

If the increase in biaxial strength is directly related to the relative density of the additive, the data points should collapse down to a single line. For the stiffness, this appears to be the case. Taking into account the presented uncertainties, no clear difference between the baseline and the enriched sintered material can be observed.

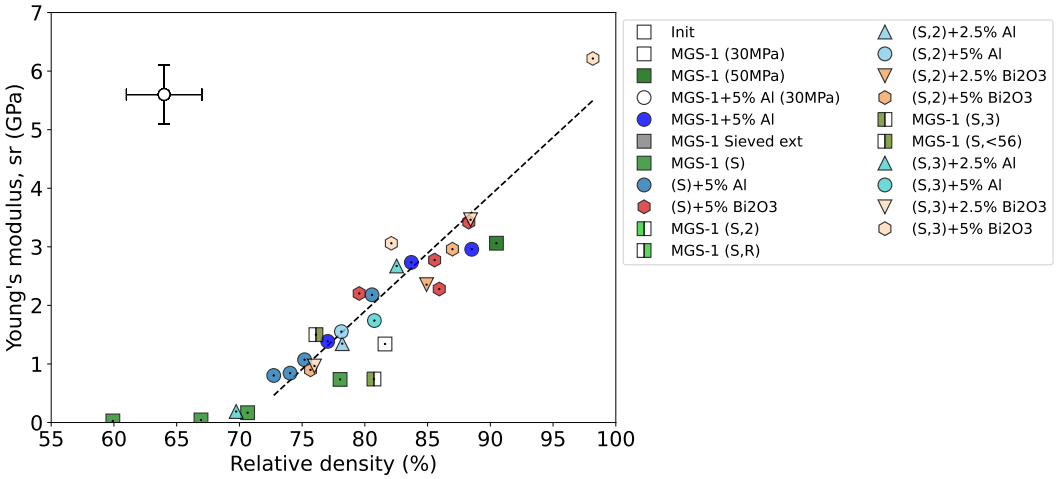

Figure 7.1: *Sintering curve for the Young's modulus of sintered samples as a function of the sample relative density. The dashed line represents the trend for all considered samples. The marker in the top left is an indication of the accuracy in relative density and Young's modulus respectively.*

The biaxial strength sinter curve shows different behaviour, however. In this plot, several lines are drawn in order to illustrate the effect of different material types. Solid lines indicate 5wt% additive samples and dashed lines 2.5wt% samples. For baseline sintered samples (dotted line), the slope of the generally observed trend is lower than that of enriched material. This observation holds for most samples, except some baseline samples made from the smallest particle size sieved material. Therefore, it appears that the increase in strength can be attributed to more than the increase in densification alone.

Comparing the trends for the different weight percentages, it can be seen that the lower additive trend is below that of the higher additive amount, but that the slopes of both lines are similar. For the aluminium additive, both lines almost overlap. The difference is slightly bigger in bismuth oxide enriched samples, but still falls well within the expected uncertainties.

Summarising, it appears that the increase in biaxial strength by using additives is related to more than just an increase in relative density, but no similar conclusion can be drawn for the stiffness. However, additional research is required to make well founded conclusions.

Additionally, the improvement of material properties also seems to affect the mechanical response of the samples. Where most of the samples made from baseline regolith simulant exhibited tough behaviour during testing, samples made from enriched material overwhelmingly exhibited brittle behaviour. Again, mechanical interlocking effects caused by the additive materials could explain this phenomenon.

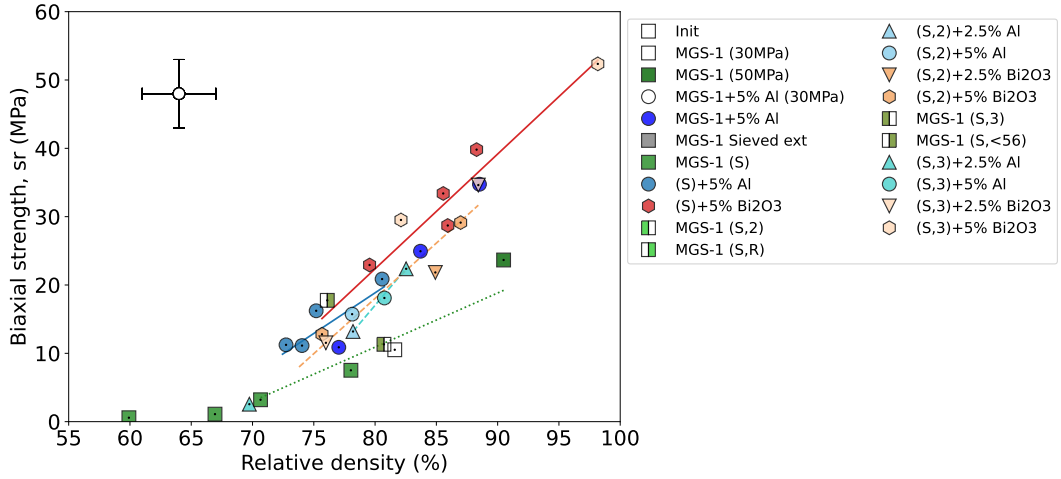

Figure 7.2: *Sintering curve for the biaxial strength of sintered samples as a function of the sample relative density. Lines indicate the generally observed trend for baseline and enriched samples, with solid lines indicating 5wt% samples and the dashed lines representing 2.5wt% samples respectively. The marker in the top left is an indication of the accuracy in relative density and biaxial strength respectively.*

7.5. Performance Compared to Literature

Few research has been performed into sintered Martian regolith simulant. One of the few examples is found by Karl et al. [40]. In their experiments, they used a slightly altered version of the clay containing MGS-1 simulant (MGS-1C) which they call MGS-1C/8. Samples were sintered between 10 minutes and 10 hours, with sintering temperatures ranging between 1130 °C and 1150 °C. Ball-on-three-balls biaxial flexure tests were performed on a subset of data. Their results and those obtained during this research are shown together in Figure 7.3. For comparison, literature data from materials made with Martian regolith simulant by using different additives and amounts are shown [37, 38, 81–84]. Additionally, flexural strength ranges for facing brick and ceramic tiles (green) and engineering brick (blue) are shown.

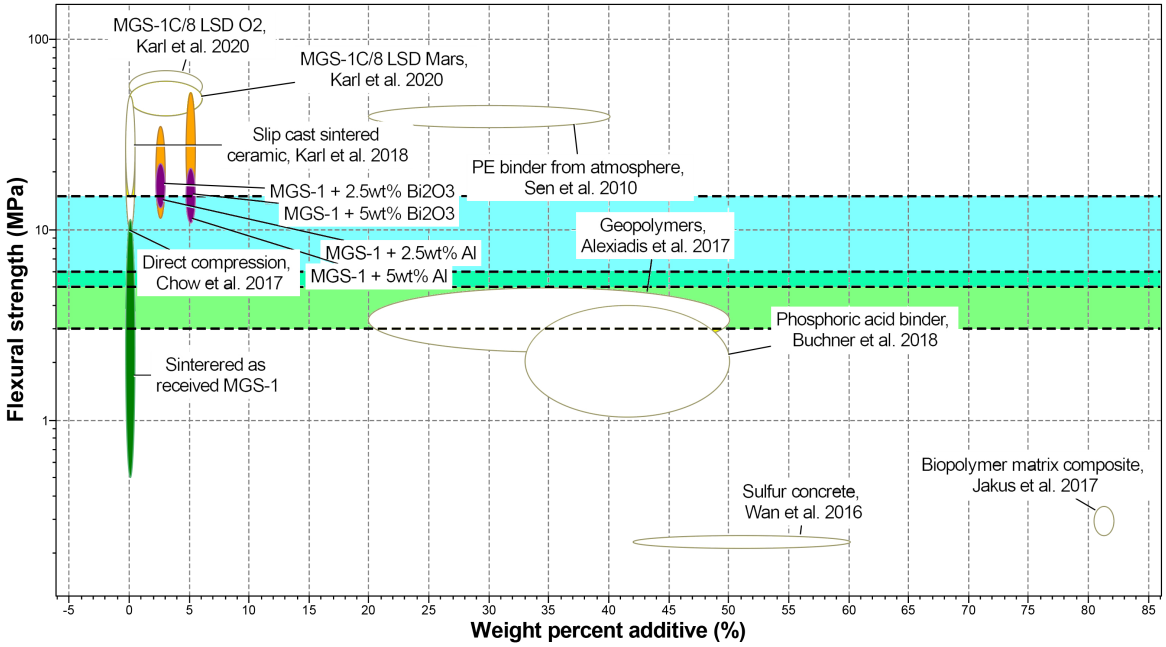

Figure 7.3: *Flexural strength vs required additional material for Martian regolith base materials*

From the comparison it becomes clear that the obtained results in this thesis perform well compared

to literature values. The values obtained by Karl et al. are slightly higher, but so are the used sintering times and temperatures.

Additionally, comparing the strength of tested samples, baseline sintered MGS-1 samples show strength comparable to ceramic terrestrial structural materials, and samples made with additives are equal or better than terrestrial engineering brick.

7.6. Link of Obtained Results to Martian Application

A value of 5wt% was used throughout this thesis for the maximum additive amount. This value was based on findings from Spedding, Nuttall, and Lim on the required shield volume for a sintered lunar habitat radiation shield, see Subsection 2.1.4. It was clearly shown in Figure 7.3 that samples made with 5wt% or lower amounts of additives exhibit highly favourable properties compared to those made without. Since these binder masses can already be transported using current launch platforms (see Figure 2.2), the used additive amounts in this thesis are deemed not unrealistic for actual application.

several different aspects need to be addressed, if the SPS process is to be used on Mars. First of all, the process needs to be scaled up for bigger samples and larger sample sizes, as during this thesis only small disk-shaped specimen were made. Second, the material system needs to be optimised for binder amount and SPS processing parameters. Finally, autonomous production process needs to be developed. Considering the SPS process and the obtained results, it is theorised that the application on site would consist of sintering tile like components for use in infrastructure such as roads or landing pads. This manufacturing process could be integrated in an autonomous production process which involves fusing individual tiles using self-sustaining/combustion joining reactions, similar to those performed by Ferguson, Shafirovich, and Mantovani on sintered Lunar regolith samples [85].

8

Conclusion

The objective of this thesis was to investigate the effect of sintering aids on sintered sample properties of spark plasma sintered MGS-1 Martian regolith simulant, with the aim to determine whether or not the obtained material could be used for structural purposes. In order to meet this objective, several different research questions were formulated. Many samples were sintered and their properties investigated.

Samples were sintered using a variety of SPS machine setting and materials. In general, an improvement in sintering degree was observed for increasing sintering temperatures. Samples made from baseline material sintered at low temperatures were granular and porous, exhibiting a low degree of sintering. Sintering improved with increasing temperature, resulting in densified samples. During sintering, a colour change was observed from brownish-red to grey.

It was found that the sintering pressure and sintering temperature are the most important process parameters impacting the sintered sample results. With increasing sintering pressure and temperature, the densification increases and subsequently the properties. Contrary to expectation, the particle size had very little effect on densification and mechanical properties. No noticeable effect of using different dwell cycles was observed for the two cycles investigated in this research.

For both sintering aids investigated (aluminium and bismuth oxide), the properties of sintered samples improved notably compared to samples made from baseline MGS-1. At higher sintering temperatures, the properties of aluminium doped samples became closer to those obtained for baseline material, whereas bismuth oxide enriched samples still exhibited a notable improvement. However, for both additives, the average improvement decreases with increasing sintering temperature, indicating that most improvement is obtained at lower sintering temperatures. The material behaviour of a sample appears to correlate with the biaxial strength. A transition from tough to brittle material behaviour was observed for a biaxial strength value at around 12 MPa.

Two different weight percentages of additive were investigated, 2.5 and 5wt%. For both weight percentages, the sample properties improved compared to baseline samples. For aluminium enriched samples, the performance of 2.5 and 5wt% doped samples at high sintering temperatures was very similar, whereas at lower temperatures the improvement of 5wt% doped samples was notably better. Bismuth oxide enriched samples showed a clear difference for the two weight percentages. For bismuth oxide, the 5wt% samples always outperformed the 2.5wt% counterparts. Again, the biggest improvement is observed at lower sintering temperatures.

In order to obtain properties similar to terrestrial mortar, it was found that samples need to have a relative density of at least 70%. For baseline MGS-1, this results in minimal sintering temperatures between 1000 °C and 1050 °C. Using additives, this temperature can be significantly lowered. For 5wt% aluminium enriched samples, this relative density is achieved at a sintering temperature of 900 °C. For 2.5wt% this temperature is 950 °C. For bismuth oxide enriched samples, these values are obtained at sintering temperatures above 900 °C irrespective of additive amount. High-end sintered baseline material is comparable to engineering brick, and samples sintered with additives outperform facing and engineering brick. Therefore, sintered Martian regolith simulant can be used for structural applications.

In conclusion, sintered Martian regolith shows great potential for use as a structural material. Minimal amounts of sintering aids can be used to decrease the required sintering temperature and increase sample properties. Therefore, the energy requirement for sintering on Mars can possibly be lowered by using additives. Between the two additives investigated in this research, bismuth oxide shows the most promising results. Using sintering aids possibly makes the application of this process more feasible on Mars in the future.

9

Recommendations

The current research aimed at investigating the effect of additives on the properties of sintered Martian regolith simulant. Throughout this research most focus was placed on comparing the biaxial strength of samples, but a variety of different avenues remain relatively unexplored. These areas could serve as potential research areas in the future and are discussed below.

Increase sample size For most combinations of material type, sintering temperature and sintering pressure, only few samples were sintered. This means that little statistical analysis was possible on the obtained results. Increased sample sizes should provide more insight in the material behaviour and spread of sintered MGS-1 samples.

Improve densification of SPS sintered baseline MGS-1 Throughout this research the maximum sintering temperature used was 1060 °C, but most samples were sintered at a maximum temperature of 1050 °C. At this sintering temperature, the baseline MGS-1 samples did not fully densify. Future research could focus on optimising the sintering profile and parameters in order to increase the densification of MGS-1. Highly densified baseline MGS-1 samples can be used to validate the trends observed during the current research and confirm the conclusions of the sintering curves of Section 7.4.

Determine the improvement mechanism of sintering aids Two different sintering aids were used, that both showed an improvement over the baseline sintered material. However, little research was performed in order to explain why these improvements are observed. Marginal amounts of SEM/EDS were performed, but no well-founded conclusions could be found.

Investigate the effect of sintering aid on other sample properties The mechanical properties of sintered samples were the main metric investigated during this research. However, for actual application on Mars several other material properties should be investigated too. Examples include thermal conductivity to assess thermal isolation properties and impact resistance to evaluate susceptibility to damage.

Assess the effect of other sintering aids The two additives used in this research were chosen specifically to result in a liquid phase during sintering without any chemical reactions taking place. This means that the liquid phase is formed ex-situ, but past research on sintering aids has also produced in-situ additives that react with the base material forming a liquid phase. Potentially, mineral compositions and thermal behaviour upon heating (gas formation, see Figure 4.3) can be used to identify other suited additives.

Assess samples made using alternative sintering methods The SPS process used during this thesis is a pressure-assisted process. Therefore, it is likely that the applied pressure aided any possible liquid phase in penetrating the material and improve densification. It would be interesting to see whether this improvement is also observed in pressure-less sintering methods like HP or alternative pressure-assisted processes like HIP. Alternatively, selective laser sintering might be an interesting technique to investigate given the potential for additive manufacturing.

Bibliography

[1] Michael Sheetz. *Elon Musk: 'Highly confident' SpaceX will land humans on Mars by 2026*. Dec. 2020. URL: https://www.cnbc.com/2020/12/01/elon-musk-highly-confident-spacex-will-land-humans-on-mars-by-2026.html (visited on 04/08/2022).

[2] A. Scott Howe and Brent Sherwood. *Out of This World: The New Field of Space Architecture*. American Institute of Aeronautics and Astronautics, Sept. 2009. ISBN: 978-1-56347-987-8. DOI: 10.2514/4.479878.

[3] Kevin M. Cannon et al. "Mars global simulant MGS-1: A Rocknest-based open standard for basaltic martian regolith simulants". In: *Icarus* 317 (Jan. 2019), pp. 470–478. ISSN: 0019-1035. DOI: 10.1016/J.ICARUS.2018.08.019.

[4] Andrew A. Gonzales et al. "Mars Sample Return using commercial capabilities: Mission architecture overview". In: *IEEE Aerospace Conference Proceedings* (2014). ISSN: 1095323X. DOI: 10.1109/AERO.2014.6836421.

[5] P. Sarrazin et al. "Field deployment of a portable XRD/XRF instrument on Mars analog terrain". In: *Advances in X-ray Analysis* 48 (2005), pp. 194–203.

[6] M. Cabane et al. "Did life exist on Mars? Search for organic and inorganic signatures, one of the goals for "SAM" (sample analysis at Mars)". In: *Advances of Space Research* 33.12 (2004), pp. 2240–2245. DOI: 10.1016/S0273-1177(03)00523-4.

[7] Catherine M. Weitz et al. "Sand Grain Sizes and Shapes in Eolian Bedforms at Gale Crater, Mars". In: *Geophysical Research Letters* 45.18 (Sept. 2018), pp. 9471–9479. ISSN: 00948276. DOI: 10.1029/2018GL078972.

[8] Mohamed N. Rahaman. *Sintering of Ceramics*. CRC Press, July 2013. ISBN: 978-1-4200-0705-3. DOI: 10.1201/B15869.

[9] K. Hadler et al. "A universal framework for Space Resource Utilisation (SRU)". In: *Planetary and Space Science* 182 (Mar. 2020), p. 104811. ISSN: 0032-0633. DOI: 10.1016/j.pss.2019.104811.

[10] Christopher P. Spedding, William J. Nuttall, and Sungwoo Lim. "Energy requirements of a thermally processed ISRU radiation shield for a lunar habitat". In: *Advances in Space Research* 65.11 (June 2020), pp. 2467–2474. ISSN: 18791948. DOI: 10.1016/j.asr.2020.03.015.

[11] Marco Christov. "A Mars heavy transport architecture - Increasing current payload capability to Mars with existing technology". In: *Mars Society Convention*. Boulder, CO: Mars Society, Oct. 2008. URL: http://www.marspapers.org/paper/Christov_2008.pdf.

[12] S. Arunan and R. Satish. "Mars Orbiter Mission spacecraft and its challenges". In: *Current Science* 109.6 (Sept. 2015), pp. 1061–1069. URL: https://doi.org/10.18520%5C%2Fv109%5C%2Fi6%5C%2F1061-1069.

[13] *SpaceX - Falcon 9*. URL: https://www.spacex.com/vehicles/falcon-9/ (visited on 03/30/2022).

[14] *SpaceX - Falcon Heavy*. URL: https://www.spacex.com/vehicles/falcon-heavy/ (visited on 03/30/2022).

[15] B. K. Muirhead et al. "Sample Retrieval Lander Concept for a Potential Mars Sample Return Campaign". In: *Ninth International Conference on Mars*. Pasadena, California, July 2019.

[16] C. D. O'Connell-Cooper et al. "APXS-derived chemistry of the Bagnold dune sands: Comparisons with Gale Crater soils and the global Martian average". In: *Journal of Geophysical Research: Planets* 122.12 (Dec. 2017), pp. 2623–2643. ISSN: 2169-9100. DOI: 10.1002/2017JE005268.

[17] Albert S. Yen et al. "Nickel on Mars: Constraints on meteoritic material at the surface". In: *Journal of Geophysical Research: Planets* 111.E12 (Dec. 2006), pp. 12–23. ISSN: 2156-2202. DOI: 10.1029/2006JE002797.

[18] C. N. Achilles et al. "Mineralogy of an active eolian sediment from the Namib dune, Gale crater, Mars". In: *Journal of Geophysical Research: Planets* 122.11 (Nov. 2017), pp. 2344–2361. ISSN: 21699097. DOI: 10.1002/2017JE005262.

[19] Audouin Dollfus and Marc Deschamps. “Grain-size determination at the surface of Mars”. In: *Icarus* 67.1 (July 1986), pp. 37–50. ISSN: 0019-1035. DOI: 10.1016/0019-1035(86)90172-7.

[20] Richard W. Shorthill et al. “The ”Soil” of mars (viking 1)”. In: *Science* 194.4260 (Oct. 1976), pp. 91–97. ISSN: 00368075. DOI: 10.1126/science.194.4260.91.

[21] C. M. Weitz et al. “Soil grain analyses at Meridiani Planum, Mars”. In: *Journal of Geophysical Research: Planets* 111.E12 (Dec. 2006). ISSN: 01480227. DOI: 10.1029/2005JE002541.

[22] Xiaojia Zeng et al. “JMSS-1: A new Martian soil simulant Planetary science”. In: *Earth, Planets and Space* 67.1 (Dec. 2015), p. 72. ISSN: 18805981. DOI: 10.1186/s40623-015-0248-5.

[23] Henry J. Moore and Bruce M. Jakosky. “Viking landing sites, remote-sensing observations, and physical properties of Martian surface materials”. In: *Icarus* 81.1 (1989), pp. 164–184. ISSN: 0019-1035. DOI: https://doi.org/10.1016/0019-1035(89)90132-2.

[24] Paul Morgan et al. “A Pre-Landing Assessment of Regolith Properties at the InSight Landing Site”. In: *Space Science Reviews* 214 (2018), p. 104. DOI: 10.1007/s11214-018-0537-y.

[25] M. Golombek et al. “Selection of the InSight Landing Site”. In: 211.1-4 (Oct. 2017), pp. 5–95. ISSN: 1572-9672. DOI: 10.1007/s11214-016-0321-9.

[26] Xiangwu Zeng et al. “Geotechnical Properties of JSC-1A Lunar Soil Simulant”. In: *Journal of Aerospace Engineering* 23.2 (Apr. 2010), pp. 111–116. ISSN: 0893-1321. DOI: 10.1061/(ASCE)AS.1943-5525.0000014.

[27] M. Z. Naser. “Extraterrestrial construction materials”. In: *Progress in Materials Science* 105 (Aug. 2019). ISSN: 0079-6425. DOI: 10.1016/j.pmatsci.2019.100577.

[28] Gregory H. Peters et al. “Mojave Mars simulant-Characterization of a new geologic Mars analog”. In: *Icarus* 197.2 (Oct. 2008), pp. 470–479. ISSN: 0019-1035. DOI: 10.1016/j.icarus.2008.05.004.

[29] Mingjing Jiang, Liqing Li, and Yugang Sun. “Properties of TJ-1 Lunar Soil Simulant”. In: *Journal of Aerospace Engineering* 25.3 (July 2012), pp. 463–469. ISSN: 0893-1321. DOI: 10.1061/(asce)as.1943-5525.0000129.

[30] Nisha K. Ramkissoon et al. “New simulants for martian regolith: Controlling iron variability”. In: *Planetary and Space Science* 179 (Dec. 2019), p. 104722. ISSN: 00320633. DOI: 10.1016/j.pss.2019.104722.

[31] Karsten Seiferlin et al. “Simulating Martian regolith in the laboratory”. In: *Planetary and Space Science* 56.15 (Dec. 2008), pp. 2009–2025. ISSN: 0032-0633. DOI: 10.1016/j.pss.2008.09.017.

[32] Carlton C. Allen et al. “JSC MARS-1: A Martian Soil Simulant”. In: *Space 98*. Reston, VA: American Society of Civil Engineers, Apr. 1998, pp. 469–476. ISBN: 9780784403396. DOI: 10.1061/40339(206)54.

[33] Pierre Delage et al. “An Investigation of the Mechanical Properties of Some Martian Regolith Simulants with Respect to the Surface Properties at the InSight Mission Landing Site”. In: *Space Science Reviews* 211.1-4 (Oct. 2017), pp. 191–213. ISSN: 1572-9672. DOI: 10.1007/s11214-017-0339-7.

[34] Athanasios Goulas et al. “Assessing extraterrestrial regolith material simulants for in-situ resource utilisation based 3D printing”. In: *Applied Materials Today* 6 (Mar. 2017), pp. 54–61. ISSN: 2352-9407. DOI: 10.1016/J.APMT.2016.11.004.

[35] Marsha A. Presley and Robert A. Craddock. “Thermal conductivity measurements of particulate materials: 3. Natural samples and mixtures of particle sizes”. In: *Journal of Geophysical Research: Planets* 111.E9 (2006). DOI: 10.1029/2006JE002706.

[36] M. P. Bodiford et al. “Lunar In Situ Materials-Based Habitat Technology Development Efforts at NASA/MSFC”. In: *Earth and Space 2006*. Vol. 2006. American Society of Civil Engineers, 2006, pp. 1–8. ISBN: 0784408300. DOI: 10.1061/40830(188)70.

[37] Lin Wan, Roman Wendner, and Gianluca Cusatis. “A novel material for in situ construction on Mars: experiments and numerical simulations”. In: *Construction and Building Materials* 120 (Sept. 2016), pp. 222–231. ISSN: 0950-0618. DOI: 10.1016/j.conbuildmat.2016.05.046.

[38] S. Sen, S. Carranza, and S. Pillay. “Multifunctional Martian habitat composite material synthesized from in situ resources”. In: *Advances in Space Research* 46.5 (Sept. 2010), pp. 582–592. ISSN: 0273-1177. DOI: 10.1016/j.asr.2010.04.009.

[39] Stephen J Indyk and Haym Benaroya. “A structural assessment of unrefined sintered lunar regolith simulant”. In: *Acta Astronautica* 140 (Nov. 2017), pp. 517–536. ISSN: 0094-5765. DOI: 10.1016/j.actaastro.2017.09.018.

[40] David Karl et al. “Sintering of ceramics for clay in situ resource utilization on Mars”. In: *Open Ceramics* 3 (Sept. 2020). ISSN: 2666-5395. DOI: 10.1016/J.OCERAM.2020.100008.

[41] Suk-Joong L. Kang. *Sintering: densification, grain, growth, and microstructure*. Oxford : Elsevier Butterworth-Heinemann, 2005, 2005.

[42] Ling Bing Kong et al. “Sintering and Densification (I)-Conventional Sintering Technologies”. In: *Transparent Ceramics*. Springer International Publishing, 2015, pp. 291–394. ISBN: 978-3-319-18956-7. DOI: 10.1007/978-3-319-18956-7_5.

[43] Jan Hostaša et al. “Sintering aids, their role and behaviour in the production of transparent ceramics”. In: *Open Ceramics* 7 (Sept. 2021), p. 100137. ISSN: 2666-5395. DOI: 10.1016/J.OCERAM.2021.100137.

[44] Gaida Sedmale et al. “Microstructure and properties of mullite–ZrO2 ceramics with silicon nitride additive prepared by spark plasma sintering”. In: *Ceramics International* 42.3 (Feb. 2016), pp. 3745–3750. ISSN: 0272-8842. DOI: 10.1016/J.CERAMINT.2015.10.112.

[45] Khalil Abdelrazek Khalil. “Advanced Sintering of Nano-Ceramic Materials”. In: *Ceramic Materials - Progress in Modern Ceramics*. IntechOpen, Apr. 2012, pp. 65–82. ISBN: 978-953-51-0476-6. DOI: 10.5772/38287. URL: https://www.intechopen.com/chapters/35038.

[46] W. Chen et al. “Fundamental investigations on the spark plasma sintering/synthesis process: I. Effect of dc pulsing on reactivity”. In: *Materials Science and Engineering A* 394.1 (Mar. 2005), pp. 132–138. ISSN: 0921-5093. DOI: 10.1016/J.MSEA.2004.11.020.

[47] H.U. Kessel and J. Hennicke. “Aspects concerning the super-fast sintering of powder metallic and ceramic materials”. In: *International Ceramic Review* 56.3 (May 2007), pp. 164–166.

[48] Olivier Guillon et al. “Field-Assisted Sintering Technology/Spark Plasma Sintering: Mechanisms, Materials, and Technology Developments”. In: *Advanced Engineering Materials* 16.7 (July 2014), pp. 830–849. ISSN: 1527-2648. DOI: 10.1002/ADEM.201300409.

[49] Michael Stuer, Paul Bowen, and Zhe Zhao. “Spark Plasma Sintering of Ceramics: From Modeling to Practice”. In: *Ceramics 2020, Vol. 3, Pages 476-493* 3.4 (Nov. 2020), pp. 476–493. ISSN: 2571-6131. DOI: 10.3390/CERAMICS3040039.

[50] W. R. Matizamhuka. “Spark plasma sintering (SPS) - An advanced sintering technique for structural nanocomposite materials”. In: *Journal of the Southern African Institute of Mining and Metallurgy* 116.12 (Dec. 2016), pp. 1171–1180. ISSN: 2225-6253. DOI: 10.17159/2411-9717/2016/V116N12A12.

[51] Z. A. Munir, U. Anselmi-Tamburini, and M. Ohyanagi. “The effect of electric field and pressure on the synthesis and consolidation of materials: A review of the spark plasma sintering method”. In: *Journal of Materials Science 2006 41:3* 41.3 (Feb. 2006), pp. 763–777. ISSN: 1573-4803. DOI: 10.1007/S10853-006-6555-2.

[52] *C1161-18 Strength of Advanced Ceramics at Ambient Temperature*. West Conshohocken, PA: ASTM International, 2003. DOI: 10.1520/C0033-03.

[53] T. Fett and G. Rizzi. *3-balls-on-3-balls test for ceramic disks: a finite element study*. Tech. rep. 2004. DOI: 10.5445/IR/270059321. URL: https://publikationen.bibliothek.kit.edu/270059321.

[54] M. N. Giovan and George Sines. “Strength of a Ceramic at High Temperatures Under Biaxial and Uniaxial Tension”. In: *Journal of the American Ceramic Society* 64.2 (Feb. 1981), pp. 68–73. ISSN: 1551-2916. DOI: 10.1111/J.1151-2916.1981.TB09578.X.

[55] H. Fessler and D. C. Fricker. “A Theoretical Analysis of the Ring□On□Ring Loading Disk Test”. In: *Journal of the American Ceramic Society* 67.9 (1984), pp. 582–588. ISSN: 1551-2916. DOI: 10.1111/J.1151-2916.1984.TB19598.X.

[56] *C1499-03 Standard Test Method for Monotonic Equibiaxial Flexural Strength of Advanced Ceramics at Ambient Temperature*. West Conshohocken, PA: ASTM International, 2017. DOI: 10.1520/C1499-03.

[57] D. J. Godfrey and S. John. “Disc flexure tests for the evaluation of ceramic strength”. In: *Proceedings 2nd International Conference of Ceramic Materials and Components for Engines*. Verlag Deutsche Keramische Gesellschaft. Lübeck-Travemünde, Apr. 1986, pp. 657–665. ISBN: 3-925543-01-5.

[58] Andreas Börger, Peter Supancic, and Robert Danzer. “The ball on three balls test for strength testing of brittle discs: Part II: analysis of possible errors in the strength determination”. In: *Journal of the European Ceramic Society* 24.10-11 (Sept. 2004), pp. 2917–2928. ISSN: 0955-2219. DOI: 10.1016/J.JEURCERAMSOC.2003.10.035.

[59] D. K. Shetty et al. “Biaxial Flexure Test for Ceramics”. In: *American Ceramic Society Bulletin* 59.12 (Dec. 1980). URL: https://www.researchgate.net/publication/236381914_Biaxial_Flexure_Test_for_Ceramics.

[60] Seung-Hyun Chae et al. “Verification of ball-on-ring test using finite element analysis”. In: *2010 12th IEEE Intersociety Conference on Thermal and Thermomechanical Phenomena in Electronic Systems*. 2010, pp. 1–6. DOI: 10.1109/ITHERM.2010.5501307.

[61] Adrianna E. Lupercio et al. “Ball-on-ring test validation for equibiaxial flexural strength testing of engineered ceramics”. In: *International Journal of Ceramic Engineering & Science* 3.3 (May 2021), pp. 128–139. ISSN: 2578-3270. DOI: 10.1002/ces2.10085.

[62] Exolith Lab. *MGS-1 Mars Global Simulant| Fact Sheet*. Tech. rep. Feb. 2022. URL: https://exolithsimulants.com/products/mgs-1-mars-global-simulant (visited on 04/08/2022).

[63] F. Ruess, J. Schaenzlin, and H. Benaroya. “Structural design of a lunar habitat”. In: *Journal of Aerospace Engineering* 19.3 (July 2006), pp. 133–157. ISSN: 08931321. DOI: 10.1061/(ASCE)0893-1321(2006)19:3(133).

[64] Gye-Chun Cho, Jake Dodds, and J. Carlos Santamarina. “Particle Shape Effects on Packing Density, Stiffness, and Strength: Natural and Crushed Sands”. In: *Journal of Geotechnical and Geoenvironmental Engineering* 132.5 (May 2006), pp. 591–602. ISSN: 1090-0241. DOI: 10.1061/(ASCE)1090-0241(2006)132:5(591).

[65] W. C. Krumbein and L. L. Sloss. *Stratigraphy and sedimentation*. Second edition. San Francisco: W.H. Freeman, 1963.

[66] Ugur Ulusoy. “Quantifying of particle shape differences of differently milled barite using a novel technique: Dynamic image analysis”. In: *Materialia* 8 (Dec. 2019). ISSN: 25891529. DOI: 10.1016/J.MTLA.2019.100434.

[67] A. F. Kirstein and R. M. Woolley. “Symmetrical Bending of Thin Circular Elastic Plates on Equally Spaced Point Supports”. In: *Journal of Research of the National Bureau of Standards* 71C.1 (1967).

[68] S. M. Hu. “Critical stress in silicon brittle fracture, and effect of ion implantation and other surface treatments”. In: *Journal of Applied Physics* 53.5 (1982), pp. 3576–3580. DOI: 10.1063/1.331137.

[69] Gijsbertus de With and Harrie H. M. Wagemans. “Ball-on-Ring Test Revisited”. In: *Journal of the American Ceramic Society* 72.8 (1989), pp. 1538–1541. ISSN: 1551-2916. DOI: 10.1111/J.1151-2916.1989.TB07702.X.

[70] H. M. Westergaard. “Stresses in concrete pavements computed by theoretical analysis”. In: *Public Roads* 7.2 (Apr. 1926), pp. 25–35. ISSN: 0033-3735.

[71] A. F. Kirstein and R. M. Woolley. “Deflection of Thin Circular Elastic Plates Under Symmetrically Distributed Loading”. In: *Journal of research of the National Bureau of Standards - C. Engineering and Instrumentation* 72C.1 (1968). URL: https://nvlpubs.nist.gov/nistpubs/jres/72C/jresv72Cn1p21_A1b.pdf.

[72] D. K. Shetty et al. “A Biaxial□Flexure Test for Evaluating Ceramic Strengths”. In: *Journal of the American Ceramic Society* 66.1 (1983), pp. 36–42. ISSN: 1551-2916. DOI: 10.1111/J.1151-2916.1983.TB09964.X.

[73] Eugene C. Robertson. “Thermal properties of rocks”. In: *Open-File Report 88-441* (1988). ISSN: 2331-1258. DOI: 10.3133/OFR88441.

[74] David Karl et al. “Clay in situ resource utilization with Mars global simulant slurries for additive manufacturing and traditional shaping of unfired green bodies”. In: *Acta Astronautica* 174 (Sept. 2020), pp. 241–253. ISSN: 0094-5765. DOI: 10.1016/j.actaastro.2020.04.064.

[75] Xiang Zhang et al. “Spark plasma sintering of a lunar regolith simulant: effects of parameters on microstructure evolution, phase transformation, and mechanical properties”. In: *Ceramics International* 47.4 (Feb. 2021), pp. 5209–5220. ISSN: 0272-8842. DOI: 10.1016/J.CERAMINT.2020.10.100.

[76] Onur Eser and Semra Kurama. “A comparison of sintering techniques using different particle sized β-SiAlON powders”. In: *Journal of the European Ceramic Society* 32.7 (June 2012), pp. 1343–1347. ISSN: 0955-2219. DOI: 10.1016/J.JEURCERAMSOC.2011.08.026.

[77] K. A. Khor, L. G. Yu, and Y. Murakoshi. “Spark plasma sintering of Sm2O3-doped aluminum nitride”. In: *Journal of the European Ceramic Society* 25.7 (May 2005), pp. 1057–1065. ISSN: 0955-2219. DOI: 10.1016/J.JEURCERAMSOC.2003.12.020.

[78] Liangliang Yang et al. “Study of the Comparative Effect of Sintering Methods and Sintering Additives on the Microstructure and Performance of Si3N4 Ceramic”. In: *Materials* 12.13 (July 2019), p. 2142. DOI: 10.3390/MA12132142.

[79] Seung Kyu Choi et al. “Densification behavior of ZrB2 with Co–WC as additives”. In: *Journal of the Ceramic Society of Japan* 122.1423 (Mar. 2014), pp. 198–203. ISSN: 1882-0743. DOI: 10.2109/JCERSJ2.122.198.

[80] Petre Badica et al. “Composites of MgB2 with Bi2O3, Bi, Sb 2O3, or Sb obtained by ex-situ spark plasma sintering”. In: *Japanese Journal of Applied Physics* 51.11S (Nov. 2012), 11PG13. ISSN: 0021-4922. DOI: 10.1143/JJAP.51.11PG13.

[81] Alessio Alexiadis, Federico Alberini, and Marit E. Meyer. “Geopolymers from lunar and Martian soil simulants”. In: *Advances in Space Research* 59.1 (Jan. 2017), pp. 490–495. ISSN: 1879-1948. DOI: 10.1016/j.asr.2016.10.003.

[82] Christoph Buchner et al. “A new planetary structure fabrication process using phosphoric acid”. In: *Acta Astronautica* 143 (Feb. 2018), pp. 272–284. ISSN: 0094-5765. DOI: 10.1016/J.ACTAASTRO.2017.11.045.

[83] Adam E. Jakus et al. “Robust and Elastic Lunar and Martian Structures from 3D-Printed Regolith Inks”. In: *Scientific Reports 2017 7:1* 7.1 (Mar. 2017), pp. 1–8. ISSN: 2045-2322. DOI: 10.1038/srep44931.

[84] David Karl et al. “Towards the colonization of Mars by in-situ resource utilization: Slip cast ceramics from Martian soil simulant”. In: *PLOS ONE* 13.10 (Oct. 2018), pp. 1–11. DOI: 10.1371/JOURNAL.PONE.0204025. URL: https://journals.plos.org/plosone/article?id=10.1371/journal.pone.0204025.

[85] Robert E. Ferguson, Evgeny Shafirovich, and James G. Mantovani. “Combustion Joining of Regolith Tiles for In Situ Fabrication of Launch/Landing Pads on the Moon and Mars”. In: *Earth and Space 2018*. Reston, VA: American Society of Civil Engineers (ASCE), Nov. 2018, pp. 281–288. DOI: 10.1061/9780784481899.028.

[86] Sebastian Spintzyk et al. “Biaxial flexural strength of zirconia: A round robin test with 12 laboratories”. In: *Dental Materials* 37.2 (Feb. 2021), pp. 284–295. ISSN: 0109-5641. DOI: 10.1016/j.dental.2020.11.016.

[87] K. O. Kese, Z. C. Li, and B. Bergman. “Method to account for true contact area in soda-lime glass during nanoindentation with the Berkovich tip”. In: *Materials Science and Engineering: A* 404.1-2 (Sept. 2005), pp. 1–8. ISSN: 0921-5093. DOI: 10.1016/J.MSEA.2005.06.006.

[88] Martin J. Meyland et al. “An experimental investigation of the flexural strength of soda–lime–silica glass at high loading rates”. In: *Glass Structures and Engineering* 4.2 (July 2019), pp. 175–183. ISSN: 2363-5150. DOI: 10.1007/S40940-018-0089-2/TABLES/4.

A

Sintered and Reference Sample Data

This appendix contains several data tables of sintered and reference samples. First, the data for sintered samples is presented. Next, the data for reference samples is shown. This reference data is split for the two different materials: mortar and soda-lime glass.

A.1. Sintering Sample Data

In this section the different overview tables for all sintered samples made during the course of this thesis are presented. First, the sintering parameters used for all sintered samples is shown in Table A.1. The reported particle sizes either correspond to that reported by Exolith Lab, or to the sieve size used to sieve the material. Note that the heating rate was kept constant at 50 °C min^{-1} for all samples. Table A.2 gives an overview of the physical properties of all samples, as measured by callipers for all dimensions. Finally, Table A.3 gives an overview of the mechanical properties for all sintered samples. In this table, the maximum sustained load is also included.

Table A.1: *Sintering parameters for all sintered samples*

Sample name	Sample Descr.	Particle size [µm]	Pressure [MPa]	Temp [°C]	Dwell cycle
Base_108001	P1	0.04-600	30	800	10 min pressure, 15 min temperature
Base_109001	P2	0.04-600	30	900	10 min pressure, 15 min temperature
Base_168001	P3	0.04-600	50	800	10 min pressure, 15 min temperature
Base_169001	P4	0.04-600	50	900	10 min pressure, 15 min temperature
Base_1010601	P5	0.04-600	30	1060	10 min pressure, 15 min temperature
Base_1610601	P6	0.04-600	50	1060	10 min pressure, 15 min temperature
Init_001	P7	0.04-600	50	1060	10 min pressure, 15 min temperature
Init_002	P8	0.04-600	50	1060	10 min pressure, 15 min temperature
POC_107001	A1	0.04-600	30	700	10 min pressure, 15 min temperature
POC_108001	A2	0.04-600	30	800	10 min pressure, 15 min temperature
POC_109001	A3	0.04-600	30	900	10 min pressure, 15 min temperature
POC_167001	A4	0.04-600	50	700	10 min pressure, 15 min temperature
POC_168001	A5	0.04-600	50	800	10 min pressure, 15 min temperature
POC_169001	A6	0.04-600	50	900	10 min pressure, 15 min temperature
POC_1610001	A7	0.04-600	50	1000	10 min pressure, 15 min temperature
POC_1610601	A8	0.04-600	50	1060	10 min pressure, 15 min temperature
Sieved_1610601	P9	<315	50	1060	10 min pressure, 15 min temperature
Sieved_1610602	P10	<315	50	1060	10 min pressure, 15 min temperature
Base_S_169001	P11	56-150	50	900	10 min pressure, 15 min temperature
Base_S_169501	P12	56-150	50	950	10 min pressure, 15 min temperature
Base_S_1610001	P13	56-150	50	1000	10 min pressure, 15 min temperature
Base_S_1610501	P14	56-150	50	1050	10 min pressure, 15 min temperature
POC_S_169001	A9	56-150	50	900	10 min pressure, 15 min temperature
POC_S_169501	A10	56-150	50	950	10 min pressure, 15 min temperature
POC_S_1610001	A11	56-150	50	1000	10 min pressure, 15 min temperature
POC_S_1610501	A12	56-150	50	1050	10 min pressure, 15 min temperature
POC_B_S_169001	B1	56-150	50	900	10 min pressure, 15 min temperature
POC_B_S_169501	B2	56-150	50	950	10 min pressure, 15 min temperature
POC_B_S_1610001	B3	56-150	50	1000	10 min pressure, 15 min temperature
POC_B_S_1610501	B4	56-150	50	1050	10 min pressure, 15 min temperature
Base_S_169002	P15	56-150	50	900	10 min pressure, 15 min temperature
Base_S_1610502	P16	56-150	50	1050	10 min pressure, 15 min temperature
Base_R_169001	P17	56-150	50	900	15 min pressure, 10 min temperature
Base_R_1610501	P18	56-150	50	1050	15 min pressure, 10 min temperature
POC_S_25_169001	A13	56-150	50	900	10 min pressure, 15 min temperature
POC_S_25_1610501	A14	56-150	50	1050	10 min pressure, 15 min temperature

POC_S_5_169001	A15	56-150	50	900	10 min pressure, 15 min temperature
POC_S_5_1610501	A16	56-150	50	1050	10 min pressure, 15 min temperature
POC_B_S_25_169001	B5	56-150	50	900	10 min pressure, 15 min temperature
POC_B_S_25_1610501	B6	56-150	50	1050	10 min pressure, 15 min temperature
POC_B_S_5_169001	B7	56-150	50	900	10 min pressure, 15 min temperature
POC_B_S_5_1610501	B8	56-150	50	1050	10 min pressure, 15 min temperature
Base_S_169003	P19	56-150	50	900	10 min pressure, 15 min temperature
Base_S_1610503	P20	56-150	50	1050	10 min pressure, 15 min temperature
Sieved_56_169001	P21	<56	50	900	10 min pressure, 15 min temperature
Sieved_56_1610501	P22	<56	50	1050	10 min pressure, 15 min temperature
POC_S_25_169002	A17	56-150	50	900	10 min pressure, 15 min temperature
POC_S_25_1610502	A18	56-150	50	1050	10 min pressure, 15 min temperature
POC_S_5_169002	A19	56-150	50	900	10 min pressure, 15 min temperature
POC_S_5_1610502	A20	56-150	50	1050	10 min pressure, 15 min temperature
POC_B_S_25_169002	B9	56-150	50	900	10 min pressure, 15 min temperature
POC_B_S_25_1610502	B10	56-150	50	1050	10 min pressure, 15 min temperature
POC_B_S_5_169002	B11	56-150	50	900	10 min pressure, 15 min temperature
POC_B_S_5_1610502	B12	56-150	50	1050	10 min pressure, 15 min temperature

Table A.2: *Physical properties for all sintered samples*

Sample name	**Sample Descr.**	**Mass [g]**	**Average height [mm]**	**Height STD (n=5)**	**Average diameter [mm]**	**Diameter STD (n=5)**	**Theoretical density [g cm^{-3}]**	**Relative density [%]**
MMS	MMS	3.3673	3.9600	0.0063	20.2600	0.1088	3.0000	87.92
Base_108001	P1	3.3181	5.4080	0.0204	20.5260	0.0174	2.9900	62.01
Base_109001	P2	3.4307	5.3980	0.0098	20.5020	0.0852	2.9900	64.39
Base_168001	P3	3.3452	5.1520	0.0483	20.5540	0.0265	2.9900	65.45
Base_169001	P4	3.4307	5.2900	0.0623	20.5660	0.0215	2.9900	65.29
Base_1010601	P5	3.3308	4.4680	0.0098	20.3360	0.0692	2.9900	76.76
Base_1610601	P6	3.4110	3.8580	0.0040	20.3980	0.0954	2.9900	90.49
Init_001	P7	3.4097	4.3660	0.0242	20.3060	0.0531	2.9900	80.66
Init_002	P8	3.0599	3.8940	0.0233	20.2500	0.0984	2.9900	81.60
POC_107001	A1	3.2433	5.4480	0.0117	20.4300	0.0506	2.9724	61.10
POC_108001	A2	3.3152	5.1820	0.0075	20.4840	0.0653	2.9724	65.31
POC_109001	A3	3.2275	4.8980	0.0040	20.4280	0.0531	2.9724	67.64
POC_167001	A4	3.1871	4.5600	0.0000	20.3920	0.0621	2.9724	72.00
POC_168001	A5	3.4095	5.0260	0.0265	20.5500	0.0610	2.9724	68.81
POC_169001	A6	3.4102	4.5600	0.0000	20.3920	0.0621	2.9724	77.04
POC_1610001	A7	3.4921	4.3060	0.0080	20.3720	0.0417	2.9724	83.71
POC_1610601	A8	3.4672	4.0580	0.0040	20.3340	0.0287	2.9724	88.52
Sieved_1610601	P9	3.3871	4.5240	0.0080	20.3000	0.0540	2.9900	77.37
Sieved_1610602	P10	3.2125	4.6700	0.0434	20.0380	0.1839	2.9900	72.96
Base_S_169001	P11	2.8009	4.6940	0.0225	20.5940	0.0320	2.9900	59.91
Base_S_169501	P12	3.4472	5.1940	0.0163	20.5480	0.0652	2.9900	66.94
Base_S_1610001	P13	3.1205	4.7560	0.0049	19.8860	0.2023	2.9900	70.65
Base_S_1610501	P14	3.4371	4.5440	0.0102	20.3180	0.0574	2.9900	78.03
POC_S_169001	A9	3.4690	4.8340	0.0136	20.5580	0.0402	2.9724	72.73
POC_S_169501	A10	3.4628	4.8500	0.0089	20.3240	0.0866	2.9724	74.04
POC_S_1610001	A11	3.3855	4.7680	0.0214	20.1120	0.0809	2.9724	75.19
POC_S_1610501	A12	3.4485	4.4480	0.0075	20.3020	0.0387	2.9724	80.57
POC_B_S_169001	B1	3.5886	4.5000	0.0303	20.5420	0.0248	3.0249	79.55
POC_B_S_169501	B2	3.5091	4.2000	0.0127	20.2740	0.0377	3.0249	85.56
POC_B_S_1610001	B3	3.4748	4.0180	0.0214	20.3060	0.0356	3.0249	88.28
POC_B_S_1610501	B4	3.4870	4.1360	0.0120	20.3220	0.0496	3.0249	85.93
Base_S_169002	P15	2.7805	4.5860	0.0418	20.5260	0.0484	2.9900	61.28
Base_S_1610502	P16	3.2238	4.5700	0.0110	20.5660	0.0683	2.9900	71.02
Base_R_169001	P17	3.4069	5.0120	0.0271	20.5220	0.0183	2.9900	68.73
Base_R_1610501	P18	3.3881	4.3060	0.0102	20.4380	0.0232	2.9900	80.21
POC_S_25_169001	A13	3.0391	4.9360	0.0206	20.0420	0.2361	2.9811	65.47
POC_S_25_1610501	A14	3.4718	4.6160	0.0102	20.2680	0.0293	2.9811	78.20
POC_S_5_169001	A15	3.1966	4.8340	0.0215	20.3940	0.2646	2.9724	68.11
POC_S_5_1610501	A16	3.3639	4.4960	0.0049	20.2540	0.0476	2.9724	78.13
POC_B_S_25_169001	B5	3.3780	4.7220	0.0098	20.2600	0.1170	3.0070	73.80
POC_B_S_25_1610501	B6	3.4114	4.1060	0.0080	20.3540	0.0326	3.0070	84.92
POC_B_S_5_169001	B7	3.4430	4.6560	0.0102	20.2820	0.0504	3.0249	75.67
POC_B_S_5_1610501	B8	3.4474	4.0460	0.0273	20.3060	0.0320	3.0249	86.98

Base_S_169003	P19	3.4248	5.2460	0.0163	20.5660	0.0174	2.9900	65.73
Base_S_1610503	P20	3.4539	4.3980	0.0117	20.3540	0.0418	2.9900	80.72
Sieved_56_169001	P21	2.8074	4.5120	0.0240	20.4900	0.1506	2.9900	63.11
Sieved_56_1610501	P22	3.3242	4.5300	0.0245	20.2640	0.1031	2.9900	76.10
POC_S_25_169002	A17	3.2164	4.6880	0.0354	20.4980	0.0075	2.9811	69.74
POC_S_25_1610502	A18	3.5373	4.3840	0.0344	20.4340	0.0273	2.9811	82.53
POC_S_5_169002	A19	3.5671	5.0060	0.0196	20.5260	0.0287	2.9724	72.45
POC_S_5_1610502	A20	3.4651	4.4460	0.0344	20.3320	0.0319	2.9724	80.76
POC_B_S_25_169002	B9	3.5848	4.7460	0.0508	20.5160	0.0206	3.0070	75.99
POC_B_S_25_1610502	B10	3.4687	3.9960	0.0102	20.3880	0.0279	3.0070	88.42
POC_B_S_5_169002	B11	3.5262	4.3080	0.0040	20.4840	0.0242	3.0249	82.11
POC_B_S_5_1610502	B12	3.4555	3.5560	0.0186	20.4120	0.0183	3.0249	98.17

Table A.3: *Mechanical properties for all sintered samples*

Sample name	**Sample Descr.**	F_{max} **[N]**	E **[GPa]**	σ **[MPa]**	E_{sr} **[GPa]**	σ_{sr} **[MPa]**	**Material behaviour**	**Fracture pattern**
Init_001	P1	102.65	0.8092	7.362	-	-	Tough	-
Init_002	P2	111.19	1.3837	10.526	1.341	10.523	Tough	-
Base_108001	P3	8.07	0.0191	0.339	-	-	Tough	3
Base_109001	P4	11.67	0.0425	0.496	-	-	Tough	3
Base_168001	P5	15.07	0.0330	0.710	-	-	Tough	3
Base_169001	P6	15.75	0.0268	0.693	-	-	Tough	4
Base_1010601	P7	88.48	0.7075	6.005	-	-	Tough	4
Base_1610601	P8	244.75	3.7525	23.709	3.061	23.658	Brittle	3
POC_107001	A1	9.99	0.0349	0.416	-	-	Tough	3
POC_108001	A2	24.09	0.0786	1.129	-	-	Tough	3
POC_109001	A3	44.55	0.1125	2.380	-	-	Tough	3
POC_167001	A4	28.54	0.1359	1.831	-	-	Tough	3
POC_168001	A5	40.58	0.1271	2.045	-	-	Tough	4
POC_169001	A6	168.34	1.4379	10.884	1.385	10.879	Tough	4
POC_1610001	A7	336.55	3.1550	24.982	2.733	24.939	Brittle	3
POC_1610601	A8	407.81	5.5934	35.015	2.958	34.743	Brittle	3
Sieved_1610601	P9	122.91	0.7672	8.074	-	-	Tough	3
Sieved_1610602	P10	86.44	0.5583	5.277	-	-	Tough	4
Base_S_169001	P11	9.78	0.0270	0.578	-	-	Tough	3
Base_S_169501	P12	23.84	0.0440	1.098	-	-	Tough	3
Base_S_1610001	P13	55.48	0.1678	3.207	-	-	Tough	3
Base_S_1610501	P14	115.62	0.7363	7.516	-	-	Tough	3
POC_S_169001	A9	202.39	0.8726	11.257	0.803	11.241	Brittle	4
POC_S_169501	A10	201.48	0.8590	11.138	0.842	11.135	Brittle	4
POC_S_1610001	A11	281.83	1.1636	16.251	1.072	16.228	Brittle	3
POC_S_1610501	A12	304.56	2.3514	20.887	2.181	20.867	Brittle	4
POC_B_S_169001	B1	345.24	3.1470	23.027	2.204	22.925	Brittle	3
POC_B_S_169501	B2	425.73	4.2120	33.581	2.774	33.395	Brittle	3
POC_B_S_1610001	B3	456.15	6.6720	40.131	3.421	39.810	Brittle	3
POC_B_S_1610501	B4	353.07	3.3822	28.864	2.280	28.707	Brittle	3
Base_S_169002	P15	11.10	0.0254	0.691	-	-	Tough	4
Base_S_1610502	P16	91.11	0.4142	5.800	-	-	Tough	3
Base_R_169001	P17	18.38	0.0628	0.934	-	-	Tough	4
Base_R_1610501	P18	77.58	0.6050	5.743	-	-	Tough	4
POC_S_25_169001	A13	31.98	0.0794	1.682	-	-	Tough	3
POC_S_25_1610501	A14	210.63	1.4105	13.201	1.346	13.192	Tough	4
POC_S_5_169001	A15	55.17	0.1197	3.031	-	-	Tough	4
POC_S_5_1610501	A16	235.67	1.4525	15.714	1.552	15.728	Brittle	4
POC_B_S_25_169001	B5	151.71	0.7024	8.958	-	-	Tough	3
POC_B_S_25_1610501	B6	262.79	3.2120	21.914	2.354	21.835	Brittle	3
POC_B_S_5_169001	B7	209.76	1.1522	12.841	0.899	12.791	Brittle	4
POC_B_S_5_1610501	B8	338.55	4.4144	29.267	2.960	29.130	Brittle	4
Base_S_169003	P19	29.13	0.0640	1.315	-	-	Tough	3
Base_S_1610503	P20	161.99	0.8181	11.338	0.743	11.320	Tough	4
Sieved_56_169001	P21	41.00	0.1852	2.692	-	-	Tough	4
Sieved_56_1610501	P22	271.53	1.5678	17.763	1.501	17.752	Brittle	4
POC_S_25_169002	A17	42.67	0.1880	2.556	-	-	Tough	3
POC_S_25_1610502	A18	315.09	3.0353	22.404	2.672	22.371	Brittle	4
POC_S_5_169002	A19	148.03	0.5488	7.555	-	-	Tough	3
POC_S_5_1610502	A20	264.25	1.8771	18.119	1.741	18.100	Brittle	4

POC_B_S_25_169002	B9	198.04	1.1298	11.563	0.964	11.537	Tough	3
POC_B_S_25_1610502	B10	390.90	4.9733	34.771	3.463	34.621	Brittle	4
POC_B_S_5_169002	B11	399.46	3.6166	29.579	3.060	29.517	Brittle	3
POC_B_S_5_1610502	B12	446.49	10.2223	52.625	6.215	52.358	Brittle	4

A.2. Reference Sample Data

In this section the reference sample data is presented. First, the zirconia disk reference data is presented, followed by the mortar reference sample data. Finally, data for the soda-lime glass reference samples is shown.

A.2.1. Zirconia Reference Data

The data for the zirconia reference samples is shown below. Table A.4 lists the physical properties and Table A.5 the mechanical.

Table A.4: *Physical properties for soda-lime glass reference samples*

Sample name	Sample Descr.	Mass [g]	Average height [mm]	Height STD (n=5)	Average diameter [mm]	Diameter STD (n=5)	Theoretical density [g cm^{-3}]	Relative density [%]
ZrO2_val_1	Zval1	3.5224	2.0000	0.0000	20.0280	0.0098	5.6800	98.50
ZrO2_val_2	Zval2	3.5230	2.0000	0.0000	20.0280	0.0098	5.6800	98.48

Table A.5: *Mechanical properties for soda-lime reference samples*

Sample name	Sample Descr.	F_{max} [N]	E [GPa]	σ [MPa]	E_{sr} [GPa]	σ_{sr} [MPa]	Material behaviour	Fracture pattern
ZrO2_val_1	Zval1	1497.74	563.1194	696.728	-	-	Brittle	3
ZrO2_val_2	Zval2	1508.59	92.8828	695.104	-	-	Brittle	3

A.2.2. Mortar Reference Data

Table A.6 list the physical properties of the mortar reference samples. All measurements were taken using callipers. A value of 2.4 g cm^{-3} was assumed for the theoretical density. Table A.7 lists the mechanical properties of the mortar reference samples. Since these samples were aimed at establishing a reference strength, no stress range correction had been applied.

Table A.6: *Physical properties for mortar reference samples*

Sample name	Sample Descr.	Mass [g]	Average height [mm]	Height STD (n=5)	Average diameter [mm]	Diameter STD (n=5)	Theoretical density [g cm^{-3}]	Relative density [%]
Mor_M04S01	M1	1.7914	3.2460	0.1023	20.2820	0.0571	2.4000	71.17
Mor_M04S02	M2	2.3330	4.2540	0.2162	20.3480	0.1123	2.4000	70.27
Mor_M04S03	M3	3.7485	6.3620	0.0691	20.1620	0.1908	2.4000	76.89
Mor_M04S04	M4	2.2205	4.0060	0.1073	20.3600	0.1584	2.4000	70.94
Mor_M07S01	M5	3.0461	4.8540	0.1129	20.4120	0.0581	2.4000	79.90
Mor_M07S02	M6	2.7146	4.3300	0.0865	20.2880	0.0945	2.4000	80.81
Mor_M07S03	M7	2.6887	4.1640	0.0163	20.2620	0.1169	2.4000	83.44
Mor_M07S04	M8	2.7001	4.1920	0.0040	20.2340	0.1740	2.4000	83.46
Mor_M07S05	M9	2.6562	4.2140	0.0196	20.3500	0.1501	2.4000	80.75
Mor_M07S06	M10	2.6125	4.3540	0.0508	19.9100	0.3694	2.4000	80.30
Mor_M08S01	M11	2.9391	4.9900	0.0261	20.5540	0.0755	2.4000	73.96
Mor_M08S02	M12	2.9233	5.0080	0.1038	20.5560	0.1035	2.4000	73.29
Mor_M08S03	M13	2.6294	4.4800	0.0603	20.3180	0.0842	2.4000	75.43
Mor_M08S04	M14	2.7561	4.6040	0.0929	20.3580	0.0852	2.4000	76.63
Mor_M08S05	M15	2.6831	4.5140	0.0546	20.3060	0.1007	2.4000	76.48
Mor_M09S01	M16	2.9911	4.9720	0.0426	20.4940	0.0674	2.4000	75.99
Mor_M09S02	M17	2.6022	4.2980	0.0117	20.2560	0.2074	2.4000	78.28

Mor_M09S03	M18	2.8933	4.7180	0.0256	20.3160	0.1508	2.4000	78.82
Mor_M09S04	M19	2.5702	4.2260	0.0314	20.2780	0.1317	2.4000	78.47
Mor_M09S05	M20	2.7105	4.3480	0.0117	20.3140	0.0728	2.4000	80.14
Mor_M09S06	M21	3.1511	5.2040	0.1362	20.5020	0.2259	2.4000	76.42
Mor_M10S01	M22	3.0266	5.0500	0.0759	20.4120	0.0873	2.4000	76.31
Mor_M10S02	M23	2.4111	4.0920	0.0075	20.0480	0.4868	2.4000	77.77
Mor_M10S03	M24	2.5226	4.1200	0.0210	20.4640	0.1461	2.4000	77.56
Mor_M10S04	M25	2.5641	4.1660	0.0150	20.4180	0.0833	2.4000	78.32
Mor_M10S05	M26	2.5830	4.3920	0.0194	20.3840	0.2215	2.4000	75.09
Mor_M10S06	M27	2.6273	4.2600	0.0237	20.2880	0.1842	2.4000	79.49
Mor_M10S07	M28	2.4709	4.0640	0.0520	20.3080	0.1512	2.4000	78.21
Mor_M10S08	M29	2.9457	4.7820	0.0223	20.4440	0.1699	2.4000	78.19
Mor_M11S01	M30	2.8920	5.0240	0.0850	20.3860	0.0761	2.4000	73.48
Mor_M11S02	M31	2.4391	3.9140	0.0136	20.4300	0.1035	2.4000	79.21
Mor_M11S03	M32	2.5541	4.0920	0.0040	20.4580	0.1308	2.4000	79.12
Mor_M11S04	M33	2.5147	4.0840	0.0102	20.3780	0.1426	2.4000	78.66
Mor_M11S05	M34	3.0465	4.9120	0.0098	20.3880	0.1930	2.4000	79.16
Mor_M11S06	M35	2.2912	3.7400	0.0253	20.3320	0.3325	2.4000	78.62
Mor_M11S07	M36	2.8132	4.6280	0.0194	20.6660	0.1368	2.4000	75.51
Mor_M11S08	M37	2.9532	4.8200	0.0415	20.5480	0.1627	2.4000	76.98

Table A.7: *Mechanical properties for mortar reference samples*

Sample name	**Sample Descr.**	F_{max} **[N]**	E **[GPa]**	σ **[MPa]**	E_{sr} **[GPa]**	σ_{sr} **[MPa]**	**Material be-haviour**	**Fracture pattern**
Mor_M04S01	M1	49.45	1.2174	7.237	-	-	Tough	-
Mor_M04S02	M2	79.62	0.9904	6.105	-	-	Brittle	-
Mor_M04S03	M3	277.66	0.5245	7.854	-	-	Brittle	-
Mor_M04S04	M4	87.86	1.0983	7.771	-	-	Tough	-
Mor_M07S01	M5	177.06	0.9997	9.803	-	-	Brittle	-
Mor_M07S02	M6	112.74	1.0326	8.263	-	-	Brittle	-
Mor_M07S03	M7	143.47	2.0162	11.597	-	-	Tough	-
Mor_M07S04	M8	148.86	1.8677	11.832	-	-	Tough	-
Mor_M07S05	M9	132.44	1.4598	10.372	-	-	Tough	-
Mor_M07S06	M10	159.82	1.1618	11.564	-	-	Brittle	-
Mor_M08S01	M11	82.53	0.4358	4.266	-	-	Tough	-
Mor_M08S02	M12	88.31	0.3159	4.499	-	-	Tough	-
Mor_M08S03	M13	114.51	1.5845	7.766	-	-	Tough	-
Mor_M08S04	M14	148.98	0.9819	9.387	-	-	Brittle	-
Mor_M08S05	M15	130.26	2.2468	8.692	-	-	Tough	-
Mor_M09S01	M16	167.34	0.8128	8.720	-	-	Brittle	-
Mor_M09S02	M17	152.20	0.8264	11.274	-	-	Brittle	-
Mor_M09S03	M18	168.59	0.7531	9.965	-	-	Brittle	-
Mor_M09S04	M19	149.81	1.9020	11.677	-	-	Brittle	-
Mor_M09S05	M20	131.46	3.9776	9.631	-	-	Brittle	-
Mor_M09S06	M21	190.59	0.8936	8.892	-	-	Tough	-
Mor_M10S01	M22	197.47	0.9284	9.914	-	-	Brittle	-
Mor_M10S02	M23	132.19	1.9627	11.164	-	-	Brittle	-
Mor_M10S03	M24	105.41	2.4844	8.761	-	-	Brittle	-
Mor_M10S04	M25	132.56	1.8828	10.690	-	-	Brittle	-
Mor_M10S05	M26	168.20	1.1636	11.865	-	-	Brittle	-
Mor_M10S06	M27	128.76	1.6565	9.847	-	-	Tough	-
Mor_M10S07	M28	141.92	2.6975	12.183	-	-	Brittle	-
Mor_M10S08	M29	166.83	1.0296	9.582	-	-	Brittle	-
Mor_M11S01	M30	165.31	1.0265	8.436	-	-	Brittle	-
Mor_M11S02	M31	140.62	2.6474	13.187	-	-	Brittle	-
Mor_M11S03	M32	157.77	2.3958	13.282	-	-	Brittle	-
Mor_M11S04	M33	131.16	1.5709	11.075	-	-	Brittle	-
Mor_M11S05	M34	206.33	0.8969	11.062	-	-	Brittle	-
Mor_M11S06	M35	108.46	1.6241	11.312	-	-	Tough	-
Mor_M11S07	M36	147.49	0.8678	9.140	-	-	Brittle	-
Mor_M11S08	M37	200.65	0.9888	11.263	-	-	Brittle	-

A.2.3. Soda-lime Glass Reference Data

The physical and mechanical properties of the soda-lime glass reference samples are shown in Table A.8 and Table A.9 respectively. In order to provide the most accurate results, the physical properties were measured using a micrometre. The discrepancies in relative density are attributed to measuring errors. Note, no stress range correction has been applied. Most samples shattered in to0 many pieces to assess the number of fractures.

Table A.8: *Physical properties for soda-lime glass reference samples*

Sample name	Sample Descr.	Mass [g]	Average height [mm]	Height STD (n=5)	Average diameter [mm]	Diameter STD (n=5)	Theoretical density [g cm^{-3}]	Relative density [%]
SLGlass_21	G21	1.4577	1.8860	0.0016	19.8180	0.2141	2.5300	99.04
SLGlass_22	G22	1.4666	1.8960	0.0015	19.9350	0.0082	2.5300	97.94
SLGlass_23	G23	1.4578	1.8910	0.0017	19.9180	0.0046	2.5300	97.79
SLGlass_24	G24	1.4725	1.8970	0.0005	19.9760	0.0065	2.5300	97.88
SLGlass_25	G25	1.4613	1.8920	0.0006	19.9480	0.0110	2.5300	97.68
SLGlass_31	G31	2.1927	2.8470	0.0006	19.9250	0.0242	2.5300	97.63
SLGlass_32	G32	2.2121	2.8460	0.0008	19.9970	0.0110	2.5300	97.83
SLGlass_33	G33	2.2050	2.8460	0.0004	19.9610	0.0065	2.5300	97.87
SLGlass_34	G34	2.1910	2.8420	0.0008	19.9300	0.0059	2.5300	97.67
SLGlass_35	G35	2.2118	2.8430	0.0004	20.0020	0.0217	2.5300	97.86
SLGlass_36	G36	2.1871	2.8440	0.0005	19.9070	0.0039	2.5300	97.64
SLGlass_41	G41	2.9758	3.8200	0.0010	20.0020	0.0090	2.5300	98.00
SLGlass_42	G42	2.9662	3.8190	0.0010	19.9670	0.0074	2.5300	98.05
SLGlass_43	G43	2.9526	3.8160	0.0008	19.9220	0.0049	2.5300	98.11
SLGlass_44	G44	2.9851	3.8190	0.0019	20.0600	0.0134	2.5300	97.75

Table A.9: *Mechanical properties for soda-lime glass reference samples*

Sample name	Sample Descr.	F_{max} [N]	E [GPa]	σ [MPa]	E_{sr} [GPa]	σ_{sr} [MPa]	Material behaviour	Fracture pattern
SLGlass_21	G21	269.52	41.3563	143.880	-	-	Brittle	-
SLGlass_22	G22	368.00	48.1471	193.600	-	-	Brittle	-
SLGlass_23	G23	400.83	53.7912	212.223	-	-	Brittle	-
SLGlass_24	G24	341.33	44.8103	179.291	-	-	Brittle	-
SLGlass_25	G25	279.45	41.1853	147.933	-	-	Brittle	-
SLGlass_31	G31	1001.14	35.9636	204.064	-	-	Brittle	-
SLGlass_32	G32	708.27	23.7516	144.411	-	-	Brittle	-
SLGlass_33	G33	1090.77	26.5276	221.605	-	-	Brittle	-
SLGlass_34	G34	1365.17	27.3920	277.443	-	-	Brittle	-
SLGlass_35	G35	682.63	24.4217	139.606	-	-	Brittle	-
SLGlass_36	G36	1007.96	25.7632	205.229	-	-	Brittle	-
SLGlass_41	G41	2977.33	19.4370	298.268	-	-	Brittle	-
SLGlass_42	G42	1848.75	15.4308	186.229	-	-	Brittle	-
SLGlass_43	G43	1860.41	15.9132	187.813	-	-	Brittle	-
SLGlass_44	G44	2962.03	18.9734	296.616	-	-	Brittle	-
SLGlass_45	G45	1477.10	14.5301	149.126	-	-	Brittle	-

B

Supplementary Information for the Compression Testing Method

In this appendix the supplementary information for the compression testing method is presented. This information from the bench compliance tests used to process the data is shown in Section B.1. Next, Section B.2 lists some of the validation experiments that were performed to assess the validity of the obtained strength results. In Section B.3 the effect of the stress range correction on the mechanical properties is discussed. Finally, a sensitivity analysis is performed on the variables used to calculated the biaxial strength in Section B.4.

B.1. Bench Compliance and Data Processing Information

In this section the information used during the data processing of the compression test data is shown. The diameters were measured using a Keyence VR5000 WideArea 3D Measurement System, images of which are shown in Figure B.1. Table B.1 summarises the data used for the data processing. Note, BC5 was not used so no slope is given.

Table B.1: *Data for the bench compliance tests used in data processing*

Bench compliance		**BC1**	**BC2**	**BC3**	**BC4**	**BC5**	**BC6**
Maximum load	[kN]	10	10	1	1	1	1
Indentation diameter	[mm]	2.7676	3.0704	0.9846	0.8644	0.8489	0.9838
Slope	[1×10^{-4} N mm^{-1}]	1.01077	1.15487	2.01072	2.11141	-	2.01865

Bench compliance		**BC7**	**BC8**	**BC9**	**BC10**	**BC11**	**BC12**
Maximum load	[kN]	1	1	1	1	1	10
Indentation diameter	[mm]	0.9792	0.9853	0.9241	0.9546	0.9546	3.1301
Slope	[1×10^{-4} N mm^{-1}]	2.16428	2.03090	1.77473	2.14913	1.84288	1.14864

B.2. Validation Experiments

In this section the validation experiments are discussed. Three different experiments were performed. First, zirconia disk reference samples were tested. Next, reference samples made from mortar were tested in order to provide a terrestrial material to which the properties of sintered samples could be measured against. Finally, soda-lime glass samples were tested.

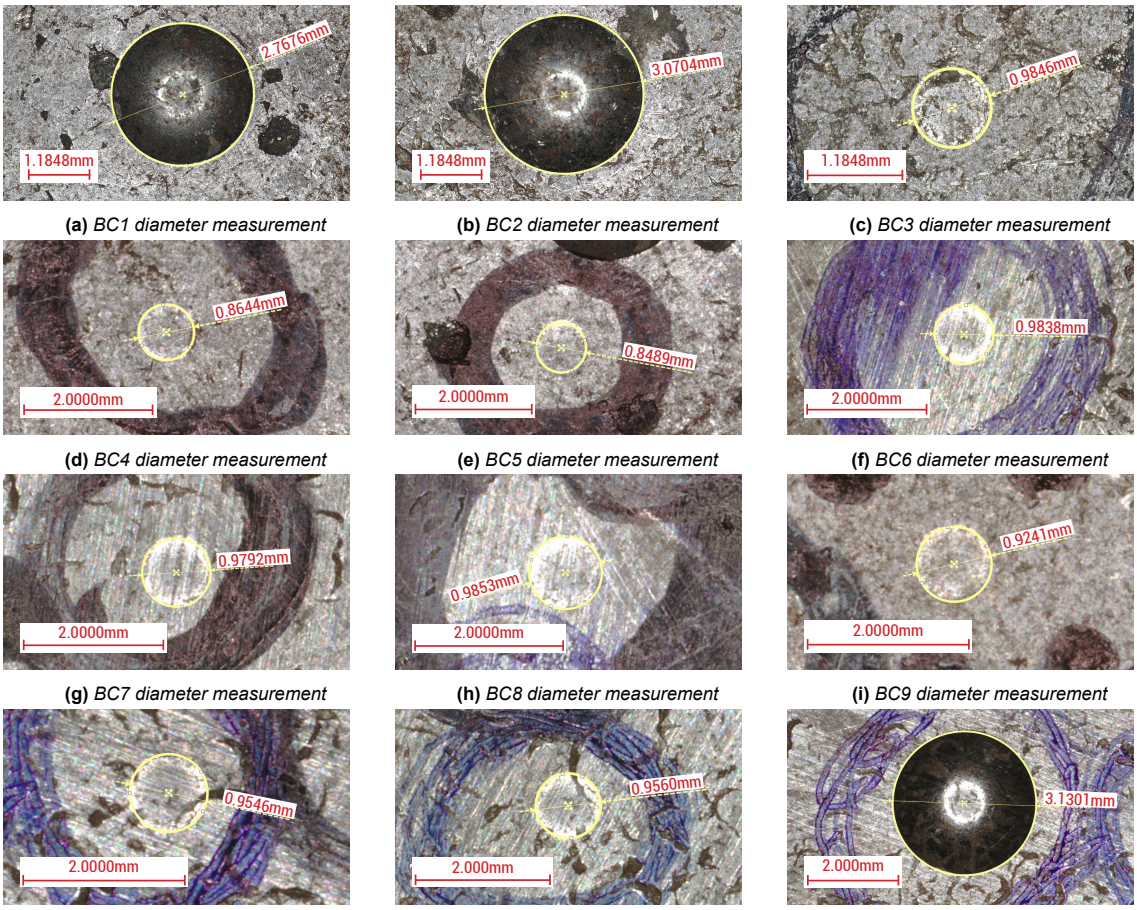

(a) *BC1 diameter measurement* **(b)** *BC2 diameter measurement* **(c)** *BC3 diameter measurement*

(d) *BC4 diameter measurement* **(e)** *BC5 diameter measurement* **(f)** *BC6 diameter measurement*

(g) *BC7 diameter measurement* **(h)** *BC8 diameter measurement* **(i)** *BC9 diameter measurement*

(j) *BC10 diameter measurement* **(k)** *BC11 diameter measurement* **(l)** *BC12 diameter measurement*

Figure B.1: *Bench compliance indentation images used for data correction*

B.2.1. Zirconia Disk Compression Results

Zirconia disk samples were obtained from UniPreTec[1] and used to get an initial feel for the validity of the test results obtained from our compression test set-up. The results obtained for the biaxial strength of the two tested samples are shown in Figure B.2. In Figure B.2, reference data from Spintzyk et al. for the minimal and maximal biaxial strength, 456 MPa and 1212 MPa respectively, are shown [86]. Data from Lupercio et al. falls within this range [61]. All of the reference data was obtained using a testing method comparable to the BoR method. Comparing our results with those from literature, our values fall well within the observed range. Therefore, it is assumed that our test set-up results in trustworthy values for the biaxial strength.

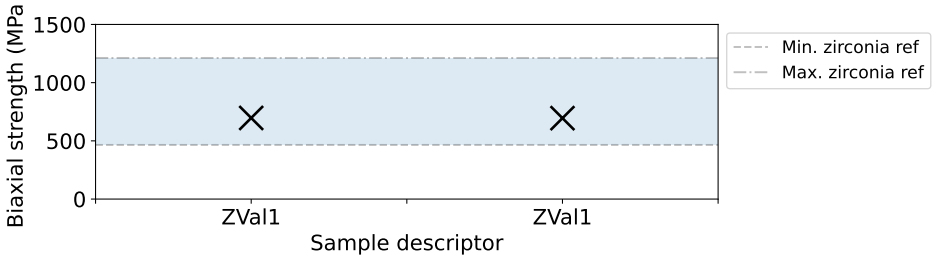

Figure B.2: *Strength of the zirconia reference samples*

[1] See UniPreTec YSZ Ceramic Plates product page, last accessed 20-04-2022 (link)

B.2.2. Mortar Disk Compression Results

Mortar samples were created in an effort determine baseline mechanical properties for a terrestrial material used in structural applications. The mortar was made using a proprietary mixture of sand, cement, a hardening agent and several cement-to-water ratios. Curing times varied between 7 and 21 days. Samples were poured into cylindrical moulds and after curing cut using a Sectom 10 cutting machine. After cutting, all samples were dried before mechanical testing. The results of the tested samples are shown in Figure B.3. Note, the stress range correction has not been applied.

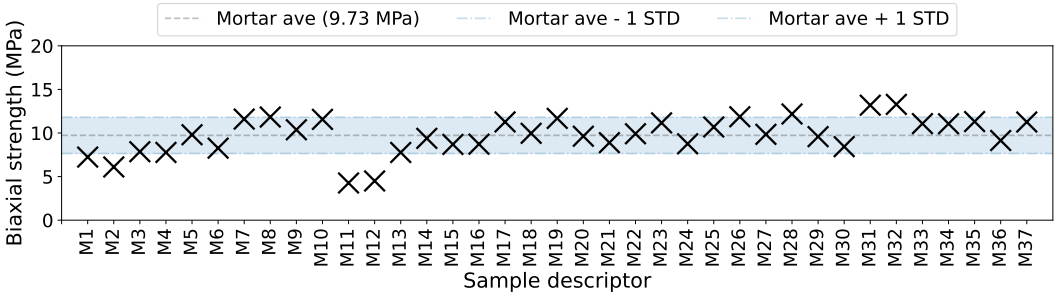

Figure B.3: *Strength of the mortar reference samples*

B.2.3. Soda-lime Glass Compression Results

A downside of the mortar reference samples were the less well-defined properties and the lack of proper literature reference values for comparison. In order to find a well-defined specimen usable for literature comparison, soda-lime glass was chosen.

The soda-lime glass used in these experiments was obtained from Yuanbo Engineering Co./LingYan Engineering Co.[2]. Three different thicknesses were tested in order to evaluate the effect of sample thickness on the obtained results. Additionally, during compression testing, two different compression bench set-ups were used. One set-up had more distance and connectors between the indenter and the loadcell, denoted as ”long”, and the other was shorter, denoted as ”short”. The effect of the difference in these testing set-ups was also investigated.

The results of the compression tests of the soda-lime glass samples are shown below. Figures B.4 and B.5 show the obtained stiffness and strength values respectively.

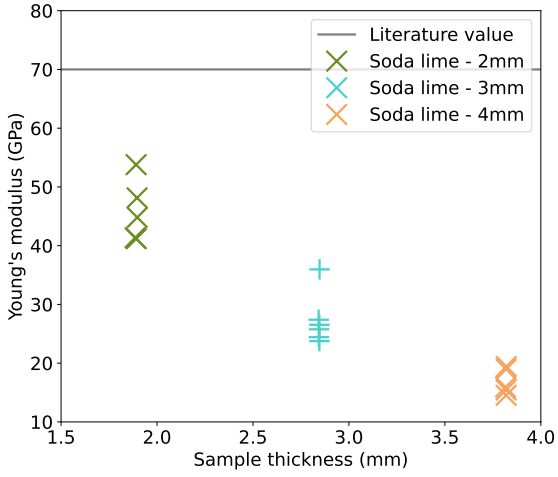

Figure B.4: *Stiffness of the soda-lime glass reference samples vs sample thickness*

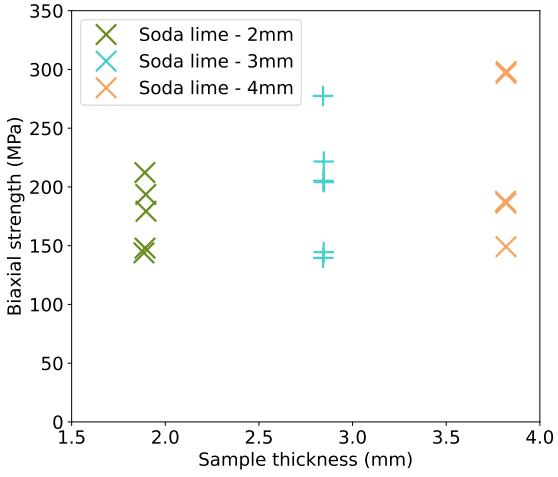

Figure B.5: *Strength of the soda-lime glass reference samples vs sample thickness*

The results in Figure B.4 show that the calculated value for the stiffness decreases with increasing

[2]See LingYan Engineering Co. glass product page, last accessed 20-04-2022 (link)

sample thickness. Therefore, the thicker the sample, the less accurate the estimate for the stiffness. A value of 70 GPa obtained from literature [87] is also included in the figure for reference.

Figure B.5 shows that the calculated biaxial strengths for all tested sample thicknesses is comparable. Note, one sample (G31) was tested using a 1 kN load cell and did not fail. However, the calculated biaxial strength value serves as a minimal biaxial strength for that sample. In order to validate our results, literature data was used. Meyland et al. investigated the effect of different loading rates on the biaxial strength of soda-lime glass samples [88]. The loading rates used in that study encompass those in this research. The results of our soda-lime tests for our loading rate (piston velocity) together with their results are shown in Figure B.6.

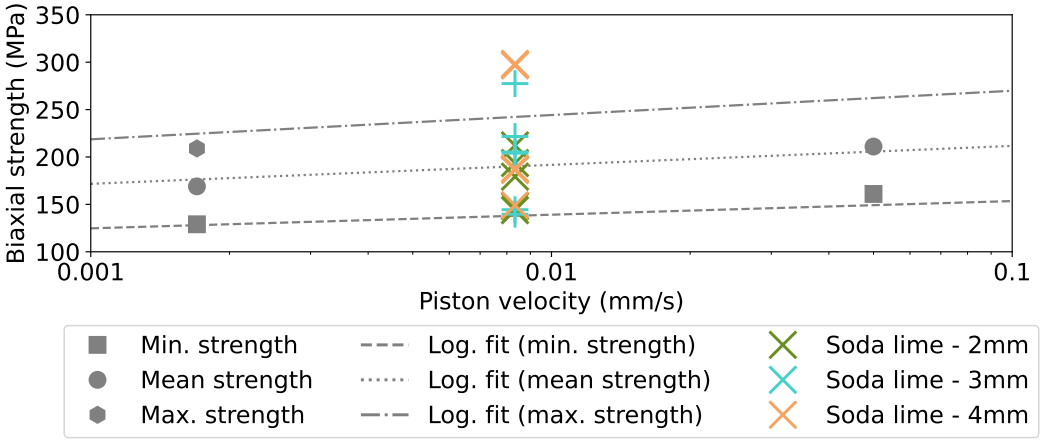

Figure B.6: *Biaxial strength of soda-lime glass specimen vs piston velocity as compared to literature [88]*

The results in Figure B.6 show that the results obtained at our loading rate, except a few outliers, correspond well with those obtained by Meyland et al. This again reinforces the validity of our results.

From the 2 mm thickness samples, three were tested using the long set-up, and two using the short. Images of the long and short test set-up can be seen in Figure B.7a and Figure B.7b respectively. Figure B.7c shows the result for the obtained biaxial strength.

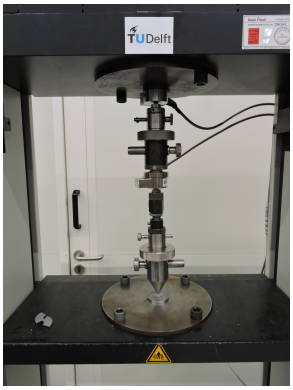

(a) *Image of the "long" test set-up*

(b) *Image of the "short" test set-up*

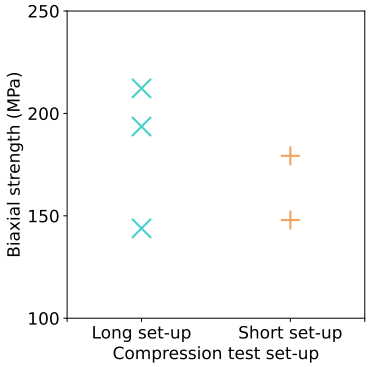

(c) *Compression test results for 2mm soda lime disk samples*

Figure B.7: *Effect of the compression test set-up, with a) the long set-up, b) the short and c) the results of tested samples.*

Figure B.7c shows that the biaxial strength values obtained using the different compression test set-ups is comparable. Therefore, it is concluded that the difference in compression test set-up did not result in notable differences in the obtained values for the biaxial strength.

B.3. Effect of the Stress Range Correction

The stress range correction was applied to evaluate the mechanical properties of samples within the same stress range, see Subsection 3.7.3. To assess the effect of this correction, the obtained values for the Young's modulus (stiffness) and biaxial strength before and after the correction are plotted. These results, together with the percentage difference, are shown in Figure B.8.

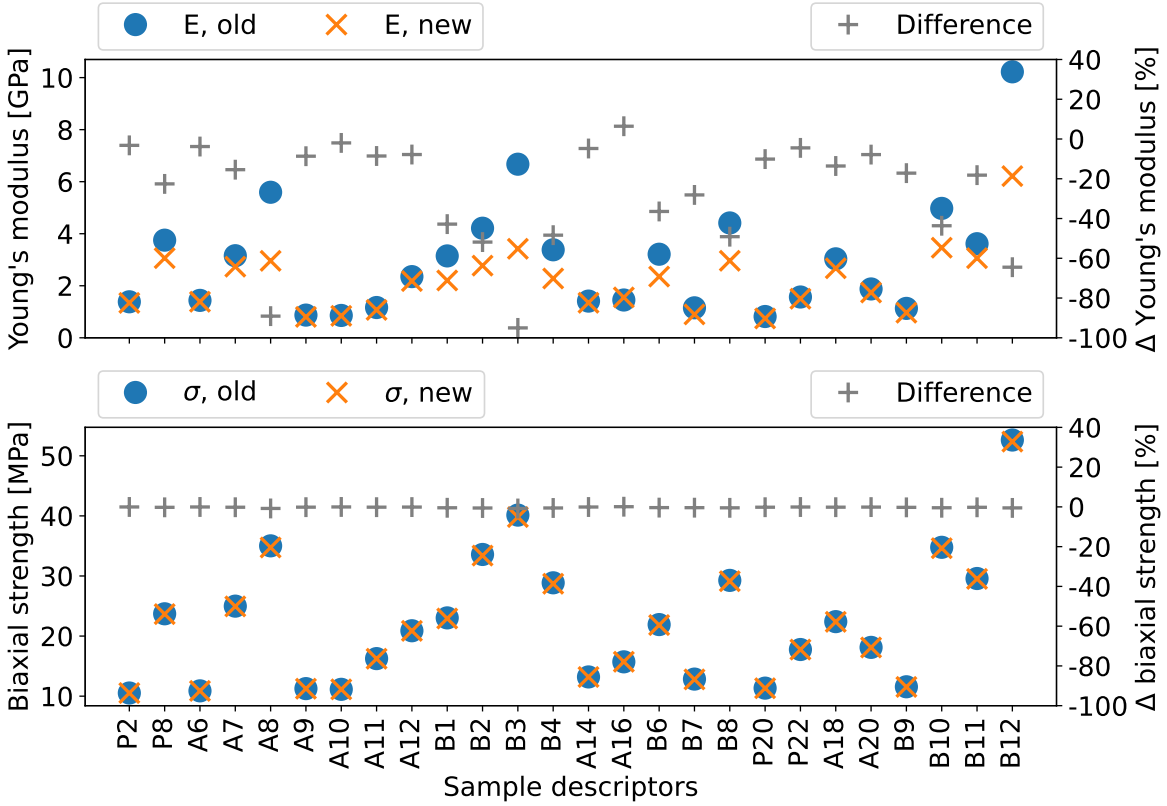

Figure B.8: *Differences caused by the stress range correction implementation on the Young's modulus and the biaxial strength*

Looking at the differences in Figure B.8, the values for the stiffness change significantly (in some cases almost up to 100 %), whereas the difference in biaxial strength hardly changes at all. This difference in stiffness is due to the correction itself. Since all samples are evaluated at the same stress range, this can result in different force-deflection areas being used to calculate the stiffness. The effect of this stiffness value on the value of the biaxial strength, however, is low (see the next section). It is concluded that the effect of the stress range correction on the biaxial strength values is negligible.

B.4. Sensitivity Analysis

The sensitivity analysis was performed for Sample *POC_S_5_1610501*, with descriptor *A12* in Tables A.1 to A.3. This sample was chosen as a representative sample for enriched material with an as-expected deflection behaviour. Two types of computations are performed. The first is the sensitivity of the investigated variable in the final formula (Equation 3.8), the second is the full computation in which any implicit use of the variable is also taken into account. Figure B.9 presents the graphs for all investigated parameters.

From the graphs it can be seen that the sample thickness (Figure B.9c) has the biggest effect on the calculated value of the biaxial strength, especially in the full computation calculation where it is used to determine the equivalent contact radius. Additionally, it can be seen that the effect of the sample stiffness (Figure B.9i) has very little effect on the value of the biaxial strength. This confirms the findings of the previous section on the effect of the stress range correction where the biaxial strength was hardly affected.

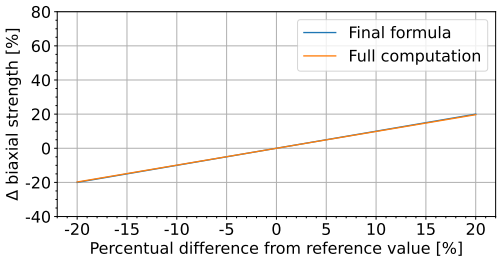

(a) *Sensitivity of the biaxial strength to the maximum sustained load*

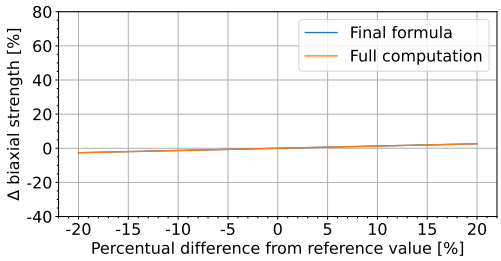

(b) *Sensitivity of the biaxial strength to the sample Poisson's ratio*

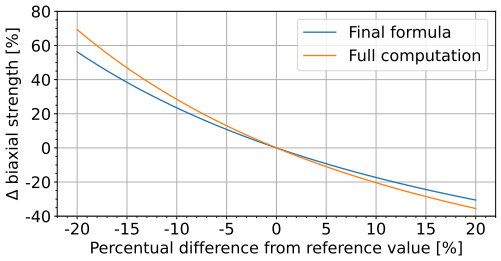

(c) *Sensitivity of the biaxial strength to the sample thickness*

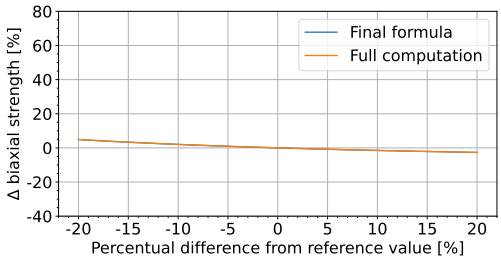

(d) *Sensitivity of the biaxial strength to the sample radius*

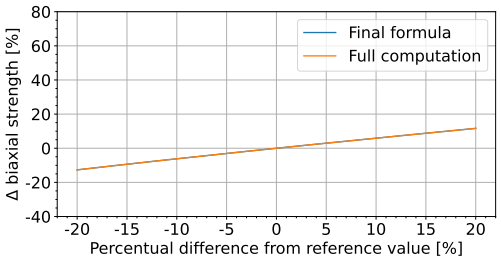

(e) *Sensitivity of the biaxial strength to the support hole radius*

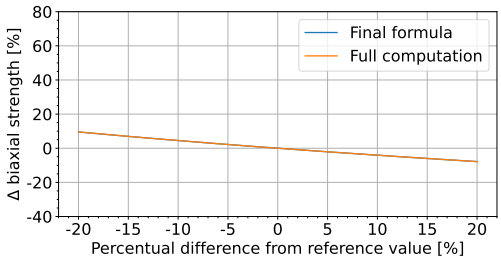

(f) *Sensitivity of the biaxial strength to the equivalent contact radius*

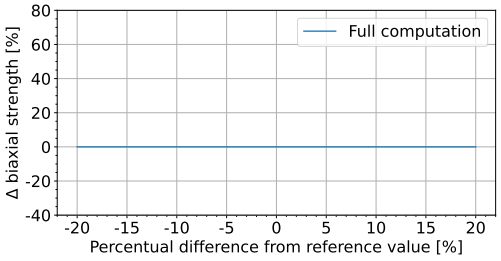

(g) *Sensitivity of the biaxial strength to the loading ball Poisson ratio*

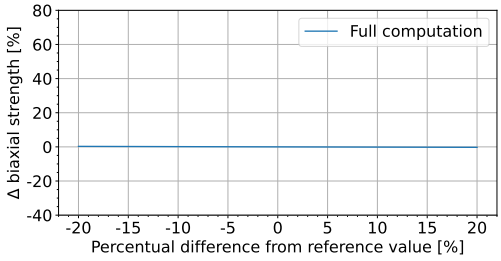

(h) *Sensitivity of the biaxial strength to the loading ball radius*

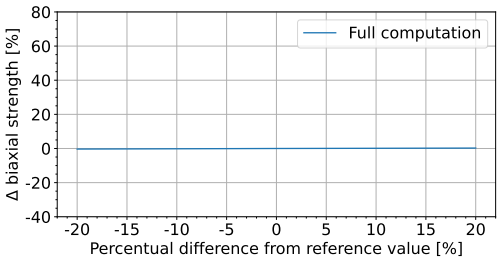

(i) *Sensitivity of the biaxial strength to the sample Young's modulus*

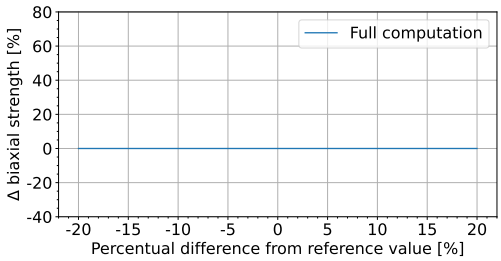

(j) *Sensitivity of the biaxial strength to the loading ball Young's Modulus*

Figure B.9: *Sensitivity of the biaxial strength to the formula variables*